The Astrophysical Journal Letters, 994:L17 (34pp), 2025 November 20 https://doi.org/10.3847/2041-8213/ae1741

Comprehensive X-Ray Observations of the Exceptional Ultralong X-Ray and Gamma-Ray Transient GRB 250702B with Swift, NuSTAR, and Chandra: Insights from the X-Ray Afterglow Properties

Brendan O'Connor[1,22], Ramandeep Gill[2,3], James DeLaunay[4,5], Jeremy Hare[6,7,8], Dheeraj Pasham[9,10], Eric R. Coughlin[11], Ananya Bandopadhyay[11], Akash Anumarlapudi[12], Paz Beniamini[3,10,13], Jonathan Granot[3,10,13], Igor Andreoni[12], Jonathan Carney[12], Michael J. Moss[14], Ersin Göğüş[15], Jamie A. Kennea[4], Malte Busmann[16], Simone Dichiara[4], James Freeburn[12], Daniel Gruen[16,17], Xander J. Hall[1], Antonella Palmese[1], Tyler Parsotan[6], Samuele Ronchini[4,18], Aaron Tohuvavohu[19], and Maia A. Williams[20,21]

[1] McWilliams Center for Cosmology and Astrophysics, Department of Physics, Carnegie Mellon University, Pittsburgh, PA 15213, USA; boconno2@andrew.cmu.edu
[2] Instituto de Radioastronomía y Astrofísica, Universidad Nacional Autónoma de México, Antigua Carretera a Pátzcuaro # 8701, Ex-Hda. San José de la Huerta, Morelia, Michoacán, C.P. 58089, México
[3] Astrophysics Research Center of the Open university (ARCO), The Open University of Israel, P.O Box 808, Ra'anana 4353701, Israel
[4] Department of Astronomy and Astrophysics, The Pennsylvania State University, 525 Davey Lab, University Park, PA 16802, USA
[5] Institute for Gravitation and the Cosmos, The Pennsylvania State University, University Park, PA 16802, USA
[6] Astrophysics Science Division, NASA Goddard Space Flight Center, 8800 Greenbelt Rd, Greenbelt, MD 20771, USA
[7] Center for Research and Exploration in Space Science and Technology, NASA/GSFC, Greenbelt, MD 20771, USA
[8] The Catholic University of America, 620 Michigan Ave., N.E. Washington, DC 20064, USA
[9] Eureka Scientific, 2452 Delmer Street Suite 100, Oakland, CA 94602-3017, USA
[10] Department of Physics, The George Washington University, Washington, DC 20052, USA
[11] Department of Physics, Syracuse University, Syracuse, NY 13210, USA
[12] University of North Carolina at Chapel Hill, 120 E. Cameron Ave., Chapel Hill, NC 27514, USA
[13] Department of Natural Sciences, The Open University of Israel, P.O Box 808, Ra'anana 4353701, Israel
[14] NASA Postdoctoral Program Fellow, NASA Goddard Space Flight Center, Greenbelt, MD 20771, USA
[15] Sabancı University, Faculty of Engineering and Natural Sciences, İstanbul 34956, Türkiye
[16] University Observatory, Faculty of Physics, Ludwig-Maximilians-Universität München, Scheinerstr. 1, 81679 Munich, Germany
[17] Excellence Cluster ORIGINS, Boltzmannstr. 2, 85748 Garching, Germany
[18] Gran Sasso Science Institute (GSSI), 67100, L'Aquila, Italy
[19] Cahill Center for Astronomy and Astrophysics, California Institute of Technology, Pasadena, CA 91125, USA
[20] Department of Physics and Astronomy, Northwestern University, Evanston, IL 60208, USA
[21] Center for Interdisciplinary Exploration and Research in Astronomy (CIERA), Northwestern University, 1800 Sherman Avenue, Evanston, IL 60201, USA

Received 2025 September 17; revised 2025 October 8; accepted 2025 October 22; published 2025 November 14

Abstract

GRB 250702B is an exceptional transient that produced multiple episodes of luminous gamma-ray radiation lasting for >25 ks, placing it among the class of ultralong gamma-ray bursts (GRBs). However, unlike any known GRB, the Einstein Probe detected soft-X-ray emission up to 24 hr before the gamma-ray triggers. We present comprehensive X-ray observations of the transient's "afterglow" obtained with the Neil Gehrels Swift Observatory, the Nuclear Spectroscopic Telescope Array, and the Chandra X-ray Observatory between 0.5 and 65 days (observer frame) after the initial high-energy trigger. The X-ray emission decays steeply as $\sim t^{-1.9}$ and shows short-timescale X-ray variability ($\Delta T/T < 0.03$) in both Swift and NuSTAR, consistent with flares superposed on an external shock continuum. Serendipitous detections by the Swift Burst Alert Telescope out to ∼0.3 days and continued NuSTAR variability to ∼2 days imply sustained central engine activity; including the early Einstein Probe X-ray detections, the required engine duration is $\gtrsim 3$ days. Afterglow modeling favors the combination of forward- and reverse-shock emission in a windlike ($k \approx 2$) environment. These properties, especially the long-lived engine and early soft-X-ray emission, are difficult to reconcile with a collapsar origin, and GRB 250702B does not fit neatly with canonical ultralong GRBs or relativistic tidal disruption events (TDEs). A "hybrid" scenario, in which a star is disrupted by a stellar-mass black hole (a micro-TDE), provides a plausible explanation, although a relativistic TDE from an intermediate-mass black hole remains viable.

Unified Astronomy Thesaurus concepts: X-ray astronomy (1810); X-ray transient sources (1852); Gamma-ray bursts (629); Relativistic jets (1390); Black holes (162); High energy astrophysics (739); Time domain astronomy (2109); Gamma-ray transient sources (1853)

1. Introduction

Gamma-ray bursts (GRBs) are among the most energetic explosions in the Universe, releasing 10^{48-52} erg of energy (collimation-corrected) in the X-ray and gamma-ray regime (1–10,000 keV). They are commonly classified as short or long GRBs, based on their prompt emission duration (C. Kouveliotou et al. 1993) and hardness ratio (HR; E. Nakar 2007;

---

[22] McWilliams Fellow.

O. Bromberg et al. 2013). The prompt duration is typically linked to the lifetime of the central engine after the jet breaks out from the surrounding stellar material (e.g., O. Bromberg et al. 2012, 2013). A subset of GRBs, referred to as ultralong GRBs, display exceptionally extended prompt gamma-ray emission, lasting for thousands to tens of thousands of seconds (e.g., Y. Y. Tikhomirova & B. E. Stern 2005; B. Gendre et al. 2013; A. J. Levan et al. 2014; K. Ioka et al. 2016).

An alternative origin for some ultralong events is that they arise from relativistic jetted tidal disruption events (TDEs), in which a star is shredded by a massive black hole (BH), launching a jet along our line of sight (J. S. Bloom et al. 2011; A. J. Levan et al. 2011; S. B. Cenko et al. 2012; D. R. Pasham et al. 2015, 2023; I. Andreoni et al. 2022). This was the case for GRB 110328A/Sw J1644+57 (J. S. Bloom et al. 2011; D. N. Burrows et al. 2011), which was the first event discovered in this class. Unlike classical GRBs, the recognized sample of relativistic TDEs lacks highly variable prompt gamma-ray emission, and these events were instead discovered via longer-duration "image" triggers (D. N. Burrows et al. 2011; J. R. Cummings et al. 2011; T. Sakamoto et al. 2011) or searches using multiday stacked data sets (S. B. Cenko et al. 2012; G. C. Brown et al. 2015).

Differentiating ultralong GRBs from relativistic TDEs remains a major observational challenge. The clearest discriminant is the identification of either (i) a supernova, which solidifies a GRB progenitor, such as in GRB 111209A/SN 2011kl (J. Greiner et al. 2015), or (ii) a rapid X-ray shutoff, which is likely indicative of a transition in the accretion mode and is taken as robust evidence for a TDE origin (e.g., D. R. Pasham et al. 2015; T. Eftekhari et al. 2024). Another key distinction lies in the transient's location within its host galaxy. Long GRBs often occur in star-forming regions offset from their host galaxy's center, whereas TDEs are expected to originate at the precise nuclei of their host galaxies, coincident with supermassive black holes (SMBHs). In addition, relativistic TDEs typically exhibit prolonged (weeks to months) and luminous X-ray emission, exceeding that of standard or ultralong GRBs (I. Andreoni et al. 2022; D. R. Pasham et al. 2023). This is usually considered the signpost of their discovery and has been used as an argument for the identification of other relativistic TDE candidates (e.g., EP240408a; B. O'Connor et al. 2025b; W. Zhang et al. 2025).

On 2025 July 2, a series of multiple high-energy bursts were detected by numerous satellites, including the Fermi Gamma-ray Space Telescope (C. Meegan et al. 2009), Konus-Wind (R. L. Aptekar et al. 1995), the Space Variable Objects Monitor (J. Wei et al. 2016), the Neil Gehrels Swift Observatory (N. Gehrels et al. 2004), the Monitor of All-sky X-ray Image (M. Matsuoka et al. 2009), and the Einstein Probe (EP; W. Yuan et al. 2025). These multiple gamma-ray triggers (GRB 250702B/D/E; E. Neights et al. 2025a) were later noticed to originate from the same sky location (H. Q. Cheng et al. 2025a; J. DeLaunay et al. 2025; D. Frederiks et al. 2025; Y. Kawakubo et al. 2025; E. Neights et al. 2025a; Svom/Grm Team et al. 2025), and the event was subsequently designated GRB 250702BDE/EP250702a. We adopt the name GRB 250702B, for consistency with standard GRB nomenclature.

Due to its on-sky location's close proximity to the Galactic plane ($b \sim 5^\circ$), its nature was initially ambiguous, with possible interpretations ranging from a new X-ray binary in outburst or a peculiar extragalactic transient. While debate over its classification continues (P. Beniamini et al. 2025; J. Carney et al. 2025; B. P. Gompertz et al. 2025; J. Granot et al. 2025, in preparation; A. J. Levan et al. 2025b; E. Neights et al. 2025b; G. Oganesyan et al. 2025), the most plausible scenarios are that it represents either an ultralong GRB or a relativistic TDE. The duration of the source's flaring activity, lasting for at least >25 ks (observer frame) at gamma-ray wavelengths (D. Frederiks et al. 2025; E. Neights et al. 2025a), easily places it among the class of ultralong GRBs. However, the EP mission identified source activity at soft X-rays (0.5–4 keV) starting nearly a full 24 hr before the first gamma-ray trigger (H. Q. Cheng et al. 2025b; D. Y. Li et al. 2025), which is not easily reconciled with standard GRB models.

Following the arcminute localization by the EP (H. Q. Cheng et al. 2025b; D. Y. Li et al. 2025), X-ray observations with the Swift X-ray Telescope (XRT; D. N. Burrows et al. 2005) identified a rapidly fading X-ray source and provided an arcsecond localization (J. A. Kennea et al. 2025). Near-infrared observations with the Very Large Telescope revealed an extremely red, quickly decaying counterpart (A. J. Levan et al. 2025b). Subsequent Hubble Space Telescope observations provided conclusive evidence that the transient lies on top of the light of an irregular host galaxy with a negligible probability (<0.1%) of chance alignment (A. J. Levan et al. 2025b), confirming the extragalactic nature of GRB 250702B. A spectroscopic redshift of the host galaxy of $z = 1.036$ was obtained by the James Webb Space Telescope (B. P. Gompertz et al. 2025). Notably, the source is spatially offset from the center of the galaxy (J. Carney et al. 2025; A. J. Levan et al. 2025b), complicating a classical TDE interpretation.

We present comprehensive X-ray observations of GRB 250702B with Swift, the Nuclear Spectroscopic Telescope Array (NuSTAR), and Chandra, aimed at characterizing its temporal and spectral evolution. At first glance, the observed multiwavelength behavior is consistent with two leading interpretations: (i) a relativistic jetted TDE, potentially originating from an offset intermediate-mass black hole (IMBH), or (ii) a peculiar ultralong GRB featuring a soft-X-ray "precursor." We explore these possibilities in detail, highlighting the conflicting lines of evidence making this event an outlier that resists a straightforward classification within existing high-energy transient populations.

Throughout the manuscript, we adopt a standard ΛCDM cosmology (Planck Collaboration et al. 2020), with $H_0 = 67.4\ \mathrm{km\ s^{-1}\ Mpc^{-1}}$, $\Omega_\mathrm{m} = 0.315$, and $\Omega_\Lambda = 0.685$.

2. Observations

2.1. Neil Gehrels Swift Observatory

2.1.1. Burst Alert Telescope

The Neil Gehrels Swift Observatory (N. Gehrels et al. 2004) Burst Alert Telescope (BAT; S. D. Barthelmy et al. 2005) is a large-field-of-view (∼2 sr) coded mask imager, capable of imaging in the 14–195 keV energy range. Additionally, BAT is sensitive to impulsive emission originating from outside its coded field of view in the 50–350 keV energy range, though at a reduced sensitivity compared to inside the coded field of view.

On 2025 July 2, the Fermi Gamma-ray Burst Monitor (GBM; C. Meegan et al. 2009) sent out low-latency alerts for four bursts associated with GRB 250702B (E. Neights et al. 2025b, 2025a), triggering the Gamma-ray Urgent Archiver for Novel Opportunities (`GUANO`; A. Tohuvavohu et al. 2020) system for Swift to save BAT time-tagged event (TTE) data around the trigger times of each alert that would otherwise not be saved. The Non-Imaging Transient Reconstruction and Temporal Search (`NITRATES`; J. DeLaunay & A. Tohuvavohu 2022) pipeline was used to analyze the `GUANO` TTE data and significantly detected transient emission around the "D," "C," and "E" bursts, while the "B" burst was occulted by the Earth for Swift (see Table 4; E. Neights et al. 2025b). Since these three detections were outside of the coded field of view, they had large localization areas, but all included the common position of GRB 250702B. The combined localizations of the four GBM triggers and three `NITRATES` detections resulted in a 90% credible region of 142 deg^2 (J. DeLaunay et al. 2025).

We note that while GRB 250702C was dissociated from GRB 250702B and classified as a short GRB originating from another part of the sky (E. Neights et al. 2025b), a flare from GRB 250702B was coincidentally observed at the same time. The localization of the simultaneous short GRB was completely behind the Earth for Swift, thus the detection of the simultaneous flare from GRB 250702B by `NITRATES` was unaffected. This robustly confirms the source flaring activity at the time of GRB 250702C (MJD 60858.6177). See Table 3 for the peak fluxes of the bursts observed by BAT. Due to the long durations of these bursts, the background estimation may be contaminated by the source flux, causing the fluxes to be underestimated.

BAT TTE data are only available around onboard triggers or when `GUANO` is triggered by an external alert. When there are no TTE data, sky images can still be created from the BAT survey product, detector plane histograms (DPHs), which are detector plane images binned into 80 channels and ∼300 s exposures. Using the `BatAnalysis` package (T. Parsotan et al. 2023) to create and analyze sky images from the DPHs, we searched for emission from the position of GRB 250702B at times when it was inside the coded field of view of BAT.

After the initial GBM trigger, there were five observations on 2025 July 2 where GRB 250702B was inside of the BAT field of view, but none of them coincided with a reported burst. In two of these five observations, emission was significantly detected in images over the full observations. The first detection was in an 856 s exposure from 2025 July 2 16:30:11 to 2025 July 2 16:44:27, which is minutes after the GRB 250702E trigger. The second detection was in an 1058 s exposure from 2025 July 2 19:36:20 to 2025-07-02T19:53:58, which is hours after the last GBM trigger (GRB 250702E). The other three observations resulted in upper limits, with the deepest upper limit from an observation between the two detections, from 2025 July 2 17:52:13 to 2025 July 2 18:06:50. We also did not identify any significant emission from the position of GRB 250702B in any other observation within ±4 days from the GRB 250702D trigger time. The 5σ upper limits as well as the flux levels of the two detections derived from the BAT Survey mode data (14–195 keV) are tabulated in Table 2. We additionally confirmed there were no previous detections of GRB 250702B by BAT in the ∼month before the initial series of high-energy triggers. We tested multiple bin sizes between 1 and 7 days, but did not identify any significant signals.

2.1.2. XRT

Following the arcminute X-ray localization with the Wide-field X-ray Telescope (WXT) on EP (H. Q. Cheng et al. 2025b), we rapidly requested a Target of Opportunity (ToO) monitoring campaign (ObsID: 19906, Submitter: O'Connor; Obsid: 19928, GO program 1922200, PI: Pasham) with the Neil Gehrels Swift Observatory (N. Gehrels et al. 2004) XRT (D. N. Burrows et al. 2005). A highest-urgency ToO detected the X-ray source, with the XRT starting at 0.5 days after the initial Fermi trigger (J. A. Kennea et al. 2025). The source was localized (J. A. Kennea et al. 2025) to R.A., decl. (J2000) = $18^{\mathrm{h}}58^{\mathrm{m}}45\overset{\mathrm{s}}{.}61, -07^\circ52'26\overset{''}{.}9$, with an uncertainty of $2\overset{''}{.}0$ at the 90% confidence level (CL). The initial observations consisted of multiple ∼3 ks exposures over the first ∼3 days. Continued monitoring (PI: Pasham) extended to 45 days (2025 August 16), with ∼1 ks per day, for a total 45 ks exposure[23] (Table 1). All XRT data were obtained in in Photon Counting mode.

We retrieved the automated XRT lightcurve analysis[24] from the Living Swift XRT Point Source Catalogue (LSXPS; P. A. Evans et al. 2023). We applied a constant energy conversion factor (ECF) of $8.68 \times 10^{-11}\,\mathrm{erg\,cm^{-2}\,cts^{-1}}$ to convert between the count rate and unabsorbed flux using the best-fit spectral parameters from the initial XRT observation (see Section 3.2 for details). We further retrieved time-sliced spectral files through the XRT Build Products tool.[25] We likewise used this tool to obtain the 0.3–2 and 2–10 keV count-rate lightcurves and derive HRs.

2.2. NuSTAR

NuSTAR (F. A. Harrison et al. 2013) observes between 3 and 79 keV, using two coaligned focal plane modules (FPMs), referred to as FPMA and FPMB. Following the initial XRT detections, we triggered our approved NuSTAR ToO program (GO program 11282, PI: Pasham) for two epochs of ∼20 ks (Table 1), starting at 1.3 and 5.4 days after the Fermi trigger. A third NuSTAR observation with a ∼40 ks exposure occurred at 9.5 days through a Director's Discretionary Time (DDT) request (PI: Kammoun; see G. Oganesyan et al. 2025).

We used standard tasks within the NuSTAR Data Analysis Software pipeline (`NuSTARDAS`; `CALDB 20250714`) within `HEASoft` (Nasa High Energy Astrophysics Science Archive Research Center (Heasarc) 2014) to reprocess the data and then extract lightcurves and spectra. In the first epoch, the X-ray counterpart is clearly detected with a mean count rate of $\sim 0.3\,\mathrm{cts\,s^{-1}}$ per FPM (B. O'Connor et al. 2025a). We extracted the source counts from a circular region with radius 45″ from both FPMA and FPMB and utilized a source-free region with radius 120″ to extract the background. The background region was placed on the same detector as the transient. After subtracting the background, the mean count rate is $\sim 0.25\,\mathrm{cts\,s^{-1}}$ per FPM.

Due to the rapid decay of the X-ray lightcurve, the source is only very weakly detected in the second epoch, with a mean count rate of $\sim 0.03\,\mathrm{cts\,s^{-1}}$. The second observation is also contaminated by strong radiation belt activity (up to $\sim 15\,\mathrm{cts\,s^{-1}}$), and we therefore reprocessed the data with strict South Atlantic Anomaly (SAA) filtering

---

[23] https://www.swift.psu.edu/operations/obsSchedule.php?source_name=&ra=284.6898&dec=-7.8746

[24] https://www.swift.ac.uk/LSXPS/transients/9377

[25] https://www.swift.ac.uk/user_objects/index.php

(`saacalc=3, saamode=STRICT, tentacle=yes`). We are left with effective exposures of 18.2 ks for FPMA and 17.8 ks for FPMB. We extracted source counts using a circular region of radius 20″ and background counts from a region of radius 120″.

In addition to our two epochs of NuSTAR observations, we analyzed a third epoch of public DDT data, which was previously presented in G. Oganesyan et al. (2025). We applied strict SAA filtering cuts (as noted above), leaving us with exposures of 31.7 ks for FPMA and 32.8 ks for FPMB. We identify a weak source in FPMB and extract source counts from both FPMs using a circular region of radius 20″. Background counts were extracted from similar regions as described above.

Source and background lightcurves were extracted in the 3–6, 10–20, and 3–79 keV energy ranges in time bins of 150 and 500 s. Spectra were grouped to a minimum of 1 count per energy bin. Photon arrival times were barycenter-corrected using the latest clock file (Clock Correction file v209, released on 2025 July 15).

2.3. Chandra X-Ray Observatory

We carried out a late-time X-ray observation with the Chandra X-ray Observatory (CXO) through a DDT request (ObsID: 31011, PI: O'Connor), starting on 2025 August 9 at 05:49:28 UT (corresponding to ∼37.69 days after discovery), for ∼27.7 ks, using ACIS-S (B. O'Connor et al. 2025c). The target was centered at the aimpoint of the S3 chip. The Chandra data were retrieved from the Chandra Data Archive.[26] We reprocessed the data using the `CIAO v4.17.0` data reduction package (A. Fruscione et al. 2006) with `CALDB v4.11.6`. At the subarcsecond location of the near-infrared counterpart (A. J. Levan et al. 2025b), we identify a clear X-ray source. We find 25 counts (0.5–8 keV) in a circular source region with radius 1.″5 centered on the localization obtained with `wavdetect`. We extracted background counts from a nearby source-free region with radius 30″. Using the best-fit X-ray spectrum (Section 3.2), we derive an unabsorbed 0.3–10 keV flux of $(3.3^{+0.7}_{-0.6}) \times 10^{-14}$ erg cm^{-2} s^{-1}. The Chandra data confirm that there are no contaminating point sources within either the Swift or NuSTAR source extraction regions.

Another DDT observation (PI: Eyles-Ferris; R. A. Eyles-Ferris et al. 2025; R. A. J. Eyles-Ferris et al. 2025) occurred, starting on 2025 September 5 at 23:26:41 UT, corresponding to 65.5 days after discovery, using ACIS-S, for a total of 39.55 ks. We analyzed this observation in the same manner, finding 12 counts in a 1.″5 radius, and obtained an unabsorbed 0.3–10 keV flux of $(1.15^{+0.40}_{-0.30}) \times 10^{-14}$ erg cm^{-2} s^{-1}.

3. Analysis and Results

3.1. Analysis of the X-Ray Lightcurve

3.1.1. Temporal Modeling

We modeled the 0.3–10 keV X-ray lightcurve (Swift/XRT and Chandra) with a power law of the form $t^{-\alpha}$ using the `emcee` package (D. Foreman-Mackey et al. 2013). As the exact onset time of the transient is unclear (Table 4), we simplify this consideration by focusing on the start time of the afterglow T_0. This should not be confused with the onset time of the transient, which is set by the first detection by the EP (H. Q. Cheng et al. 2025b; D. Y. Li et al. 2025), despite this early detection preceding the peaks of the X-ray and gamma-ray lightcurves. We use the combined Swift/XRT and Chandra X-ray lightcurve to determine the afterglow start time, assuming it decays as a power law. We performed multiple different fits to the data to explore the range of possible afterglow start times and temporal decay rates. We first allowed the afterglow start time T_0 to be a free parameter, then performed an additional fit with T_0 fixed to the first high-energy trigger time (the discovery time) of GRB 250702D by Fermi (see Table 4).

We first modeled the data with a single power law. The early XRT data obtained show significant variability on short timescales, providing scatter around the best-fit power-law decay. We obtain a reduced chi-squared of $\chi^2/\mathrm{dof} = 2.36$ for a fixed T_0 and $\chi^2/\mathrm{dof} = 2.32$ for a free T_0. The poor chi-squared values are the result of the intrinsic variability at early times and can be observed in the bottom panel showing fit residuals in Figure 1 (left). In Figure 1 (left), we show the best-fit power-law decay when allowing T_0 to be free. The best-fit start time T_0 (MJD $= 60858.657^{+0.054}_{-0.063}$) and the general posterior of T_0 values agree with a start time at the peak of gamma-ray activity (E. Neights et al. 2025a). The full posteriors for both fits are shown as corner plots in Figure 14 in Appendix C. The exact inferred power-law slope depends strongly on T_0. These two fits yield similarly steep slopes and agree at the $\sim 1.5\sigma$ level, favoring an X-ray lightcurve decay of between $\approx t^{-1.7}$ to $t^{-1.9}$.

We performed these fits both with and without the inclusion of the initial XRT orbit at <0.55 days after discovery (see Figure 14 in Appendix C). We demonstrate that the initial XRT observation shows flaring activity (Section 3.1.2) and may bias the temporal analysis. Ignoring the initial flaring episode does not significantly change the inferred decay slope (see Figure 14 in Appendix C), but it does shift the inferred value of T_0 (Figure 1, right) toward earlier times. This demonstrates that the exact decay slope and afterglow start time depend strongly on the assumptions taken for the origin of the X-ray lightcurve.

While it is standard in GRB afterglow modeling to take the initial trigger time as the afterglow start time T_0, in this case, the start time is complicated by the early 2025 July 1 detection (H. Q. Cheng et al. 2025b; D. Y. Li et al. 2025). We performed comprehensive temporal fits to investigate the onset of the afterglow component. That the posteriors of the afterglow onset times agree with the later gamma-ray triggers, as opposed to the first detections by the EP, is slightly unexpected but clearly depends on the choice of power law versus broken power law (Figure 15 in Appendix C). If the true onset time occurred 24 hr earlier, on 2025 July 1, then the inferred initial power-law decay is significantly steeper ($\sim t^{-3.5}$), and a break to a shallower slope ($\sim t^{-5/3}$) would be required to match the late-time X-ray data (see Figure 15 in Appendix C). This is plausible, since the early emission is likely flaring, which then subsides to reveal the slowly fading afterglow. However, the simplest explanation is that either the onset of the relativistic jet's interaction with its surrounding environment occurs around the peak of gamma-ray activity or that the bulk of its energy is released at this phase, in either case leading to a single-power-law afterglow decay. As the trigger of GRB

---

[26] https://cda.harvard.edu/chaser/

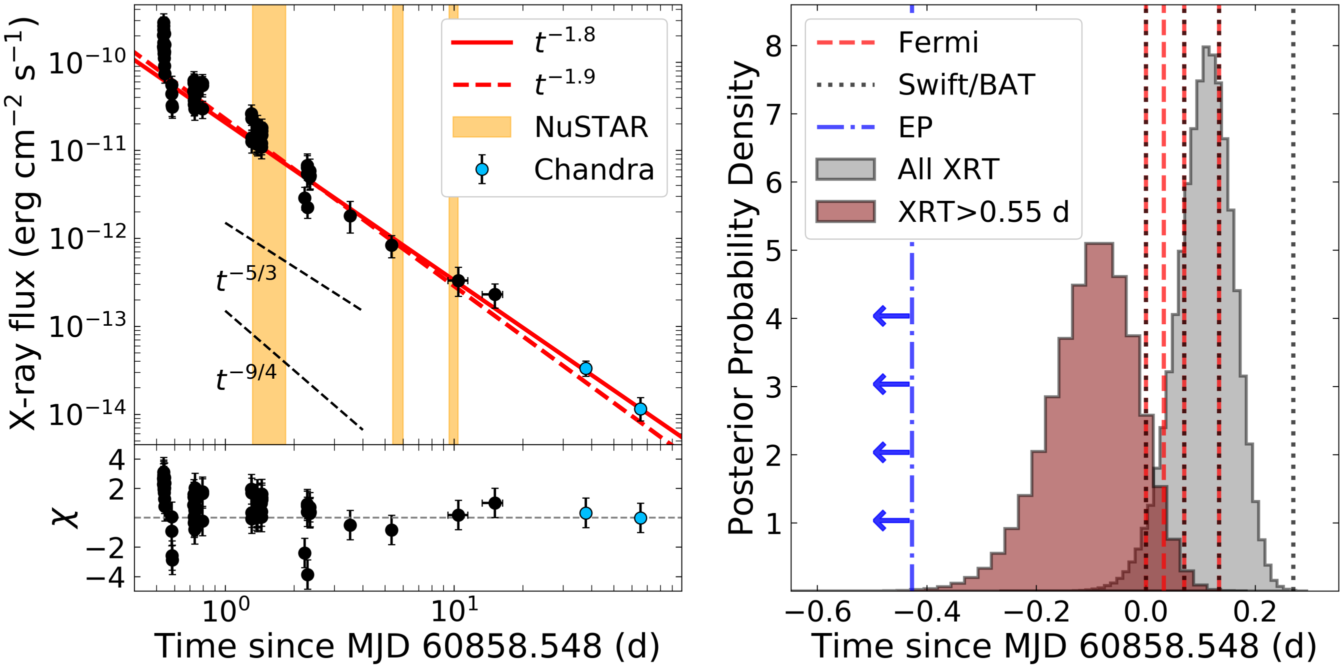

Figure 1. Left: X-ray lightcurve of GRB 250702B combining Swift and Chandra in the 0.3–10 keV energy range. The start time T_0 is the GBM "D" burst. The red lines show the best-fit decay from the initial trigger time of GRB 250702D (Table 4). The dashed red line ($t^{-1.9}$) includes the first XRT orbit in the fit, whereas the solid red line excludes the first XRT orbit and provides a better fit to the late-time data ($t^{-1.8}$). The observation windows of our NuSTAR data are shown as the orange shaded regions. For reference, we show the expected slopes for a relativistic TDE, corresponding to both complete ($t^{-5/3}$) and partial ($t^{-9/4}$) disruption. The bottom panel shows the 0.3–10 keV lightcurve fit residuals relative to the solid red line. Right: histogram showing the posterior probability density of the best-fit T_0 time for the X-ray afterglow emission. The gray histogram shows the T_0 posterior obtained when fitting all XRT data, and the red histogram shows the T_0 posterior when excluding the first XRT orbit. The trigger times reported by Fermi (red) and EP (blue) are shown as vertical lines (Table 4). The July 1 window in which EP reports an initial detection is to the left of the vertical blue line. We also show as vertical black lines the times of the Swift/BAT gamma-ray detections. All times are relative to the trigger of GRB 250702D at MJD 60858.548.

250702E has the highest fluence (i.e., the bulk of the energy release) of the Fermi triggers (E. Neights et al. 2025b, 2025a), it would make sense that this would be favored as the onset time of the jet's afterglow in this context.

Using the trigger of GRB 250702D as T_0, we similarly modeled the NuSTAR 3–79 keV flux (see Section 3.2) across the three epochs (with midtimes of 1.58, 5.70, and 9.98 days; Table 1) with a temporal power-law model. We derive a temporal index of $\alpha = 2.26 \pm 0.15$. This is slightly steeper than, but consistent at the $\sim 2\sigma$ level with, the XRT fit using the same fixed start time (see Figure 14 in Appendix C). We note that the NuSTAR data are limited to three epochs, and the third epoch suffers from large error bars, which suggests that the slope derived from the combined Swift and Chandra lightcurve is more accurate. The first epoch of NuSTAR data also suffers from flaring (see Section 3.1.2), which can also explain its higher flux that can lead to a steeper inferred slope. The shallower slope measured from Swift and Chandra is also more consistent with the early Swift/BAT Survey mode upper limits (see Section 2.1.1 and Table 2). This is shown in Figure 2. While the NuSTAR extrapolation goes through two BAT detections of the prompt emission, this depends strongly on the assumed temporal slope, and we emphasize the BAT detections are not included in the fit.

3.1.2. Short-timescale X-Ray Variability

Our initial NuSTAR observation starting at $T_0 + 1.3$ days and extending to 1.9 days after the initial Fermi trigger ("D" burst), shows significant X-ray variability on $\sim$1–2 ks timescales. In Figure 3, we show the 3–79 keV lightcurve (300 s bins, FPMA +FPMB) of GRB 250702B. The observed X-ray variations are seen in both FPMs independently (Figure 16 in Appendix D). In particular, in the last good time interval (GTI), the count rate drops significantly (see the residuals in the bottom panel of Figure 3). The difference between the end of the second-to-last GTI and the start of the last GTI is 3.7 ks (observer frame), which is taken to be a conservative upper bound to the minimum variability timescale at this phase. This implies $\Delta T/T < 0.03$, which is difficult to produce by emission from an external shock and implies that there is late-time central engine activity extending out to $\sim 1.6 \times 10^5$ s (observer frame). We confirmed that this variability is unrelated to the particle background during the observation by applying different combinations of SAA filtering and selecting different background regions for background lightcurve generation and subtraction. The background lightcurve is also shown for comparison in Figure 3 for FPMA+FPMB and in Figure 16 for both FPMA and FPMB individually.

In Appendix D, we describe our analysis of past NuSTAR observations of GRB afterglows (e.g., GRB 130427A and 221009A), which do not display short-term X-ray variability (see also Figure 17 in Appendix D). We compute the reduced chi-squared with regard to the mean count rate in each observation, finding $\chi^2/\text{dof} \approx 1.0$ for these other GRBs. This compares to $\chi^2/\text{dof} = 2.8$ for GRB 250702B (Figure 16 in Appendix D), demonstrating that the source is significantly more variable on short timescales. Even excluding the last GTI, where a steep drop in the count rate is clearly observed, we find $\chi^2/\text{dof} = 1.9$. The reduced chi-square depends on the binning, as larger time bins reduce the errors and lead to larger

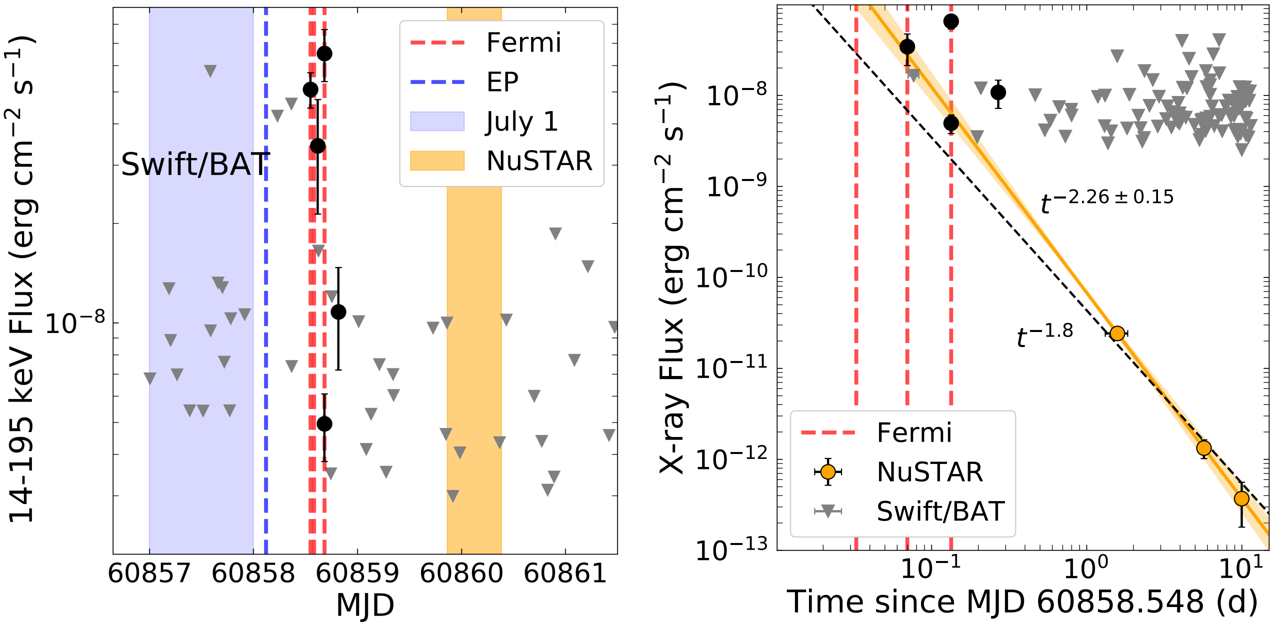

Figure 2. Left: Swift/BAT Survey mode (14–195 keV) emission from GRB 250702B from the start of 2025 July 1 to the end of 2025 July 4. The black points show the Swift/BAT detections (14–195 keV; Tables 2 and 3) from both the `GUANO` and survey data. The gray downward triangles represent the 5σ upper limits from Swift/BAT in the 14–195 keV energy range. The trigger times reported by Fermi (red) and EP (blue) are shown as vertical lines (Table 4). The 2025 July 1 window in which EP reported an initial detection is shown as the blue shaded region. The time window of our initial NuSTAR observation (starting 1.3 days after the initial Fermi trigger) is shown as the orange shaded region. Right: best-fit temporal power law to the NuSTAR lightcurve in 3–79 keV. The 1σ error on the fit is shown as the shaded orange region. The Swift/BAT upper limits are shown as the gray triangles and the detections as black circles. The start time T_0 is taken as the trigger time of GRB 250702D. The vertical red lines show the Fermi trigger times of GRBs 250702B, 250702C, and 250702E (see Table 4).

values of the reduced chi-squared, as seen in Figure 3 (300 s bins), where $\chi^2/\text{dof} = 9.6$. We note that while Figure 3 uses 300 s bins for visualization purposes, our comparison to the GRB variability in Appendix D was consistently performed using 150 s bins for both GRB 250702B (Figure 16 in Appendix D) and the other GRBs (Figure 17 in Appendix D).

In addition, the existence of short-timescale variability is independently supported by the early Swift/XRT data, where the count rate is high enough to have short time bins (Figure 4). In the initial XRT orbit, we find significant flaring and changes in the HR (Figure 4 and Appendix E). The correlated change in HR is typical of flaring activity and in contrast with afterglow emission. The observed flares have a duration of ∼ 150 s at ∼0.54 days (the observed time since the "D" burst). This leads to a very short-variability timescale of $\Delta T/T \approx 0.003$, where ΔT is denoted as the difference (T_{start}–T_{stop}) between the start T_{start} and stop T_{stop} of the flare divided by the observed peak of the flaring activity T_{peak} (e.g., C. A. Swenson & P. W. A. Roming 2014). We note that this is extremely fast even for X-ray flares observed in GRBs, which also generally have higher amplitudes (P. A. Curran et al. 2008; M. G. Bernardini et al. 2011; R. Margutti et al. 2011; C. A. Swenson & P. W. A. Roming 2014).

In order to explore the nature of the variability observed by NuSTAR (Figure 3), we cross-correlated the NuSTAR data with simultaneous XRT data covering the first few orbits. This is displayed in Figure 5, where the XRT count-rate lightcurve has been rescaled to the expected NuSTAR 3–79 keV count rate, based on the observed joint XRT and NuSTAR spectral fit. See Section 3.2 for details of the spectral modeling and its results. We emphasize that this scale factor is not arbitrary and is derived using the `PIMMS` software.[27] This scale factor provides good agreement between the simultaneous XRT and NuSTAR data. We then compared these data to the best-fit power-law decay for the soft-X-ray data (Figure 1 and Section 3.1.1), which was also rescaled using the same factor. We caution that this scale factor depends on the spectral shape, which likely changes as a result of the observed X-ray variability (Figure 4), although we do not find strong evidence for this in the NuSTAR data (Figure 18 in Appendix E). Regardless, in Figure 5, the NuSTAR data show a clear excess above the extrapolation of the XRT data. We therefore interpret the NuSTAR variability as late-time flaring activity with a duration of ∼1–2 ks, requiring late-time central engine activity out to ∼2 days (observer frame). However, due to the variability, we cannot conclude whether the power-law fit to the XRT data is setting the continuum level of an external shock afterglow (serving as a baseline for the flares) or whether it is accretion-driven emission originating from an internal dissipation region within the relativistic jet (see Section 4.3). We note that while the last NuSTAR GTI could be interpreted as a sharp drop in flux, we do not have clear evidence for the short-timescale sharp "dips" in flux (by a factor of ∼10) observed from Sw J1644+57 (J. S. Bloom et al. 2011; D. N. Burrows et al. 2011; A. J. Levan et al. 2011). We discuss both possible interpretations of the X-ray lightcurve further in Sections 3.3 and 4.2.

In order to more robustly explore the variability, we made use of a Bayesian Blocks approach (J. D. Scargle 1998; J. D. Scargle et al. 2013). We extracted NuSTAR lightcurves from FPMA and FPMB in the 3–30 keV energy range using the standard `nuproducts` task, which applies the usual instrumental corrections for exposure, aperture/point-spread function, and vignetting. After restricting the data to overlapping intervals of the two sets of GTIs (FPMA and FPMB),

---

[27] https://heasarc.gsfc.nasa.gov/cgi-bin/Tools/w3pimms/w3pimms.pl

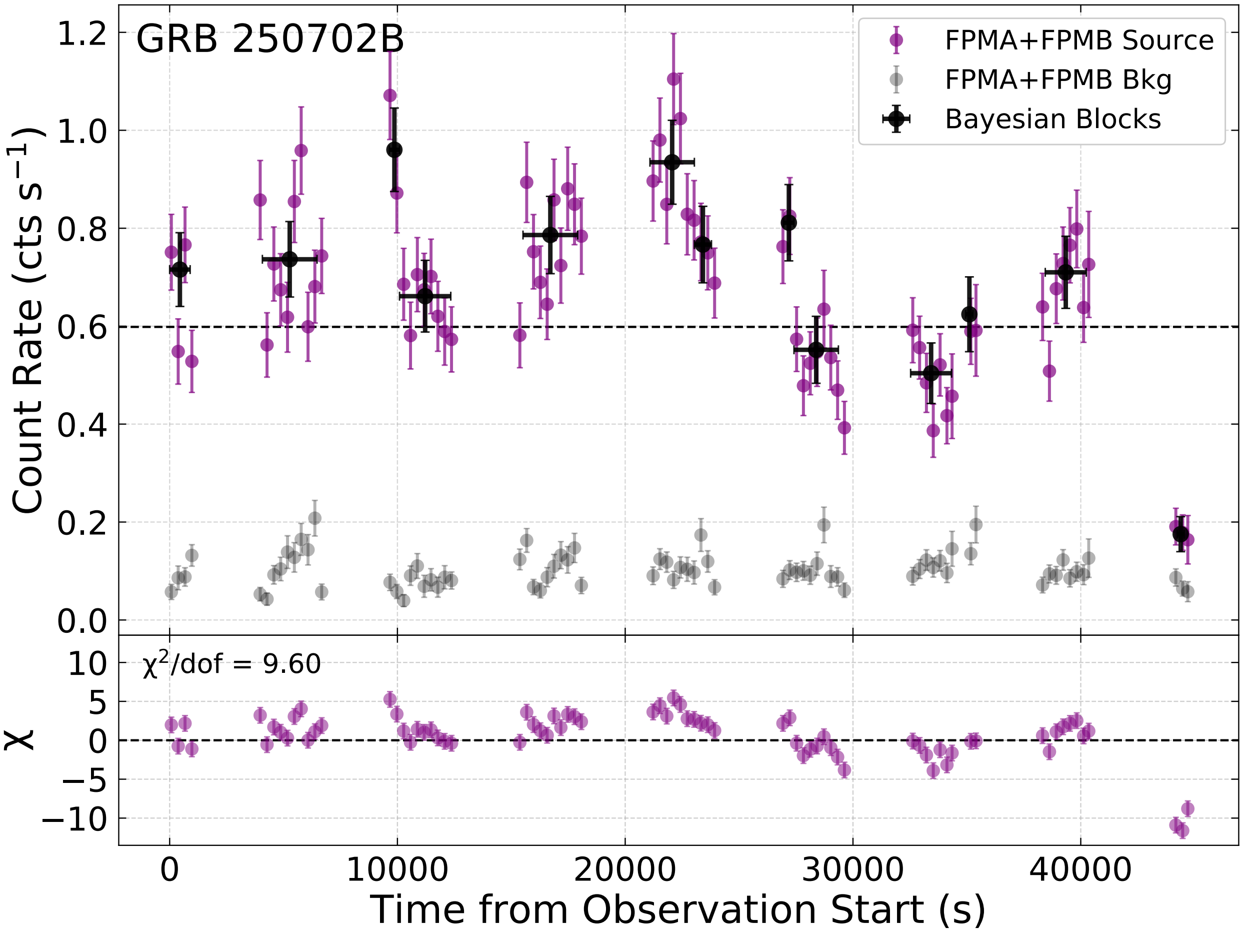

Figure 3. The 3–79 keV NuSTAR lightcurve (FPMA+FPMB) in 300 s bins (purple). The lightcurve is not background-subtracted, but the background lightcurve (gray) is also shown for comparison. The dashed black line shows the mean count rate. The Bayesian Blocks results are shown as the larger black circles. The bottom panel shows the residuals with respect to the mean count rate, to underscore the source's short-timescale variability.

we combined the lightcurves from both detectors and rebinned them to 300 s, in order to improve the signal-to-noise ratio. Uncertainties were propagated in quadrature. We then performed a Bayesian Blocks analysis on the combined lightcurve on a per-GTI basis, adopting a false-positive probability parameter of $p_0 = 0.05$. This choice corresponds to a 5% chance that any detected change point is spurious, thereby balancing sensitivity to genuine variability against the risk of oversegmentation (see, e.g., J. D. Scargle 1998 for more details on Bayesian Blocks). The Python implementation provided in `astropy.stats.bayesian_blocks`[28] was used, with uncertainties incorporated through the `sigma` input parameter. For comparison, we also tested the analysis without rebinning, using the combined barycenter-corrected FPMA and FPMB source event files directly with `fitness="events"`, which yielded consistent results in terms of block boundaries. The Bayesian Blocks result is shown in Figure 3 and supports the existence of short-timescale X-ray variability.

3.1.3. Pulsation Search

We carried out a pulsation search for periodic X-ray signals. We analyzed the barycenter-corrected event files for both FPMA and FPMB individually, as well as the combined event

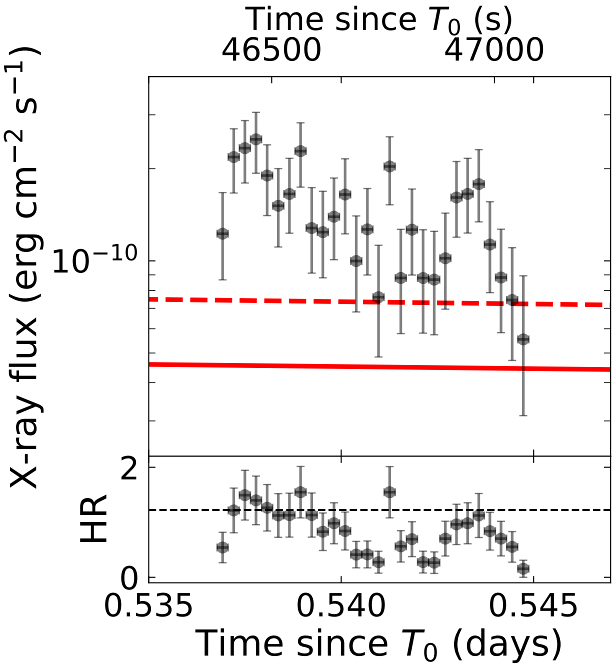

Figure 4. A zoom-in on the early Swift/XRT lightcurve using 25 s bins. The start time T_0 is the GBM "D" burst. The red lines are the same as in the temporal fit shown in Figure 1 (left). The HR between 2–10 and 0.3–2 keV is shown in the bottom panel. The dashed black line shows the mean HR of the full lightcurve.

---

[28] https://docs.astropy.org/en/stable/api/astropy.stats.bayesian_blocks.html

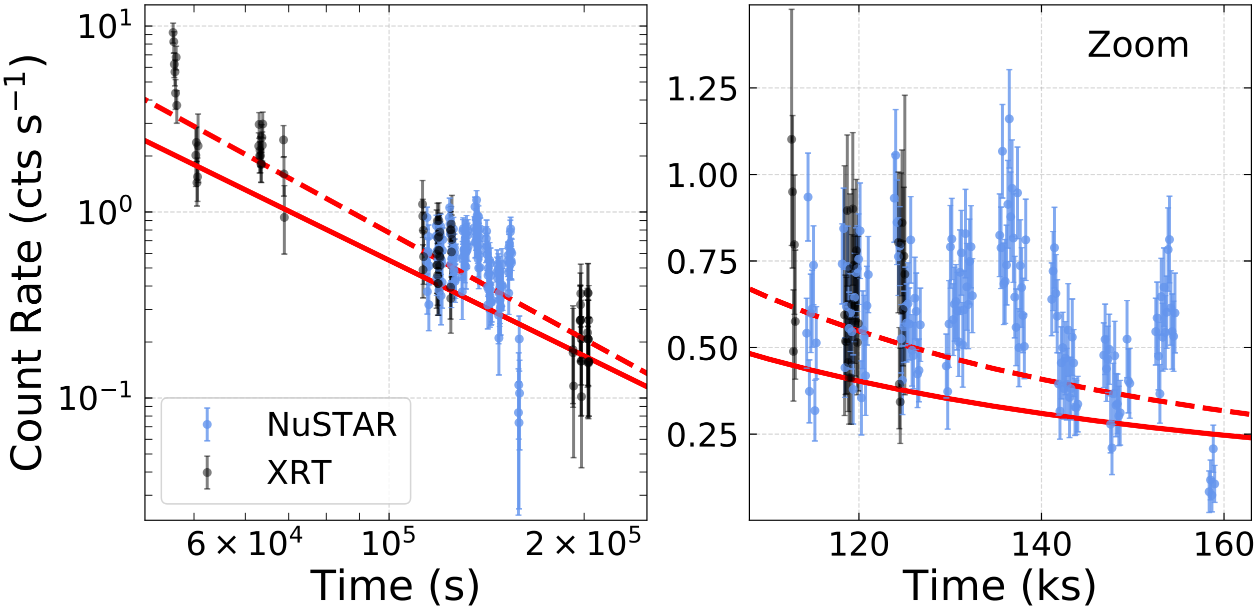

Figure 5. Left: X-ray lightcurve comparing NuSTAR (FPMA+FPMB) data to the XRT lightcurve and best-fit temporal power law as shown in Figure 1. The start time T_0 is the GBM "D" burst. The solid red line is the best fit ($t^{-1.7}$) when including only XRT at >2.5 days, and the red dashed line is the best fit ($t^{-1.9}$) when including all XRT data. The NuSTAR data are in 150 s bins and the XRT data are in 100 s bins. The XRT count rate and power-law fit are rescaled to their expected NuSTAR 3–79 keV count rate. We emphasize that this scale factor is not arbitrary and is computed directly based on the best-fit spectral shape (Section 3.2). Right: the same as the left panel but zoomed in on the NuSTAR data in linear space. Note that the temporal axis is in units of kiloseconds in this panel.

file, to search for coherent periodicity. The event files were filtered to contain only the source region using `xselect`. We performed a Lomb–Scargle periodogram (N. R. Lomb 1976; J. D. Scargle 1982) analysis using a bin size of $\delta t = 0.003$ s to search between frequencies of 10^{-4} to 300 Hz. We also constructed an averaged power spectrum using the `AveragedPowerspectrum` class in `Stingray` (D. Huppenkothen et al. 2019), using 1000 s bins and a bin size of $\delta t = 0.003$ s. We tested multiple different combinations of bins, but the results were unchanged. We performed the same analysis on multiple energy bins, including 3–6, 3–10, 3–20, and 3–79 keV. We do not identify any significant signal (occurring in both FPMA and FPMB or in the combined FPMA+FPMB events list) in the power spectra that exceeds the trial corrected 99.7% CL.

3.1.4. Average Power Spectrum

Motivated by claims of minutes-timescale X-ray quasiperiodic oscillations in some TDEs (e.g., R. C. Reis et al. 2012; D. R. Pasham et al. 2019), we also extracted an average power density spectrum focusing below 0.5 Hz, as follows. We extracted NuSTAR's FPMA and FPMB barycenter-corrected event lists in the 3–30 keV energy band and restricted the data to the intersection of their GTIs, ensuring strictly simultaneous and gap-free coverage. Photon arrival times were binned into 1 s lightcurves, and power spectra were computed on a per-GTI basis using the Leahy normalization (D. A. Leahy et al. 1983), for which purely Poissonian noise corresponds to a flat level of 2 (D. A. Leahy et al. 1983). To balance sensitivity to low frequencies with efficient use of exposure, we adopted a hybrid segmentation scheme: long GTIs were divided into equal segments of length $T_{\rm seg} = 3000$ s, corresponding to a minimum sampled frequency of $1/T_{\rm seg} = 3.3 \times 10^{-4}$ Hz, while shorter GTIs that could not accommodate such segments were retained in full as shorter stretches, contributing only above their respective $1/T_{\rm seg}$ frequency limits. Power spectra from all segments were computed independently and then mapped onto a common uniform Fourier frequency grid, padding with null values below each segment's $1/T$ cutoff to avoid bias at low frequencies. The resulting power spectra were averaged in the Fourier domain, with each frequency bin weighted by the number of contributing segments. Finally, the combined spectrum was logarithmically rebinned into 30 bins across the accessible frequency range, to provide a clearer representation of the broadband variability, and the uncertainties in each bin were estimated as the mean power divided by the square root of the number of independent measurements contributing to that bin. The result is displayed in Figure 6, which clearly shows a red-noise contribution below 2×10^{-3} s, supporting the presence of short-timescale X-ray variability out to 2 days after discovery.

We note that a significantly shorter variability timescale of ~1 s was found in the gamma-ray data from Fermi/GBM (E. Neights et al. 2025a). However, we caution that the low count rate of the NuSTAR data cannot probe 1 s variability timescales, and we cannot determine whether the lack of identified X-ray variability on shorter timescales during our observation is a physical property of the source.

3.2. Spectral Modeling

3.2.1. X-Ray Spectra

We obtained multiepoch NuSTAR observations with simultaneous Swift/XRT coverage (Figure 5), enabling spectral modeling at a midtime of 1.58 days post-trigger across the 0.3–79 keV band. In subsequent epochs, the rapid fading of the X-ray counterpart leads to diminished spectral quality in both instruments, so we restrict our joint spectral analysis to the first epoch only. We additionally performed a fit to the final two epochs of NuSTAR data by themselves.

We modeled all time-averaged X-ray spectra with `XSPEC v12.14.0` (K. A. Arnaud 1996), using the Cash statistic

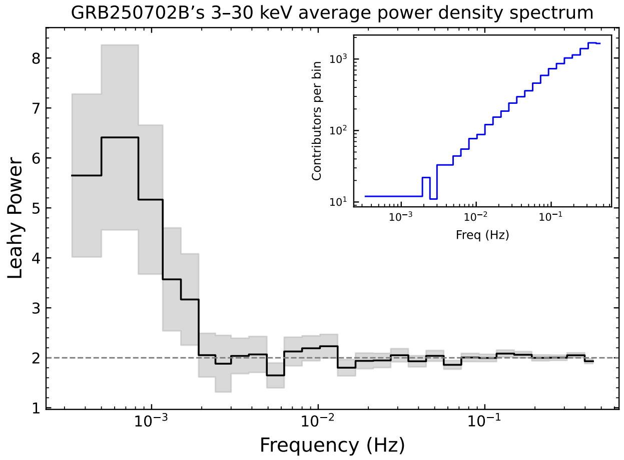

Figure 6. GRB 250702B's 3–30 keV average power density spectrum from NuSTAR FPMA+FPMB data. The black step line shows the mean Leahy-normalized power spectrum, the gray shading indicates 1σ uncertainties, and the dashed line marks the expected Poisson noise level of 2. The inset shows the number of contributing values per frequency bin on log–log axes.

(C-stat; W. Cash 1979), with the interstellar medium abundance table set following J. Wilms et al. (2000) and photoelectric absorption cross sections set following D. A. Verner et al. (1996). All spectra were grouped to a minimum of 1 count per bin. We performed a fit with an absorbed power-law model (`constant*tbabs*ztbabs*pow`) to the NuSTAR (FPMA and FPMB) and simultaneous Swift/XRT data. The normalization of FPMA was fixed to unity, and we allowed the normalization of FPMB to vary to account for cross-calibration uncertainty. The constant normalization of FPMB varied by $\lesssim$3% compared to unity, likely due to a rip in the multilayer insulation of FPMB (K. K. Madsen et al. 2020).

In all fits, we have frozen the Galactic hydrogen column density to $N_{\rm H,gal} = 3.34 \times 10^{21}$ cm^{-2} (R. Willingale et al. 2013). The data were modeled between 0.3–10 keV for Swift and 3–79 keV for NuSTAR. Using an absorbed power-law model, we find an intrinsic hydrogen column density $N_{\rm H,z} = (6.2 \pm 0.8) \times 10^{22}$ cm^{-2} and X-ray photon index $\Gamma = 1.82 \pm 0.03$ with C-stat/dof = 1277/1390. The spectral fit and fit residuals are shown in Figure 7. We do not find evidence for spectral features, such as emission or absorption lines or reflection features. This further supports an extragalactic scenario for GRB 250702B, as it would be peculiar for an X-ray binary in outburst.

We performed an additional fit to the first 24 hr of XRT data. The spectrum was extracted using the XRT Build Products tool. We similarly modeled the data using an absorbed power law: `tbabs*ztbabs*pow`. We find an intrinsic hydrogen column density of $N_{\rm H} = (3.5^{+1.2}_{-1.1}) \times 10^{22}$ cm^{-2} with a photon index $\Gamma = 1.57 \pm 0.17$. We note that the derived ECF (Section 2.1.2) of 8.68×10^{-11} erg cm^{-2} cts^{-1} differs by $\sim$5% compared to that derived by the automatic LSXPS tools (9.07×10^{-11} erg cm^{-2} cts^{-1}) when not including an intrinsic absorber at $z = 1.036$ (B. P. Gompertz et al. 2025). In any case, the derived photon index from NuSTAR ($\Gamma = 1.80 \pm 0.03$) is steeper than that derived from the XRT data (Section 2.1.2; J. A. Kennea et al. 2025). While this is only a $\sim 1\sigma$ deviation, we note that the initial observation with the EP Follow-up X-ray Telescope (FXT) at $\sim$0.5 days, occurring near-simultaneously to the first orbit of XRT data, yielded a photon index of $\Gamma = 1.57 \pm 0.07$ (H. Q. Cheng et al. 2025a), which is a more significant deviation. However, it is necessary to note that these other spectra occur at earlier times (0.5 versus 1.6 days), and we can neither confirm nor rule out an evolution of the photon index.

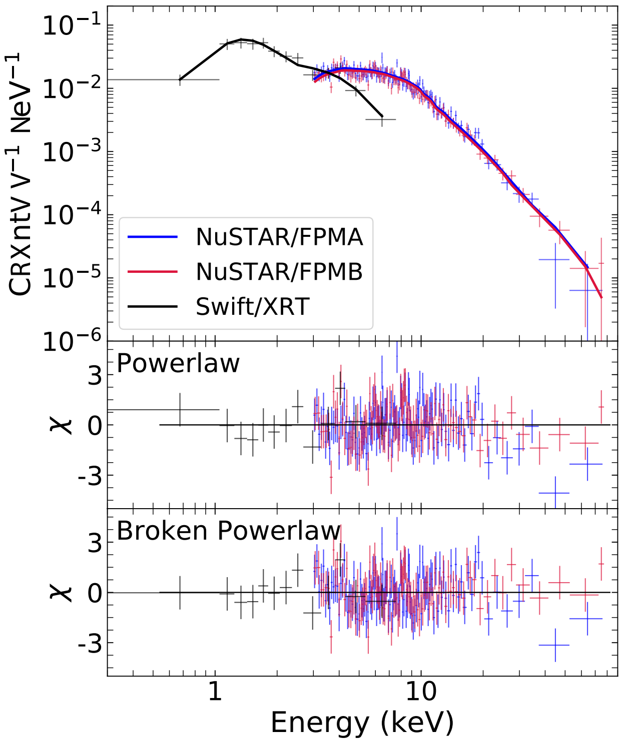

Figure 7. Joint spectral fit including Swift/XRT (black) and NuSTAR FPMA (blue) and FPMB (red) in the 0.3–30 keV energy range. The middle panel displays the fit residuals for an absorbed power-law model, and the bottom panel shows the fit residuals for an absorbed broken power law. The data have been rebinned within `XSPEC` for visualization purposes.

In order to explore whether the steeper index can be explained by a spectral break within the NuSTAR band, we further tested a broken-power-law model (`bknpow`). The spectral break energy $E_{\rm br}$ is measured in the observer frame. This yields $N_{\rm H,z} = (5.0 \pm 0.8) \times 10^{22}$ cm^{-2}, an initial photon index of $\Gamma_1 = 1.64 \pm 0.07$, and a later photon index of $\Gamma_2 = 1.97 \pm 0.06$, with a break at $E_{\rm br} = 8.3^{+0.8}_{-0.5}$ keV. The fit has C-stat/dof = 1260/1388. We then added the requirement that the deviation between the initial photon index Γ_1 and the later photon index Γ_2 is 0.5, as expected from synchrotron radiation with a cooling break in the X-ray band ($\Delta\beta = 0.5$; R. Sari et al. 1998; J. Granot & R. Sari 2002). We find $N_{\rm H,z} = (4.4 \pm 0.7) \times 10^{22}$ cm^{-2}, $\Gamma_1 = 1.55 \pm 0.04$, and $E_{\rm br} = 8.4 \pm 0.6$ keV for C-stat/dof = 1263/1389. The break is identified even if we restrict the X-ray spectra to be fit at only <30 keV. We used the Akaike Information Criterion (AIC) to asses the preferred model between a power law and broken power law. The broken-power-law model is favored with ΔAIC = −12. Spectral breaks in the X-ray range are a property of synchrotron radiation (J. Granot & R. Sari 2002) and are found regularly in GRBs (e.g., R. Filgas et al. 2011; E. Troja et al. 2012). An evolving spectral break was also identified in the relativistic TDE AT2022cmc (Y. Yao et al. 2024).

That said, the evidence is not overwhelming and a single power law provides an adequate fit to the data (Figure 7) without a very noticeable change in the residuals. The benefit of the broken power law is that it solves the early (potential) discrepancy with the initial EP/FXT photon index and is physically motivated. However, we cannot rule out variations in the photon index with time that could allow for a change of 1.6–1.8 in the photon index between 0.5 and 1.6 days.

We also modeled the second and third epochs (with midtimes of 5.70 and 9.98 days, respectively; Figure 2) of NuSTAR data (Table 1). In the second epoch, we derive a power-law photon index of $\Gamma = 1.68 \pm 0.19$ for fixed $N_{\mathrm{H,z}} = 5 \times 10^{22}$ cm^{-2} with C-stat/dof = 126/164. The column density was fixed, as it is unconstrained by NuSTAR alone. We find no evidence for a spectral break, and modeling with a broken power law places the break energy far outside the observed spectral range. We note that the spectrum has a very low signal-to-noise ratio at >20–30 keV. In the third epoch, the source is significantly fainter, and we restrict our spectral modeling to < 30 keV. We derive $\Gamma = 1.86 \pm 0.35$ with C-stat/dof = 93/95.

Additionally, we modeled the spectra of the two Swift/BAT survey detections (see Section 2.1.1 and Table 2) using the χ^2 statistic, as the mask-weighted counts in the spectra follow Gaussian statistics. The spectra are binned into the eight default survey analysis energy bins, ranging from 14 to 195 keV. Using a single-power-law model, we find a photon index $\Gamma = 1.44 \pm 0.38$ and a 14–195 keV flux of $(4.95 \pm 1.14) \times 10^{-9}$ erg cm^{-2} s^{-1} for the first detection occurring shortly after the "E" burst (Table 4) and $\Gamma = 1.77 \pm 0.58$ and a 14–195 keV flux of $(1.08 \pm 0.39) \times 10^{-8}$ erg cm^{-2} s^{-1} for the second detection, starting at ∼0.28 days post-trigger (measured from the "D" burst). We do not find any significant evidence for a high-energy cutoff to the power law in either detection. As the BAT detection is not persistent and clearly fluctuates above the earlier 5σ upper limits (Figure 2), these detections may be associated with late-time central engine activity (e.g., flares). If interpreted as continued prompt emission, this would further extend the duration of the prompt phase (for a discussion, see E. Neights et al. 2025a).

3.2.2. X-Ray-to-near-infrared Spectral Modeling

While the X-ray and near-infrared emission can have various explanations when considered between the progenitor classes of ultralong GRBs and relativistic TDEs, here we evaluate their consistency in coming from the same emission component—namely, an external forward shock (FS). To do this, we investigated the X-ray-to-near-infrared spectral energy distribution (SED) of GRB 250702B, using near-infrared (HK_s bands) detections reported by A. J. Levan et al. (2025b) that were obtained near simultaneously with the midtime of our initial NuSTAR observation (1.58 versus 1.60 days). The source is extremely extinct, due both to dust within our Galaxy ($A_{\mathrm{V}} = 0.847$ mag; E. F. Schlafly & D. P. Finkbeiner 2011) and additional intrinsic dust within its host ($A_{\mathrm{V,z}} > 10$ mag; A. J. Levan et al. 2025b; J. Carney et al. 2025), and only displayed detections in the near-infrared H and K_s bands, despite deep limits at optical wavelengths (J. Carney et al. 2025). We modeled the X-ray-to-near-infrared spectrum with `XSPEC`, using both an absorbed power-law model (`tbabs*ztbabs*zdust*pow`) and a broken-power-law model (`tbabs*ztbabs*zdust*bknpow`). The near-infrared data were corrected for Galactic extinction prior to fitting (E. F. Schlafly & D. P. Finkbeiner 2011). For intrinsic dust within the host galaxy, we utilized a Small Magellanic Cloud (SMC) extinction law with $R_{\mathrm{V}} = 2.93$ (Y. C. Pei 1992) and a redshift $z = 1.036$ (B. P. Gompertz et al. 2025). For the broken power law, we similarly required that $\Gamma_2 - \Gamma_1 = 0.5$. The X-ray data were modeled using a C-stat and the near-infrared data using chi-squared. The total fit statistic was minimized by the fit.

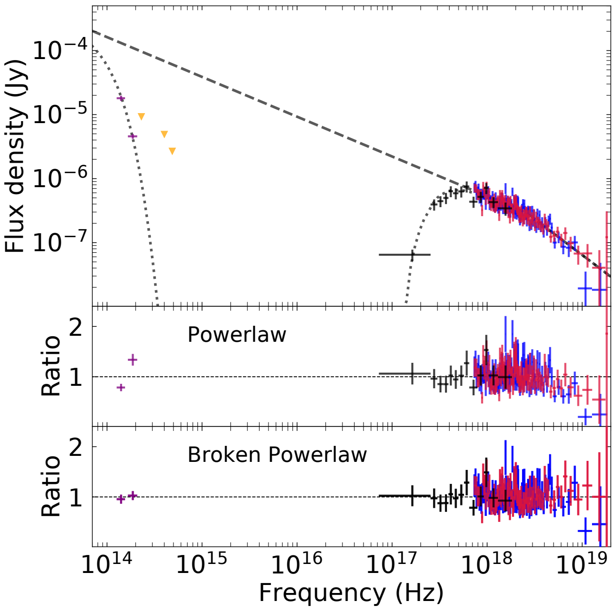

Figure 8. Observed X-ray-to-near-infrared SED with Swift/XRT (black), NuSTAR FPMA (blue) and FPMB (red), VLT HAWK-I (*HK* bands; purple; A. J. Levan et al. 2025b), and optical upper limits (*riJ* bands; orange; J. Carney et al. 2025). The middle panel displays the fit residuals for an absorbed power-law model, and the bottom panel shows the fit residuals for an absorbed broken power law.

For a single power law between 10^{14} and 10^{19} Hz, we derive $N_{\mathrm{H,z}} = (5.3 \pm 0.7) \times 10^{22}$ cm^{-2}, $\Gamma_{\mathrm{XIR}} = 1.72 \pm 0.04$, and reddening $E(B-V)_z = 3.07 \pm 0.20$ mag, with a total fit statistic of 1300 for 1391 degrees of freedom (dof). The reduced chi-squared is $\chi^2/\mathrm{dof} = 1.32$. For $R_{\mathrm{V}} = 2.93$, the derived visual extinction is extremely large: $A_{\mathrm{V,z}} = R_{\mathrm{V}} \times E(B-V)_z = 9.0 \pm 0.6$ mag. The required visual extinction is a strong function of the dust law, assumed redshift, and near-infrared-to-X-ray spectral index. The lack of optical or near-infrared detections at frequencies higher than the H band is also a factor.

A broken-power-law fit yields $N_{\mathrm{H,z}} = (3.0 \pm 0.6) \times 10^{22}$ cm^{-2}, $\Gamma_{\mathrm{XIR,1}} = 1.64 \pm 0.03$, $E_{\mathrm{br}} = 10.9^{+1.5}_{-1.1}$ keV, and reddening $E(B-V)_z = 2.25 \pm 0.20$ mag, with a total fit statistic of 1264 for 1390 dof. The reduced chi-squared is $\chi^2/\mathrm{dof} = 1.14$. The visual extinction is $A_{\mathrm{V,z}} = 6.6 \pm 0.6$ mag. This fit and residuals are shown in Figure 8. Based on the total fit statistic and the residuals, we favor the broken-power-law fit as providing a better description of the X-ray-to-near-infrared data at ∼1.6 days. The derived spectral index is also consistent with the initial XRT and EP/FXT data.

We caution that (while clearly significant) the exact dust contribution is uncertain and here depends on the assumption that both the near-infrared and X-ray data originate from the same emission component. However, this is unclear and not required by the data. It may simply be possible due to the additional free parameter of dust, which can modify the observed near-infrared spectral index to a broad range of intrinsic spectral indices. In addition, the X-rays are flaring at the time the spectra were acquired (which may require slightly more dust to match the higher flux level), but this is not necessarily going to impact the near-infrared emission, especially if that originates from an external shock.

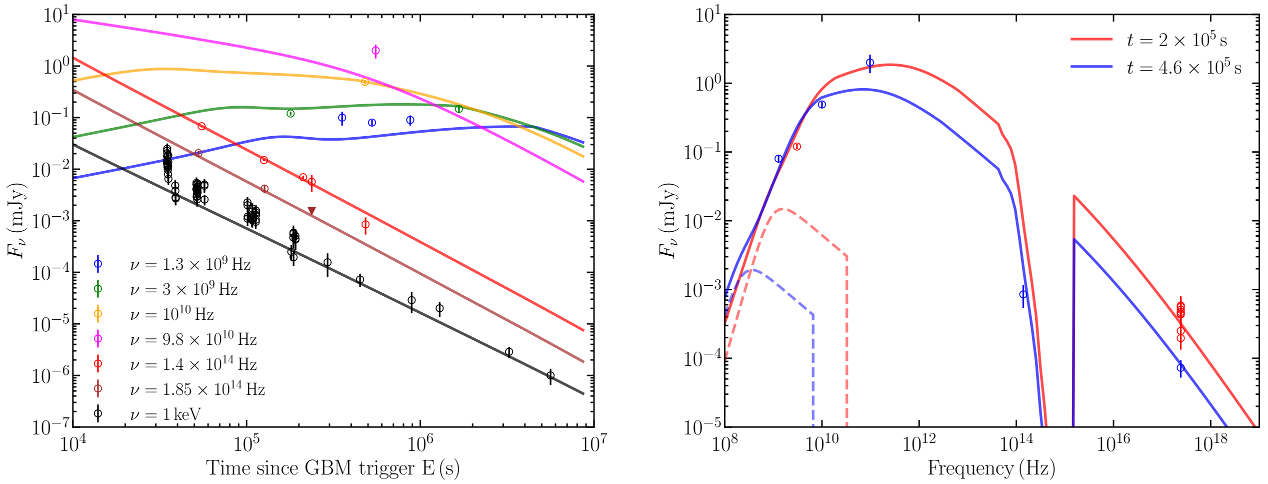

Figure 9. Left: FS and RS afterglow models fit to multiwavelength observations. The start time T_0 is the GBM "E" burst. The Markov Chain Monte Carlo parameter posterior distributions are shown in Figure 20, which only considers the last five X-ray detections for the X-ray lightcurve. The lightcurves are obtained for the following model parameters that keep the X-ray afterglow emission below the flaring X-ray emission at early times: $\theta_j = 7.8 \times 10^{-3}$ rad, $E_{\rm k,iso} = 6.2 \times 10^{54}$ erg, $\Gamma_0 = 306$, $n_0 = 0.6$ at $R_0 = 10^{18}$ cm, $p = 2.1$, and $\epsilon_e = 0.2$, $\epsilon_B = 10^{-3}$, $k = 2$. The same dynamical parameters are used for the RS emission with these shock microphysical parameters: $p_{\rm RS} = 2.2$, $\varepsilon_{e,\rm RS} = 0.1$, $\varepsilon_{B,RS} = 10^{-3}$, $t_{\rm grb} = 10^3$ s, and $g_{\rm RS} = 2.0$. The start time T_0 is taken as GRB 250702E (Table 4). Right: model spectra comparisons with observations at two different times, with the RS spectra shown with dashed lines.

3.3. Broadband Afterglow Modeling

The interaction between the local environment and the relativistic jets launched by both GRBs and jetted TDEs produces a broadband (radio-to-gamma-ray) synchrotron afterglow (R. Sari et al. 1998; J. Granot & R. Sari 2002). We modeled the multiwavelength lightcurves of GRB 250702B using the standard fireball model (P. Mészáros & M. J. Rees 1997; R. A. M. J. Wijers & T. J. Galama 1999; J. Granot & R. Sari 2002), using the numerical methods of R. Gill & J. Granot (2018, 2023) to compute the FS and reverse-shock (RS) emission from a nonspreading top-hat jet.

The FS model depends on the isotropic-equivalent kinetic energy of the outflow $E_{\rm kin}$ at the jet's core, the. initial bulk Lorentz factor Γ_0 at the jet's core, the jet core's half-opening angle $\theta_{\rm j}$, the surrounding density $n_{\rm ext}$, the slope of the electrons' power-law energy distribution p, and the microphysical parameters ε_e and ε_B that determine the partitioning of the shock energy in the electrons and magnetic fields, respectively. The RS depends on the additional parameters $p_{\rm RS}$, $\varepsilon_{e,\rm RS}$ and $\varepsilon_{B,\rm RS}$, and $g_{\rm RS}$ (see R. Gill & J. Granot 2023). To explore the nature of the surrounding environment, the power-law slope k and normalization n_0 at $R_0 = 10^{18}$ cm of the external density profile, $n_{\rm ext} = n_0 (R/R_0)^{-k}$, are left as free parameters. Another parameter that must be specified when modeling the RS emission is the GRB duration, typically T_{90}, that determines the initial radial width of the ejecta, $\Delta_0 = cT_{90}/(1+z)$, to see if a thin-shell (Newtonian RS) or thick-shell (relativistic RS) solution is obtained (R. Sari & T. Piran 1995). With multiple emission episodes in this GRB, which are also separated by long quiescent periods, the initial radial width of the ejecta is unclear. Therefore, we assume a thin-shell scenario, in which the RS and FS afterglow lightcurve peak times do not exactly coincide and the FS afterglow peaks later. The FS+RS afterglow model therefore depends on 12 free parameters.

We supplemented our X-ray data set with radio data compiled from GCN Circulars (K. D. Alexander et al. 2025; P. Atri et al. 2025; A. Balasubramanian et al. 2025; N. Grollimund et al. 2025; A. I. Sfaradi et al. 2025; A. J. Tetarenko et al. 2025), the multiwavelength data presented in A. J. Levan et al. (2025b), and additional optical/near-infrared (OIR) photometry from J. Carney et al. (2025). The OIR photometry was corrected for Galactic extinction prior to fitting (E. F. Schlafly & D. P. Finkbeiner 2011), and an additional intrinsic extinction component using an SMC dust law (K. D. Gordon et al. 2024) was added. We note that the OIR upper limits (J. Carney et al. 2025; A. J. Levan et al. 2025b) are included in the fit but are not displayed in the figures, for clarity. We used the `emcee` (D. Foreman-Mackey et al. 2013) package to fit the broadband afterglow first with an FS-only model. We then used this solution to add the RS afterglow, by manually considering the shock microphysical parameters that yielded a close match to the observations.

We set the start time T_0 of the afterglow as the GBM "E" burst (GRB 250702E occurs only ~0.134 days after the initial trigger GRB 250702D; Table 4)—see Section 5.2 for further discussion of the likely start time. Additional fits were performed using the "D" burst as T_0 and are presented in Figure 21 in Appendix F. They do not modify our overall conclusions and are broadly consistent with the fits using the "E" burst as T_0. We performed another fit using a T_0 that is 1 day prior to the "D" burst, but this does not provide suitable solutions to the multiwavelength lightcurve.

In our fits, we have assumed that the near-infrared data originate from the external shock (although this is not guaranteed; A. J. Levan et al. 2016). We have further assumed that the initial X-ray data at $< 2 \times 10^5$ s (relating to the "E" burst) are significantly contaminated by excess emission from late-time central engine activity. This is supported by the presence of short-term variability in the NuSTAR data out to ~2 days (see Section 3.1.2 and Figures 3 and 5). We therefore have only included the final X-ray points at $>2 \times 10^5$ s in our modeling. It is worth pointing out that the lack of variability inferred from the late-time X-ray data is potentially due simply to the low count rates at that phase. In any case, we note that including all X-ray data in the fit does not significantly modify our afterglow solutions or the inferred parameters.

The best-fit afterglow model is shown in Figure 9 and a corner plot is displayed in Figure 20 in Appendix F.

Regardless of redshift, the conclusion is that the afterglow requires a large (isotropic-equivalent) kinetic energy and an ultrarelativistic jet with a small jet opening angle propagating in a wind-like density profile. The high Lorentz factor is required such that the jet decelerates prior to our first X-ray observations, and the small jet opening angle allows for the afterglow to be in a steep decaying post-jet-break phase throughout all our multiwavelength observations. We discuss these points further in Section 5.2.

We find that the inferred visual extinction from the afterglow model is slightly smaller than derived using `XSPEC` (Section 3.2). The main conclusion that a significant dust column must lie along the line of sight is the same. We find that the difference is likely due to variations in the parameterization of the SMC dust law (Y. C. Pei 1992; K. D. Gordon et al. 2024) and due to the flatter spectral slope favored by the afterglow model, which naturally requires a smaller dust correction. Our broadband spectral modeling (Figure 8) favors a larger value of $p = 2.28 \pm 0.06$[29] compared to the value derived from our afterglow modeling ($p = 2.11 \pm 0.03$). The afterglow model prefers a smaller value of p, so as to provide a better match to the post-jet-break temporal decay slope (see the discussion in Section 5.2). The difference in the p values is likely coming from the integration over the jet's surface of equal arrival times that is done in the afterglow model compared to the spectral fit that simply assumes line-of-sight emission. However, these two values of p only deviate by $\sim 2\sigma$ and neither is inconsistent with the data.

We note that the afterglow model (Figure 9, right) places the cooling frequency $\nu_{\rm c}$ in or near the X-ray band at a consistent frequency, with our observations of a spectral break based on an analysis of the X-ray-to-near-infrared SED (Figures 7 and 8). This provides support for the presence of a break in the SED. As the jet model used here is nonspreading,[30] even after the jet break the cooling frequency continues to evolve with the same dependence $\nu_{\rm c} \propto t^{(3k-4)/2(4-k)}$, which is $\sim t^{0.3}$ to $t^{0.5}$ for our preferred environment. We see this in the right panel of Figure 9. Evolving the observed $\sim$10 keV break at 1.6 days (observer frame) back in time places it at the upper end of the XRT band ($\sim$6–7 keV) during the first orbit of XRT data. It would also evolve the cooling frequency to $\sim$17–25 keV by the time of our second NuSTAR observation, likewise allowing it to be missed due to limited counts (low signal-to-noise ratio) above those energies. If instead the jet is spreading laterally, then the cooling frequency would be frozen in place during the course of all our observations and even more easily missed in the initial XRT spectra. An additional point is that the cooling frequency is likely smooth over at least an order of magnitude in frequency, such that minor changes in the frequency are not noticeable on the short timescales probed by XRT and NuSTAR.

We find that the radio data, except for Atacama Large Millimeter/submillimeter Array observations at $\nu = 98$ GHz (K. D. Alexander et al. 2025), are well explained by our model and are dominated by the FS emission. This is in contrast with the modeling of A. J. Levan et al. (2025b), who attribute all of the radio afterglow to RS emission. Continued radio monitoring is crucial for fully measuring the evolution of the radio emission and accurately constraining the FS and RS contributions.

4. The Peculiar High-energy Properties of GRB 250702B

GRB 250702B is a peculiar ultralong X-ray and gamma-ray transient that does not neatly fit into any class of known high-energy transients (see Section 1 for a summary). Its properties most closely resemble the classes of ultralong GRBs or relativistic jetted TDEs. Here, we focus on a few of its relevant high-energy properties in this context. In Section 5, we consider both of these possible progenitor scenarios and explain why its observed properties are not an exact match to either progenitor class.

4.1. Ultralong Prompt Emission

GRB 250702B displayed unusual prompt emission properties. For starters, it triggered a variety of high-energy monitors multiple times on 2025 July 2, with a gamma-ray duration in excess of 25 ks (see E. Neights et al. 2025a for a detailed discussion). Additional high-energy detections were uncovered on 2025 July 1 by the EP and Fermi, extending the prompt emission duration to longer than a day (H. Q. Cheng et al. 2025b; D. Y. Li et al. 2025; E. Neights et al. 2025a). In fact, Swift/BAT[31] (Section 2.1.1 and Figure 2) also detected the source in Survey mode at two additional instances that followed the Fermi triggers, further pushing the prompt duration[32] (and therefore central engine activity) to extreme values.

As such, the exact start time of the event is unclear, though our analysis favors an afterglow onset timed with the 2025 July 2 triggers (Figure 1, right). The delay between the 2025 July 1 and July 2 detections is unusual for GRBs, which have never before been found to have such a long delay between the early "precursor" emission and the main burst episode. It is possible that this is a selection bias, due to the lack of widefield soft-X-ray monitors like the EP in the past. It is therefore possible that some previously known ultralong GRBs also show such subenergetic precursor emission that was missed. However, the EP lightcurve shows a smooth rise to peak emission (D. Y. Li et al. 2025), coinciding with the final Fermi trigger (E. Neights et al. 2025a), which excludes its interpretation as a "precursor." In any case, such underlying soft-X-ray emission would easily be missed in previous ultralong events.

While these properties are atypical for GRBs, they have likewise never been observed from a relativistic TDE. While relativistic TDEs have been uncovered in binned gamma-ray data (S. B. Cenko et al. 2012; G. C. Brown et al. 2015) or 1000 s long image triggers (D. N. Burrows et al. 2011; T. Sakamoto et al. 2011), they have never triggered high-energy monitors in the standard "rate" trigger method that detects typical GRBs, and they have definitely not done so multiple times in a 24 hr window. As near all-sky gamma-ray

---

[29] This value is derived from spectral fits including data that exhibit flaring episodes (Figure 5) and therefore may differ from the SED of the external shock afterglow.

[30] The condition $\Gamma_0\theta_{\rm j} \geqslant 1$ is enforced to prevent the jet from spreading laterally in the coasting phase (J. E. Rhoads 1997, 1999), which would break its approximation as a spherical outflow. We note that this pushes Γ_0 to high (but not unreasonable) values; see Section 5.2 for discussion. Even relaxing this requirement, we require Lorentz factors in the range $\Gamma_0 \gtrsim 20$–50.

[31] As these Swift/BAT detections occurred prior to the start of the soft-X-ray observations with XRT, their interpretation as either additional prompt episodes or X-ray flares is unclear—although see E. Neights et al. (2025a).

[32] We note that these Swift/BAT detections are included in the 25 ks determination of the prompt emission duration by E. Neights et al. (2025a).

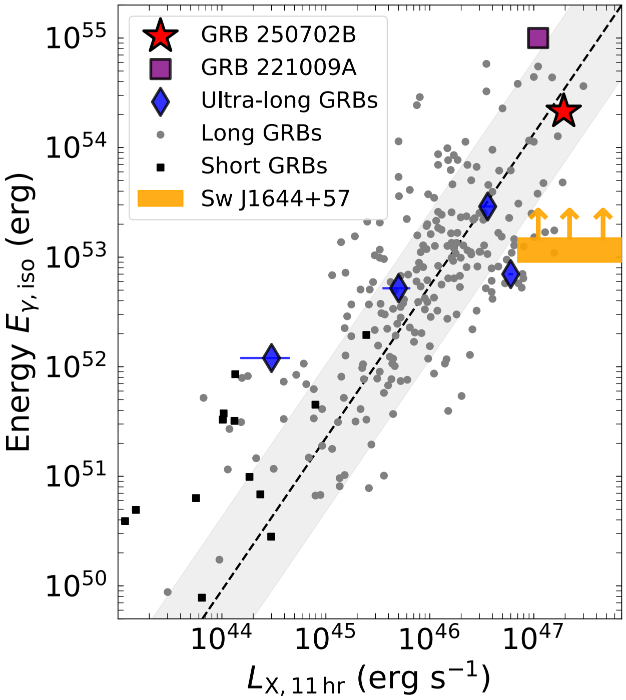

Figure 10. Rest-frame X-ray luminosity (0.3–10 keV) at 11 hr (in the rest frame) from discovery versus gamma-ray energy (1–10,000 keV). GRB 250702B is shown by a red star. We measure 11 hr from the start of the "D" burst (discovery trigger). We show Sw J1644+57 as a shaded region (see the text for details; D. N. Burrows et al. 2011). A sample of short (black squares) and long (gray circles) GRBs are compiled from M. Nysewander et al. (2009) and E. Berger (2014). We show GRB 221009A as a purple square (E. Burns et al. 2023; B. O'Connor et al. 2023; S. Lesage et al. 2023). A sample of ultralong GRBs is shown for comparison (GRBs 101225A, 111209A, 121027A, and 130925A; P. A. Evans et al. 2014a; A. J. Levan et al. 2014). The long-GRB correlation of $L_{\rm X,11} \approx 5.6 \times 10^{44} (E_{\gamma,\rm iso}/10^{51}\,\rm erg)^{0.72}$ erg s^{-1} is shown by the black dashed line (E. Berger 2014). Reproduced from B. O'Connor et al. (2025b).

monitors have been operating for decades, multiple gamma-ray triggers would be more difficult to miss in the past than early soft-X-ray emission that could only have been found by the EP, which launched only in the last 2 yr (W. Yuan et al. 2025). A detailed subthreshold gamma-ray search in the day(s) preceding ultralong GRBs is likely necessary to further investigate this possibility.

An important clue can be obtained from the isotropic-equivalent gamma-ray energy $E_{\gamma,\rm iso}$. The integrated energy obtained by Konus-Wind (D. Frederiks et al. 2025) is $E_{\gamma,\rm iso} = (1.4^{+0.4}_{-0.2}) \times 10^{54}$ erg in the 1–10,000 keV energy range (see also E. Neights et al. 2025a). This is at the high end of the isotropic-equivalent energies found in classical GRBs and ultralong GRBs (see Figure 10). This is also substantially higher than the energy released ($\approx 10^{51}$ erg; 1–10,000 keV) by Sw J1644+57 during its initial Swift/BAT detection (GRB 110328A; T. Sakamoto et al. 2011). The individual energetics of the "DBE" events yield energies a factor of 10 times higher (E. Neights et al. 2025a). However, Sw J1644+57 triggered BAT multiple times over the next 2 days, before BAT triggers were disabled for the source (D. N. Burrows et al. 2011). We estimate the gamma-ray energy during this peak phase by adopting the average fluence reported by D. N. Burrows et al. (2011) over this 2 day window and adopting the spectral shape (peak energy ∼70 keV) reported by A. J. Levan et al. (2011). This yields $E_{\gamma,\rm iso} \approx (1.0 \pm 0.2) \times 10^{53}$ erg in 1–10,000 keV. This value is derived during the peak phase (∼2 days) of Sw J1644+57's emission (in both X-rays and gamma rays), but Sw J1644+57 was detected by BAT both before and after this peak phase (D. N. Burrows et al. 2011). Therefore, our derived energy during this 2 day window is a lower limit to its full gamma-ray energy release. We show this lower limit as an orange shaded region in Figure 10, for comparison to the energetics of GRB 250702B and classical (short, long, and ultralong) GRBs. Another notable difference to GRB 250702B is that the gamma-ray emission from Sw J1644+57 was substantially softer (peak energy ∼70 keV; A. J. Levan et al. 2011) than the >1 MeV emission observed from GRB 250702B (E. Neights et al. 2025a).

In addition, the Fermi data revealed a critical piece of evidence in the minimum variability time. E. Neights et al. (2025a) identified a very short second-duration ($\lesssim 1$ s, observer-frame) variability timescale, which is a factor of 100–1000 smaller than observed in relativistic TDEs (J. S. Bloom et al. 2011; D. R. Pasham et al. 2023). Relativistic TDEs, and accreting BHs in general, are limited by the Schwarzschild light-crossing time $t_s = 2R_{\rm g}/c$, where $R_{\rm g} = GM/c^2$ is the gravitational radius, which depends on the BH mass. As larger masses lead to longer predicted minimum variability timescales, if a massive BH is invoked, it would require a small $\lesssim 5 \times 10^4 M_\odot$ IMBH. It is also important to note that the light-crossing timescale argument is only a lower limit to the minimum variability timescale, and the BH mass determined through this argument for past relativistic TDEs is larger than the latest analysis based on their jet shutoff timescales (T. Eftekhari et al. 2024).

However, we note that relativistic TDEs have been compared to smaller versions of blazars (J. S. Bloom et al. 2011), which have been observed to have variability on timescales less than their light-crossing times (D. Giannios et al. 2009; A. Shukla & K. Mannheim 2020). The shorter-variability timescale observed from blazars has been explained by the "jets in a jet" model (D. Giannios 2013). Whether the same magnetic reconnection mechanism can explain the prompt emission of GRB 250702B is outside the scope of this paper, but we caution that this minijet scenario would mean that the short-variability timescale does not directly constrain the BH mass.

In any case, this seconds-long variability is typical of that observed in long-duration GRBs and would therefore most obviously favor an interpretation that invokes a stellar-mass progenitor, such as in GRBs. As an additional argument, in the collapsar progenitor channel, the central engine for long GRBs is likely a stellar-mass BH (S. E. Woosley 1993). Assuming a $\sim 5 M_\odot$ BH, the predicted minimum variability timescale based on the Schwarzschild light-crossing time is 5×10^{-5} s, which is significantly smaller (by orders of magnitude) than the minimum variability observed in GRBs (see, e.g., 10^{-2}–100 s; V. Z. Golkhou & N. R. Butler 2014). Following this argument, if applied to massive BHs, it would imply the minimum variability from light crossing is significantly smaller than the likely true intrinsic variability that can be observed. We therefore consider the second-duration minimum variability of GRB 250702B (E. Neights et al. 2025a) as strong evidence for a stellar-mass progenitor (Section 5.2).

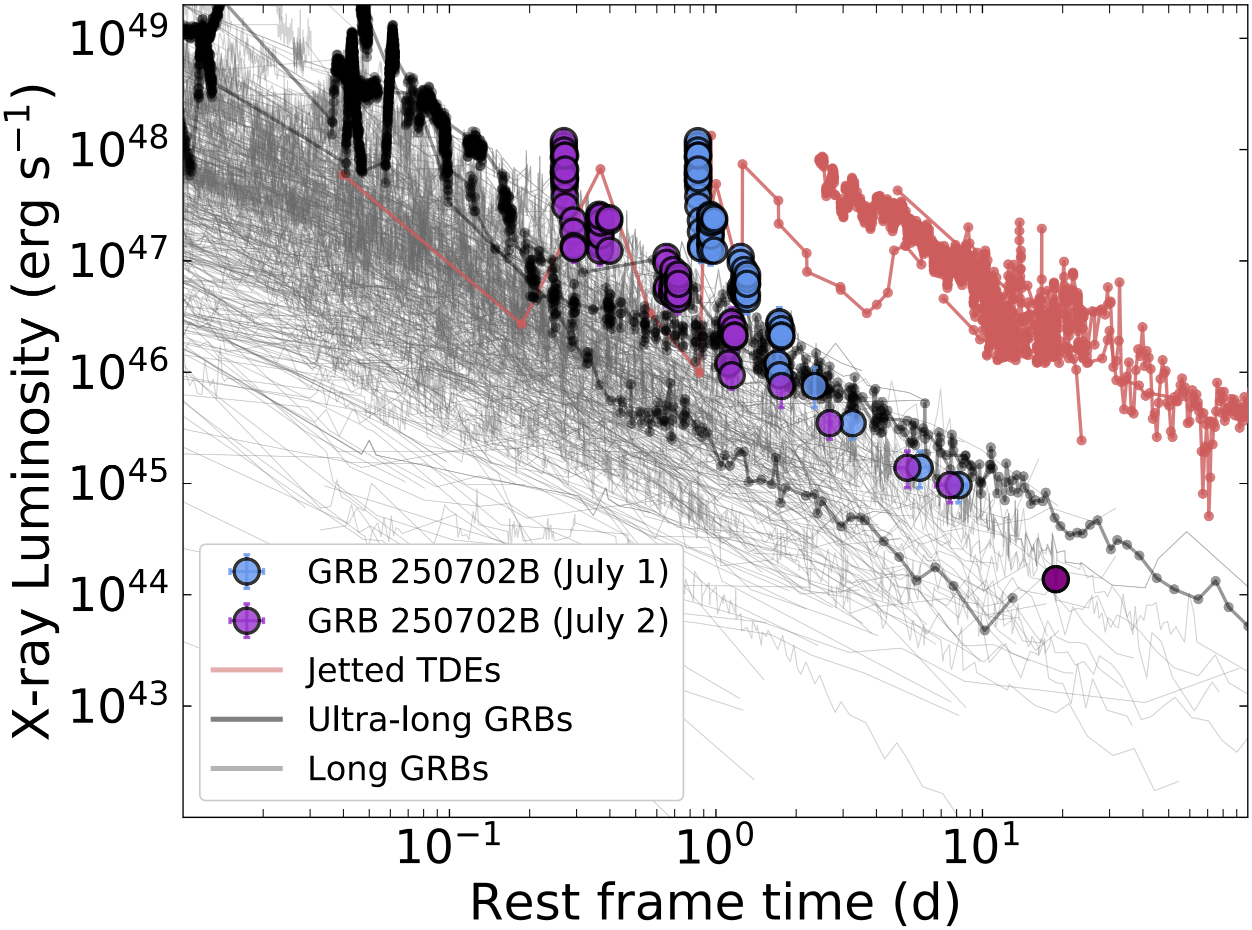

Figure 11. K-corrected rest-frame (0.3–10 keV) X-ray lightcurves of Swift long-duration GRBs, ultralong GRBs (GRBs 111209A, 121027A, and 130925A; P. A. Evans et al. 2014a; A. J. Levan et al. 2014), and relativistic jetted TDEs (J. S. Bloom et al. 2011; S. B. Cenko et al. 2012; G. C. Brown et al. 2015; D. R. Pasham et al. 2023) compared to GRB 250702B for a few different T_0. For the 2025 July 2 start time (purple), we have used the trigger time of GRB 250702D as T_0 (Table 4). For the 2025 July 1 start time (blue), we use the beginning of the first EP detection window (H. Sun 2025, private communication).

4.2. X-Ray Luminosity and Prompt Afterglow Correlations

The X-ray afterglow luminosity as a function of time is a key diagnostic between different classes of energetic transients. It has been used to initially identify between a GRB or TDE origin (e.g., J. S. Bloom et al. 2011; D. N. Burrows et al. 2011; I. Andreoni et al. 2022; D. R. Pasham et al. 2023). In Figure 11, we compare the rest-frame X-ray lightcurve measured by Swift and Chandra to classical long GRBs,[33] ultralong GRBs, and relativistic jetted TDEs. The striking feature is the agreement with the observed luminosities and decay rates of Swift long GRBs.

While we have taken the initial Fermi trigger ("D" burst) as T_0 for this figure, it is possible that the start time is prior to this, despite our temporal modeling favoring otherwise (Figure 1). However, regardless of the start time taken for the event, we are unable to reproduce the long-lived behavior observed in known relativistic TDEs. As shown in Figure 15 in Appendix C, an earlier T_0 requires a very steep initial decay of the X-rays, before returning to a GRB-like luminosity and decay. This additionally would strongly imply an extreme X-ray luminosity (higher than ultralong GRBs or any observed GRB) at >1 day, before quickly returning to GRB afterglow-like levels (Figure 11). While ultralong GRBs show this rapid X-ray decay during the ends of their prompt phases, they have all reached afterglow-like behavior a factor of 2 earlier in time in the rest frame (assuming a 2025 July 1 onset; Figure 11). For these reasons, a much earlier T_0 is hard to believe, especially given the lack of detections in Swift/BAT Survey mode data, even extending to a month before discovery (Section 2.1.1 and Figure 2).

The range of X-ray afterglow temporal slopes (Section 3.1.1 and Figure 14 in Appendix C) is consistent with a range of possibilities, such as fallback accretion for either complete stellar disruption ($t^{-5/3}$) or a post-jet-break afterglow (Section 3.3). The X-ray luminosity clearly falls in the typical range for GRB afterglows and disfavors a classical relativistic TDE (though there are other reasons for this as well; see Section 5.1 for a discussion). While the exact nature of the X-ray emission (i.e., internal versus external) is uncertain (Section 4.3), it is worth noting that this event follows the standard GRB correlations (Figure 10) between the prompt gamma-ray energy and the X-ray luminosity at 11 hr, $E_{\gamma,\mathrm{iso}}$–$L_{\mathrm{X},11}$ (M. Nysewander et al. 2009; E. Berger 2014; B. O'Connor et al. 2020). This correlation (within its scatter) holds for both classical GRBs and ultralong GRBs (Figure 10).

In Figure 10, we consider the X-ray luminosity at 11 hr (rest frame) from the discovery of each transient. Thus, for GRB 250702B, we have adopted the "D" burst as T_0. However, the agreement of GRB 250702B with this correlation depends on

---

[33] https://www.swift.ac.uk/xrt_curves/

the exact afterglow onset time (Figure 1), as adopting an earlier start time (e.g., the initial EP detection) is likely to modify the X-ray luminosity (toward brighter values). In any case, we find that utilizing the "E" burst as T_0 does not modify this conclusion.

Ultralong GRBs also clearly follow this correlation within the observed scatter of classical GRBs. Each of the ultralong GRBs (e.g., GRBs 101225A, 111209A, 121027A, and 130925A) has a gamma-ray duration of $\sim 10^4$ s and displays non-afterglow-like soft-X-ray behavior during this phase (A. J. Levan et al. 2014). Despite their long-lived central engine activity, each of these sources returned to a more standard afterglow behavior with a shallow plateau-like decay by 11 hr (rest frame). That these long-lived peculiar GRBs should also follow the $E_{\gamma,\mathrm{iso}}$–$L_{\mathrm{X},11}$ correlation would circumstantially favor external afterglow emission from GRB 250702B at 11 hr after the initial Fermi trigger. However, this interpretation is complicated by the observed X-ray variability at $\sim$1 day (rest frame), which is another behavior shared by ultralong GRBs at $<10^4$ s (see Figure 3 of A. J. Levan et al. 2014). Instead, it is possible that this correlation is simply a demonstration of the radiation efficiency of relativistic blastwaves (potentially those launched by stellar-mass BHs; Section 5.2). We discuss the likelihood of an external origin for the X-ray emission in Section 4.3.

4.3. An Internal or External Origin for the X-Ray Lightcurve?

The observed short-timescale X-ray variability by Swift (Figure 4) and NuSTAR (Figure 3) complicates the interpretation that the X-ray emission arises from an external shock. The short timescale ($\Delta T/T < 0.03$) of these flares is not possible to reproduce with an external emission mechanism. Instead, this favors an internal origin for the X-ray lightcurve out to at least $\sim$1 day (rest frame), as also seen at early times ($<10^4$ s, rest frame) in ultralong GRBs (A. J. Levan et al. 2014).

However, unlike the current sample of ultralong GRBs, the observed short-timescale variability in GRB 250702B does not overlap with the (observed) duration of its prompt gamma-ray emission, which stops being detected prior to the first XRT observation (E. Neights et al. 2025a). An additional puzzle piece is the clear agreement of the later-time (>1 day, rest frame) X-ray lightcurve with GRB afterglows (Figure 11). With these qualities in mind, the origin of the X-ray emission has two main possibilities:

1. A completely accretion-driven relativistic outflow with an internal nonthermal dissipation mechanism dominating the X-ray emission out to >65 days (observer frame), as observed in known relativistic TDEs; or
2. Late-time central engine activity to produce short-timescale variability on top of the nonthermal external shock continuum that dominates at >2 days (observer frame).

The exact cause of the X-ray emission has strong implications for the precise nature of the progenitor system and its central engine. In particular, any central engine capable of reproducing the observed X-ray emission must remain active (at least) between the initial EP detection (H. Q. Cheng et al. 2025b; D. Y. Li et al. 2025) and the end of the first NuSTAR observation. In fact, numerical simulations have shown that the soft-X-ray emission is a better tracer of the jet activity duration than the gamma-ray duration (T. Parsotan & D. Lazzati 2024). Cumulatively, the observations require an engine duration in excess of $\gtrsim$3 days in the observer frame, corresponding to $\gtrsim$1.5 days ($\gtrsim 1.6 \times 10^5$ s) in the rest frame.

The central engine is very likely due to accretion onto a BH, and the main open questions are the mass of the BH and its formation pathway (see Section 5 for further discussion). Relativistic TDEs such as Sw J1644+57 display accretion-driven central engine activity, characteristic of sharp dips and flaring, out to hundreds of days (C. J. Saxton et al. 2012; V. Mangano et al. 2016), easily exceeding this requirement. In such a scenario, the X-ray emission arises from internal dissipation within the relativistic jet, with dips in the X-ray flux likely linked to changes in the accretion rate of disrupted stellar material onto the BH. For a small enough BH mass (Section 5.1), this scenario is easily capable of matching the observed flaring timescales, but it may still be challenged to reproduce the short 1 s (observer-frame) minimum variability of the prompt emission (E. Neights et al. 2025a).

Relativistic TDEs must also emit FS X-ray emission, due to the interaction of their relativistic jet with its surrounding environment, which also gives rise to their luminous long-lived radio emission. However, the X-ray emission from the external FS is completely outshined (and therefore undetected) by the fallback accretion until late times, when the internal jet emission shuts off. If interpreting GRB 250702B as a relativistic TDE, the low X-ray luminosity of the fallback accretion, compared to known relativistic TDEs, must be explained. It is possible that this is due to lower mass accretion onto the BH or lower radiation efficiency, but this is at odds with the significantly more energetic flaring high-energy gamma-ray emission of GRB 250702B. In addition, the FS emission must be hidden at a lower flux level, which can cause challenges based on the required kinetic energy. For example, for the X-rays generated by the external shock to lie an order of magnitude below the observed lightcurve requires a small kinetic energy ($<10^{52-53}$ erg) of the jet, which leads to extremely high gamma-ray efficiencies (>90%) that we deem unrealistic (e.g., P. Beniamini et al. 2016).

In the second scenario for the X-ray emission, the external X-ray emission does not lie very far below the accretion-driven excess that produces the flaring behavior (Figure 9). Our afterglow modeling shows that this scenario is easy to produce with reasonable kinetic energies (Figure 20 in Appendix F), with the FS emission beginning to dominate the observed lightcurve at >2 days. It is important to note that the X-ray variability observed for GRB 250702B (Figure 5) is at a lower amplitude, and much less frequent, than observed in known relativistic TDEs (e.g., Sw J1644+57; D. N. Burrows et al. 2011; J. S. Bloom et al. 2011). The current sample of relativistic TDEs shows dramatic (up to 10 times) dips in the flux on short timescales, which are not observed here. There is minor evidence for a dip at the end of the initial NuSTAR observation (Figure 5) and at $\sim$2.2 days (observer frame) by Swift (Figure 1), but the variability amplitude is significantly smaller than in Sw J1644+57 (J. S. Bloom et al. 2011; D. N. Burrows et al. 2011) or AT2022cmc (I. Andreoni et al. 2022; D. R. Pasham et al. 2023). However, we point out that the jetted TDEs Sw J2058+0516 (S. B. Cenko et al. 2012) and Sw J1112-8238 (G. C. Brown et al. 2015) do not show as pronounced dips as Sw J1644+57 (J. S. Bloom et al. 2011; D. N. Burrows et al. 2011). The cause of this in GRB 250702B could be due to the proximity of the external afterglow to the flux level of the accretion-driven emission at ∼2 days (observer frame).

While past GRB afterglow observations with NuSTAR do not display this short-timescale behavior (Appendix D and Figure 17), these cover only a small sample of GRB phenomena, which are notably diverse. Ultralong GRBs (e.g., GRB 121027A) display comparable X-ray variability and dips (A. J. Levan et al. 2014) out to $\sim 10^4$ s in the rest frame (Figure 11)—see, e.g., Figure 14 of P. A. Evans et al. (2014a). This late-time X-ray variability is likely linked to ongoing central engine activity and ongoing prompt gamma-ray emission. However, the timescale required for GRB 250702B is significantly longer than the current ultralong sample and has the additional difficulty of producing the initial EP emission (D. Y. Li et al. 2025). We further discuss the prospects for the progenitor of GRB 250702B in Section 5.

4.4. Results of External Afterglow Modeling

We have modeled the multiwavelength lightcurve (Section 3.3) of GRB 250702B, assuming that the near-infrared and radio emissions are generated by a combination of the FS and RS emissions (Figure 9) and that the X-ray lightcurve after $>2 \times 10^5$ s (relative to the "E" burst; observer frame) is dominated by the external shock. Here, we outline our main results and how they impact the interpretation of GRB 250702B.

The long-lasting prompt phase adds difficulty in determining the precise onset time of the afterglow. Corroborated by our temporal analysis of the X-ray lightcurve (Section 3.1.1 and Figure 1), we performed our afterglow modeling relative to the GBM "E" burst (MJD 60858.682; Table 4). We support interpreting this as the afterglow onset time by invoking a picture where each independent GBM trigger (or prompt episode) is due to an internal shell–shell collision and essentially marks the launch time of an ultrarelativistic shell. As both shells collide, they merge to form a larger, more energetic shell, which eventually catches up to, and then refreshes, the blast wave producing the FS (P. Kumar & A. Panaitescu 2000; R. Sari & P. Mészáros 2000). This refreshed shock then resets the inferred afterglow T_0, with the most energetic shell (the "E" burst) dominating the afterglow. The results of our afterglow modeling using the "E" burst as T_0 are shown in Figure 9 and Figure 20 in Appendix F. However, we note that utilizing the "D" burst as T_0 only marginally changes our results for the afterglow parameters—see Figures 21 and 22 in Appendix F.

As we do not observe the jet's deceleration (coasting) phase, our afterglow modeling provides a lower limit to the initial Lorentz factor for the jet being required to decelerate prior to the start of the first multiwavelength observations of the afterglow phase (Figure 9). The required Lorentz factor is strongly correlated with the jet's kinetic energy (Figure 20 in Appendix F), with larger energies requiring larger Lorentz factors, as the (on-axis) deceleration time $t_{\rm dec}$ is given by (R. Sari & T. Piran 1999; E. Molinari et al. 2007)

$$\frac{t_{\rm dec}}{1+z} = \left[\frac{3-k}{2^{5-s}\pi}\frac{E_{\rm kin,iso}}{c^{5-k}\,A\,\Gamma_0^{8-2k}}\right]^{1/(3-k)}, \qquad (1)$$

where Γ_0 is the initial bulk Lorentz factor at the jet's core, $E_{\rm kin,iso}$ is the (isotropic-equivalent) kinetic energy, $A = m_{\rm p} n_0 R_0^k$, n_0 is the density normalization at the radius $R_0 = 10^{18}$ cm, $m_{\rm p}$ is the proton mass, and c is the speed of light.

The modeling finds Lorentz factors in the range of $\Gamma_0 \gtrsim 100$ (Figure 20 in Appendix F), which can be taken as lower limits to the true Lorentz factor, as higher values would allow for an earlier deceleration (i.e., consistent with observations). While we have required $\Gamma_0\theta_j \geqslant 1$ in our modeling, to prevent lateral spreading during the coast phasing such that the spherical jet approximation can be applied, we note that relaxing this requirement still demands large Lorentz factors of $\Gamma_0 > 20$–50. However, if $\Gamma_0\theta_{\rm j} < 1$, then the inferred true prompt emission fluence becomes larger by a factor of $(\Gamma_0\theta_{\rm j})^{-2}$, as most of the Γ_0^{-1} cone is actually not emitting, so the energy per solid angle is larger for the same fluence. This would increase the inferred gamma-ray energy, which is already quite large.

The derived range of Lorentz factors is consistent with inferences from the population of classical GRBs (G. Ghirlanda et al. 2018), which covers a similar range (for a wind environment). However, the range is significantly higher than expectations for relativistic TDEs (Section 5.1), which are generally thought to be less relativistic ($\Gamma_0 \approx 10$–20; e.g., B. A. Zauderer et al. 2011, 2013; I. Andreoni et al. 2022; D. R. Pasham et al. 2023) than the jets launched by GRBs. The range of Lorentz factors we infer is consistent with the detection of >1 MeV photons during the prompt phase, which require $\Gamma_0 > 50$ (E. Neights et al. 2025a).

Additionally, the steep decay of the X-ray and near-infrared data requires that the afterglow (Section 3.3) is in the post-jet-break phase prior to the start of the multiwavelength observations (Figure 9). This is consistent with the afterglow modeling presented by A. J. Levan et al. (2025b), J. Carney et al. (2025), and B. P. Gompertz et al. (2025). For a nonspreading jet (e.g., J. Granot 2007), the geometric steepening after the jet break is given by $\Delta\alpha = \frac{3-k}{4-k}$, which ranges between $\Delta\alpha = 3/4$ in a uniform-density environment ($k = 0$) to $\Delta\alpha = 1/2$ for a wind environment ($k = 2$). Our afterglow modeling favors a steep external density profile $n_{\rm ext} \propto R^{-k}$, where $k \simeq 2$. In this case, the post-jet-break slope for a nonspreading jet is given by $\alpha_{\rm j} = \frac{3}{4}(p-1) + \frac{k}{2(4-k)} + \frac{3-k}{4-k} = 1.83 \pm 0.04$ (for $\nu_{\rm m} < \nu < \nu_{\rm c}$), accounting for the errors on p and k (Figure 20 in Appendix F). This is consistent with the range of temporal slopes inferred from the X-ray lightcurve (Section 3.1.1). Including the addition of lateral jet spreading yields instead $\alpha_{\rm j} = p$ (J. E. Rhoads 1999; R. Sari et al. 1999), which would similarly prefer $p \approx 2$ and favor a slightly earlier afterglow start time closer to the "D" burst (Figure 14 in Appendix C). The overall conclusions based on the energy, density, Lorentz factor, and jet opening angle are unchanged (Figure 21 in Appendix F).

Our modeling prefers a high isotropic-equivalent blast-wave kinetic energy $E_{\rm kin,iso}$ in excess of 10^{54-55} erg, which is consistent with the large isotropic-equivalent gamma-ray energy $\sim 2 \times 10^{54}$ erg (E. Neights et al. 2025a). The true (beaming-corrected) energy release can be derived by taking into account the jet's core half-opening angle $\theta_{\rm j}$. The constraint on the jet's half-opening angle likewise scales strongly with the jet's kinetic energy, as the jet break time $t_{\rm j}$ is given by (J. E. Rhoads 1999; R. Sari et al. 1999; R. A. Chevalier & Z.-Y. Li 2000; D. A. Frail et al. 2001)

$$\frac{t_{\rm j}}{1+z} = \left[\frac{3-k}{2^{5-s}\pi}\frac{E_{\rm kin,iso}\,\theta_{\rm j}^{8-2k}}{c^{5-k}\,A}\right]^{1/(3-k)}. \qquad (2)$$

As our nonspreading jet solution requires an early jet break, the range of the jet's core half-opening angles (Figure 20 in Appendix F) can therefore be taken as an upper limit to the jet's collimation. While smaller opening angles, down to $\theta_\mathrm{j} \approx 0.01$ rad, are preferred by the fit, a rough upper limit of $\theta_\mathrm{j} \lesssim 0.02$ rad ($\lesssim 1°$) can be obtained. This is at the extremely low end of the jet opening angles observed for GRBs (e.g., D. A. Frail et al. 2001; S. B. Cenko et al. 2010; X.-G. Wang et al. 2018) and also significantly smaller than inferred for relativistic TDEs ($\theta_\mathrm{j} \approx 0.35$ rad (20°); P. Beniamini et al. 2023).

In any case, the inferred collimation constraints can be used to compute upper limits to the true collimation-corrected energy release $E_\mathrm{kin,beam} = (\theta_\mathrm{j}^2/2) E_\mathrm{kin,iso}$ for our assumed top-hat jet model. The same formalism applies to the gamma-ray energy $E_{\gamma,\mathrm{beam}}$. The true beaming-corrected energy release is then $E_\mathrm{true} = E_\mathrm{kin,beam} + E_{\gamma,\mathrm{beam}} = (4.1^{+1.6}_{-1.2}) \times 10^{50}$ erg, where we have $E_\mathrm{kin,beam} = (3.5^{+1.4}_{-1.0}) \times 10^{50}$ erg and $E_{\gamma,\mathrm{beam}} = (5.8^{+8.8}_{-5.6}) \times 10^{49}$ erg. These values are consistent with the range of energies inferred for traditional GRBs (e.g., S. B. Cenko et al. 2010). We emphasize that due to the lack of a direct jet break measurement, these should be treated as upper bounds on the energy release. However, it must be noted that the association of these values with upper bounds on the energy requires that we are observing a post-jet-break lightcurve. While our afterglow modeling favors this interpretation, if instead there has been no jet break out to 65 days (observer frame), as seen in a handful of GRBs (e.g., B. O'Connor et al. 2023), this would instead imply a much wider jet (>10°) and significantly larger collimation-corrected energies ($>10^{53}$ erg) that are difficult to reconcile with a traditional collapsar progenitor channel (see also J. Carney et al. 2025).

We can likewise use the inferred kinetic energy and gamma-ray energy release to compute the gamma-ray efficiency $\eta_\gamma = E_{\gamma,\mathrm{iso}}/(E_{\gamma,\mathrm{iso}} + E_\mathrm{kin,iso})$, where we have used the isotropic-equivalent definition for energies (though this does not change the result). We derive a gamma-ray efficiency of $\eta_\gamma = 0.15^{+0.15}_{-0.08}$, which is consistent with values inferred for classical GRBs (L. Nava et al. 2014; P. Beniamini et al. 2015).

4.5. Implications from the Gas-to-dust Ratio

The relation between the hydrogen column density N_H and visual extinction A_V follows a well-known linear relationship in the Milky Way, e.g., $N_\mathrm{H}/A_\mathrm{V} = (2.21 \pm 0.09) \times 10^{21}$ cm^{-2} mag^{-1} (e.g., P. Predehl & J. H. M. M. Schmitt 1995; T. Güver & F. Özel 2009). The exact slope of this relation can vary between galaxies and between different assumptions for the dust extinction law. Assuming the relation within our own Galaxy, we would obtain $A_\mathrm{V} \approx 13.6 \pm 2.8$ mag, which is higher than the inferred values (Section 3.2.2).

Based on our modeling of the X-ray-to-near-infrared SED (Figure 8), we find a gas-to-dust ratio of $N_\mathrm{H,z}/A_\mathrm{V,z} = (4.5 \pm 1.0) \times 10^{21}$ cm^{-2} mag^{-1} for GRB 250702B. This is approximately twice the ratio for the Milky Way (T. Güver & F. Özel 2009). The inferred intrinsic dust extinction $A_\mathrm{V,z}$ is strongly dependent on the assumed spectral shape between the X-ray and near-infrared bands (Section 3.2.2) and the assumption they arise from the same emission mechanism (see Section 3.3). If, instead, the X-ray emission is dominated by an accretion-driven outflow (Section 4.3) and is unrelated to the near-infrared emission, under the assumption that the near-infrared emission arises from the external afterglow, we still require a significant dust contribution ($A_\mathrm{V,z} \gtrsim 3$) in our modeling.

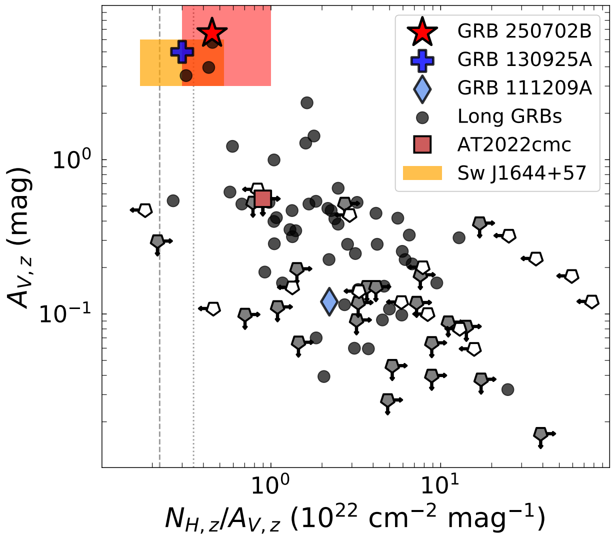

Figure 12. Intrinsic ratio of hydrogen column density to visual extinction versus visual extinction inferred from long-GRB (black circles) afterglows (P. Schady et al. 2010; J. Greiner et al. 2011; T. Krühler et al. 2011b; D. A. Perley et al. 2011; T. Zafar et al. 2011). Sources with either upper limits on the column density (white) or upper limits on the extinction (gray) are shown as pentagons. GRB 250702B is shown as a red star, based on our near-infrared-to-X-ray modeling. A more conservative range of the allowed values (even breaking the assumption that both X-ray and near-infrared data originate from the external shock) is shown as a shaded red region. The ultralong GRBs 111209A (G. Stratta et al. 2013) and GRB 130925A (J. Greiner et al. 2014) are also shown. We display as a shaded region the range for the relativistic TDE Sw J1644 (J. S. Bloom et al. 2011; D. N. Burrows et al. 2011; A. J. Levan et al. 2011, 2016) and as a triangle that for AT2022cmc (based on an upper limit on reddening; see Y. Yao et al. 2024). The dashed and dotted lines refer to the median values for the Milky Way (T. Güver & F. Özel 2009) and SMC (P. Bouchet et al. 1985), respectively. This figure is reproduced from T. Krühler et al. (2011b).

The allowed range of values is displayed by the shaded red region in Figure 12. We compare this to the values observed for classical long GRBs, ultralong GRBs, and relativistic TDEs in Figure 12. It is worth noting the ratio is comparable to those found in the relativistic TDE Sw J1644+57 ($N_\mathrm{H,z}/A_\mathrm{V,z} \approx (2\text{–}5) \times 10^{21}$ cm^{-2} mag^{-1}; J. S. Bloom et al. 2011; D. N. Burrows et al. 2011; A. J. Levan et al. 2011) and in the ultralong GRB 130925A ($N_\mathrm{H,z}/A_\mathrm{V,z} \approx 3 \times 10^{21}$ cm^{-2} mag^{-1}; P. A. Evans et al. 2014b; J. Greiner et al. 2014).

The allowed range of $N_\mathrm{H,z}/A_\mathrm{V,z}$ ratios for GRB 250702B lies at the low end of the values inferred by P. Schady et al. (2010), who had instead found (for a sample of 28 classical long GRBs) that the GRB-derived $N_\mathrm{H,z}/A_\mathrm{V,z}$ ratio of $(3.3 \pm 2.8) \times 10^{22}$ cm^{-2} mag^{-1} exceeded the values for the SMC, LMC, and Milky Way by at least a factor of 10 (see their Figure 5). T. Krühler et al. (2011a) analyzed a sample of the dustiest GRB afterglows ($A_\mathrm{V,z} \approx 3\text{–}5$ mag) and identified a possible inverse relationship between the intrinsic visual extinction $A_\mathrm{V,z}$ and the intrinsic gas-to-dust ratio $N_\mathrm{H,z}/A_\mathrm{V,z}$ (see Figure 12). They found that the dustiest afterglows ($A_\mathrm{V,z} > 3$ mag) had smaller values of $N_\mathrm{H,z}/A_\mathrm{V,z}$ compared to the bulk sample. GRB 250702B agrees with this trend and lies in the same location as the dustiest afterglows (see Figure 12; T. Krühler et al. 2011a). However, lower gas-to-dust ratios (order 10^{20} cm^{-2} mag^{-1}) have been found for a handful of other "dark" bursts (A. J. van der Horst et al. 2009; J. Greiner et al. 2011), such as GRBs 051022 (A. J. Castro-Tirado et al. 2007) and 150309A (A. J. Castro-Tirado et al. 2024)—see also D. A. Perley et al. (2009).

T. Krühler et al. (2011a) interpret the lower $N_{\mathrm{H},z}/A_{\mathrm{V},z}$ ratio as two independent absorbers with local ionized metals in the circumburst environment producing the inferred X-ray absorption $N_{\mathrm{H},z}$ and a physically separate dusty absorber in the host galaxy producing the high visual extinction $A_{\mathrm{V},z}$. This scenario is plausible for GRB 250702B and is consistent with the independent inference of a dusty galaxy based on the host SED modeling of J. Carney et al. (2025). However, we cannot rule out that the local environment of GRB 250702B simply differs from classical GRBs and has SMC-like gas-to-dust properties (P. Bouchet et al. 1985). We do caution that $N_{\mathrm{H},z}/A_{\mathrm{V},z}$ ratios (e.g., T. Güver & F. Özel 2009) are calibrated in regions where $A_{\mathrm{V}} < 1$ mag, and they may not apply in denser or dustier environments as observed for GRB 250702B. Regardless of the interpretation, we can conclude that all events with high $A_{\mathrm{V},z}$ fall in the same region of the parameter space, which is worth further investigation. We note that there are existing selection effects against the discovery of the most highly extinguished GRBs and that rapid, deep near-infrared imaging is required to identify other potential members of this class, which will aid in understanding the origin of these small gas-to-dust ratios.

5. Interpretation of GRB 250702B

The possible scenarios for explaining GRB 250702B can be most simply broken down into two progenitor categories, those involving either: (i) a massive BH; or (ii) a stellar-mass BH central engine. The expected behaviors, such as the minimum variability timescale or duration, are quite different between these different progenitor systems. Below, we discuss these differences in more detail and highlight where each progenitor system has difficulties in reproducing the observed behavior.

5.1. An IMBH Progenitor

Our understanding of the relativistic jets launched by TDEs is limited due to the small number of existing candidates (J. S. Bloom et al. 2011; D. N. Burrows et al. 2011; A. J. Levan et al. 2011; B. A. Zauderer et al. 2011; S. B. Cenko et al. 2012; G. C. Brown et al. 2015; D. R. Pasham et al. 2015, 2023; I. Andreoni et al. 2022; Y. Yao et al. 2024; B. O'Connor et al. 2025b). These sources are thought to be produced when a main-sequence (MS) star is shredded by a massive BH ($M_{\mathrm{BH}} \approx 10^{5-8} M_{\odot}$), launching a narrowly collimated relativistic jet along our sightline.[34] They have been found to emit extremely luminous long-lived X-ray and radio emission. Their X-ray emission is highly variable, with rapid short-term (∼hours) variability.

Relativistic TDEs are found at the centers of their host galaxies,[35] coincident with the locations of massive BHs ($\gtrsim 10^{5} M_{\odot}$). These locations are possibly very dusty, as seen in Sw J1644+57 (A. J. Levan et al. 2011, 2016). This is consistent with the large dust column present in GRB 250702B. However, GRB 250702B is clearly offset by $\sim 0\farcs7$ from the center of its host galaxy (J. Carney et al. 2025; A. J. Levan et al. 2025b), corresponding to ∼ 5.8 kpc at $z = 1$ (B. P. Gompertz et al. 2025). The offset may be consistent with an IMBH scenario and is not unprecedented in TDEs (those without indications of relativistic outflows; C. C. Jin et al. 2025; Y. Yao et al. 2025). However, the environment of an offset IMBH is expected to be significantly less dense, and likely less dusty, when compared to the environment surrounding an SMBH. In particular, a wind-like environment ($n_{\mathrm{ext}} \propto R^{-2}$), as favored by our afterglow modeling (Section 3.3), is not expected around a massive BH. We suggest this favors instead a stellar-mass BH progenitor, as discussed further in Section 5.2. However, this is not far off from a Bondi-like profile (i.e., $r^{-3/2}$; see J. Granot et al. 2025, in preparation for further discussion), which could be expected for the nucleus of a (dwarf) galaxy undergoing a gas-rich merger (as possibly favored by the host galaxy morphology; J. Carney et al. 2025).

Associating the observed prompt emission duration (Section 4.1) with accretion onto the BH following the tidal disruption of a star, the peak must have occurred on a timescale of at least ∼1 day (observer frame), allowing for the initial detection by the EP ∼24 hr before the Fermi triggers (Table 4). If the disrupted star was on the MS and completely destroyed, the time to peak emission (from initial pericenter) is $t_{\mathrm{peak}} \approx 25 M_{\bullet,6}^{1/2}$ days (E. R. Coughlin & C. J. Nixon 2022; A. Bandopadhyay et al. 2024; J. Fancher et al. 2025), where $M_{\bullet,6}$ is the mass of the disrupting BH in units of $10^{6} M_{\odot}$. After the peak time of the fallback accretion rate (also referred to as the fallback time), the X-ray lightcurve will decay (e.g., $t^{-5/3}$), as observed in past relativistic TDEs (Figure 11). Here, we observe the source to be fading from the initial XRT observation (∼0.5 days after the initial triggers). Therefore, we consider a conservative bound on the peak time of fallback accretion to be $t_{\mathrm{peak}} \lesssim \left(\frac{1}{1+z}\right) 1.5$ days. Equating this peak timescale to $\lesssim \left(\frac{1}{1+z}\right) 1.5$ days then constrains the mass of the disrupting BH to $\lesssim 9 \times 10^{2} M_{\odot}$, which is firmly in the IMBH regime and could, e.g., be present in a low-mass satellite of the visually distorted massive parent galaxy (see J. Carney et al. 2025; A. J. Levan et al. 2025b). Allowing for an earlier disruption of the star (though disfavored by the existing data) up to a day before even the initial detections (H. Q. Cheng et al. 2025b; D. Y. Li et al. 2025; E. Neights et al. 2025a) would extend this requirement on the BH mass to $\lesssim 2.5 \times 10^{3} M_{\odot}$. The required BH masses are consistent with the requirement ($\lesssim 5 \times 10^{4} M_{\odot}$) from the Schwarzschild light-crossing time (Section 4.1). The partial disruption of the star would only lengthen this timescale, and while placing it on a tightly bound orbit could reduce the time to peak for a higher-mass BH, it would require an additional mechanism, e.g., Hills capture (J. G. Hills 1988) or disruption by a BH binary, to generate such an orbit.

An alternative scenario is that the disrupted star was a white dwarf (WD), in which case the time to peak could have been significantly shorter (for the same BH mass) as compared to the disruption of an MS star. Figure 13 (left) shows the prediction for the peak timescale, t_{peak}, as a function of WD mass, $M_{\star}$, that arises from equating the maximum gravitational field in the WD interior to the tidal field of the BH (i.e., by employing the model described in E. R. Coughlin &

---

[34] The inference of a highly collimated jet is required by the extremely super-Eddington accretion rates. A collimated jet drastically decreases the required energy budget compared to the inferred isotropic-equivalent energy.

[35] AT2022cmc is an exception, as no host galaxy has been detected to date (I. Andreoni et al. 2022).

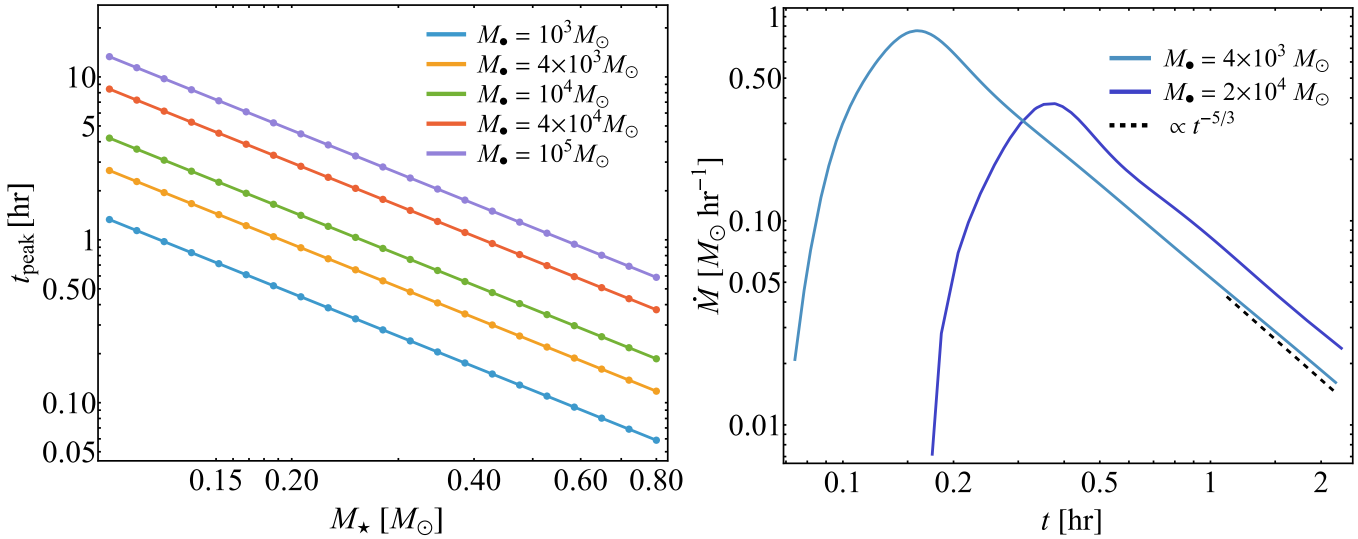

Figure 13. Left: the peak timescale (source frame) for accretion onto a BH from a tidally disrupted WD, as a function of the mass of the WD. The different colors represent different BH masses, as shown in the legend. Right: fallback rate onto the BH from a hydrodynamical simulation of a $0.6M_\odot$ WD modeled as a 5/3 polytrope, being disrupted by a $4 \times 10^3 M_\odot$ (light blue curve) and $2 \times 10^4 M_\odot$ (dark blue curve) BH. The black dashed line shows a $t^{-5/3}$ scaling, which is the expected late-time scaling of the fallback rate if the WD is completely tidally destroyed. The times are in the source frame.

C. J. Nixon 2022), assuming that the WD has a 5/3 polytropic density profile and adopting the polytropic relationship $R_\star = 0.011(M_\star/(0.6M_\odot))^{-1/3}R_\odot$ (M. Nauenberg 1972). We see that the peak timescale follows a power-law scaling with the mass of the WD ($t_{\rm peak} \propto M_\star^{-3/2}$) and, for disruptions caused by a $4 \times 10^3\, M_\odot$ BH, ranges from ∼0.1 to 2.7 hr (source frame) for WD masses ranging from 0.1 to $0.8M_\odot$. Higher-mass BHs yield longer peak timescales, up to ∼10 hr for a low-mass WD being disrupted by a $10^5 M_\odot$ BH. These timescales are far too short to reproduce the long-lasting high-energy emission observed from GRB 250702B, especially as larger BHs also become strongly disfavored by the short minimum variability timescale (see E. Neights et al. 2025a).

The times to peak fallback shown in Figure 13 (left), as well as the scaling with the WD mass, are in good agreement with the return time of the most bound debris that comes from the standard "frozen-in" model (as originally proposed in J. H. Lacy et al. 1982; see also M. J. Rees 1988; G. Lodato et al. 2009; N. Stone et al. 2013). Specifically, this approximation predicts (using the previously referenced mass–radius relationship)

$$T_{\rm fb} = \frac{\pi R_\star^{3/2}}{\sqrt{2GM_\star}}\left(\frac{M_\bullet}{M_\star}\right)^{1/2} \simeq 0.12\left(\frac{M_\bullet}{4 \times 10^3 M_\odot}\right)^{1/2}\left(\frac{M_\star}{0.6M_\odot}\right)^{-3/2}\ {\rm hr}. \qquad (3)$$

These dependencies on BH mass and stellar mass are both present in Figure 13 (left).

To further substantiate this ∼hour-long timescale, we performed hydrodynamical simulations of the disruption of a $0.6M_\odot$ WD modeled as a $\gamma = 5/3$ polytrope by a $4 \times 10^3 M_\odot$ BH and a $2 \times 10^4 M_\odot$ BH, using the smoothed particle hydrodynamics code PHANTOM (D. J. Price et al. 2018). The radial density profile was mapped onto a 3D particle distribution in PHANTOM and relaxed for ∼10 sound-crossing times across the stellar radius. We used 10^5 particles to model the WD and an adiabatic equation of state with an adiabatic index $\Gamma = 5/3$. Its center of mass was placed on a parabolic orbit with a pericenter distance $r_{\rm p} = r_{\rm t}$ (where $r_{\rm t} = R_\star(M_\bullet/M_\star)^{1/3}$ is its tidal radius), at an initial distance of $5r_{\rm t}$ from the BH. Figure 13 (right) shows the mass fallback rate onto the BH. For the $4 \times 10^3 M_\odot$ ($2 \times 10^4 M_\odot$) BH, the fallback rate peaks at a time of ∼0.16 hr (0.38 hr), which is roughly consistent with the expectations of the standard "frozen-in" model (Equation (3)) and agrees very well with the predictions from E. R. Coughlin & C. J. Nixon (2022; shown in the right panel of Figure 13).

We note that the hydrodynamic simulation shown in Figure 13 (right) provides the fallback rate, which is not necessarily equal to the accretion rate, which is ultimately responsible for liberating the observed energy (by assumption here). In particular, there will be a substantial difference between the two if the viscous timescale is substantially longer than the timescale over which the material is supplied to the BH, i.e., the fallback time (M. J. Rees 1988). For standard α-disk models and typical values of α, the viscous time is generally short compared to the fallback time, and the timescale over which the viscous delay becomes significant is ∼years (J. K. Cannizzo et al. 1990; G. Lodato & E. M. Rossi 2011). Additionally, recent works (e.g., B. Mockler et al. 2019; M. Nicholl et al. 2022) have found that the early-time luminosities of observed TDEs can be reproduced well with fallback models that impose zero viscous delay (though late-time observations of TDEs exhibit sustained levels of accretion that are consistent with a viscously spreading disk; S. van Velzen et al. 2019).

Based on Figure 13, we see that a WD disruption would produce a timescale too short to be consistent with the observed day-long duration associated with the prompt emission. Specifically, noting that the fallback rate peaks on a timescale of ∼0.16 hr for a $4 \times 10^3 M_\odot$ BH and using the $\propto M_\bullet^{1/2}$ scaling implied by Equation (3) (and shown in the right panel of Figure 13), a BH mass of $M_\bullet \simeq 4 \times 10^7 M_\odot$ would be required to yield a peak timescale of $\sim\left(\frac{1}{1+z}\right)1.5$ days. This is well in excess of the Hills mass for the disruption of a WD, which is comparable to ∼*a few* × $10^5 M_\odot$ if the BH is spinning and the orbital angular momentum of the star is aligned with the spin axis of the BH. While the fallback rates shown in Figure 13 (right) are obtained from the complete disruption of a WD, a partial disruption could yield a longer peak timescale by a factor of at most a few.[36] A longer peak timescale could also arise from the WD being on an unbound (eccentricity > 1) orbit about the BH, but, as shown in Figure 4 of M. Cufari et al. (2022), $t_{\rm peak}$ changes by less than a factor of $\sim$10 over a wide range of orbital eccentricities, implying that the BH mass required to generate a fallback rate having a peak timescale of at least a day would still exceed the Hills mass for the disruption of a WD. A WD does not produce a long-lasting-enough central engine as required by the prompt phase, unless a tightly bound orbit (in which essentially all debris is accreted on the orbital timescale) combined with (rare) repeated partial disruptions is considered (A. J. Levan et al. 2025b). Such scenarios likely require a (likely rare) Hills capture mechanism (J. G. Hills 1988). Based on these arguments, we strongly disfavor the disruption of a WD by an IMBH as the progenitor of GRB 250702B.

We therefore return to the consideration of an MS star disrupted by an IMBH. A characteristic feature of the known relativistic TDEs is a sharp cessation of their jet activity and a corresponding significant drop in luminosity, which can be interpreted as the transition from super-Eddington accretion to sub-Eddington accretion onto the BH (e.g., B. A. Zauderer et al. 2013; D. R. Pasham et al. 2015; T. Eftekhari et al. 2024). The observation of a steep drop in X-ray luminosity would be a smoking gun for a TDE progenitor, as it is not possible in an external shock scenario. Thus, long-term X-ray monitoring is required to search for this possibility. The shutoff time can be related to the mass of the BH. Using the late-time Chandra observations, we can confirm that the jet has not shut off prior to 65 days (observer frame). Given the time to peak in the fallback rate $t_{\rm peak}$ and the peak of the fallback rate itself as $\dot{M}_{\rm peak}$, one can estimate the subsequent and time-dependent accretion luminosity as $L = \eta c^2 \dot{M}_{\rm peak}(t/t_{\rm peak})^{-5/3}$, from which the time to reach the Eddington limit, $t_{\rm Edd}$, is

$$t_{\rm Edd} = t_{\rm peak}\left(\frac{\eta\kappa\dot{M}_{\rm peak}\,c}{4\pi G M_\bullet}\right)^{3/5}. \tag{4}$$

Further letting $\dot{M}_{\rm peak} \simeq M_\star/(4t_{\rm peak})$ and $t_{\rm peak} \simeq 25 M_{\bullet,6}^{1/2}$ days, this becomes (after setting $\eta = 0.1$ and $\kappa = 0.34$ cm^2 g^{-1})

$$t_{\rm Edd} \simeq 500 M_{\bullet,6}^{-2/5} M_{\star,\odot}^{3/5}\ \text{days}, \tag{5}$$

where $M_{\star,\odot}$ is the mass of the star in solar masses. For a BH mass of $\sim 10^3 M_\odot$, which is required for a peak timescale of $\lesssim\left(\frac{1}{1+z}\right)1.5$ days, this would predict a (source-frame) time to reach the Eddington limit of $t_{\rm Edd} \simeq 20$ yr—i.e., well in excess of the observed 65 day lower limit (Figures 1 and 11). On the other hand, the disruption of a lower-mass star (which is more likely if disrupted stars are drawn from a standard stellar population), a partial TDE, and a lower radiative efficiency—which is likely, given the very high Eddington fraction and corresponding optical depths—would all serve to reduce this timescale. It is worth noting that the time to Eddington-level accretion for a WD–IMBH merger is likewise long (as the initial peak accretion rate is so highly super-Eddington), with typical (source-frame) timescales of $\sim$1 yr for the fiducial parameters considered above. Late-time X-ray observations are strongly encouraged to constrain or measure this timescale, as this can be seen as "smoking gun" evidence for a TDE scenario.

We note that a possible issue with the scenario in which an MS star is disrupted by a lower-mass BH is that the relativistic advance of the periapsis angle is $3\pi G M_\bullet/(c^2 r_{\rm p})$ to lowest order in $1/r_{\rm p}$, which amounts to $\sim 0\overset{\circ}{.}3$ for a solar-type star and $r_{\rm p} = r_{\rm t}$. Such a small periapsis advance could lead to the inefficient circularization of the debris, but this could be alleviated if the pericenter distance of the star is well within the tidal radius. In the Newtonian approximation and when the disrupted star is in the pinhole scattering regime (necessary for high-β disruptions), the cumulative distribution function for β is $F_\beta(\beta) = 1/\beta$, such that $\sim$2.5% of stars reach $\beta \geqslant 40$ and have periapsis advance angles $\gtrsim 10°$. This would therefore be a relatively rare event, but given that no other such GRBs have yet been observed, we do not consider this an inconsistency.

Thus, while we can strongly disfavor a WD–IMBH merger, we cannot exclude an MS–IMBH merger (for further discussion, see J. Granot et al. 2025, in preparation). The MS–IMBH merger is consistent with many of the observed timescales, but still has difficulties as: (i) the multiple gamma-ray triggers are unlike any observed in past relativistic TDEs; (ii) the X-ray lightcurve is consistent with the luminosities of known GRBs and not known relativistic TDEs (Figures 9 and 11); and (iii) the event follows standard GRB prompt afterglow correlations (Figure 10). Additionally, the observed rate of GRBs, even ultralong GRBs (though this depends on the exact duration requirement for this definition; see A. J. Levan et al. 2014), exceeds the known number of relativistic TDEs.

5.2. *A Stellar-mass BH Progenitor*

The observed properties of GRB 250702B are most similar to those found in the (notably small) sample of ultralong GRBs. The main characteristics that make this event appear an outlier are the discovery of untriggered high-energy emission up to a day prior to the first onboard gamma-ray triggers (H. Q. Cheng et al. 2025b; D. Y. Li et al. 2025; E. Neights et al. 2025a) and the continued short-timescale flaring out to 2 days (Section 4.3). Besides these factors, all other properties appear typical of GRBs. These include the X-ray luminosity and rapid lightcurve decay, the triggered gamma-ray emission, the isotropic-equivalent gamma-ray energy release, the gamma-ray efficiency, the prompt emission's minimum variability timescale, the consistency of the multiwavelength lightcurve with external afterglow emission in a dense wind environment, the dusty host galaxy, and the offset location within its host. In fact, each of these properties are instead atypical for a massive BH progenitor (Section 5.1).

However, the discovery of the early soft-X-ray emission (D. Y. Li et al. 2025) and the extremely long ($>$25 ks; E. Neights et al. 2025a) gamma-ray emission are difficult to reconcile in a traditional collapsar scenario, even considering a peculiar progenitor, such as the collapse of a blue supergiant (P. Mészáros & M. J. Rees 2001; D. Nakauchi et al. 2013; G. Stratta et al. 2013; K. Ioka et al. 2016). It is worth noting that the EP is revealing that soft-X-ray emission can extend for

---

[36] Figure 2 of D. Garain & T. Sarkar (2024) shows fallback rates for the disruption of a $1M_\odot$ WD by a $10^3 M_\odot$ BH for a range of orbital pericenter distances, wherein the peak timescale shows very little variation over the entire range.

10–100 times the gamma-ray emission for what otherwise would appear a typical GRB at gamma-ray frequencies (see, e.g., Y.-H. I. Yin et al. 2024, 2025; A. J. Levan et al. 2025a; Y. Liu et al. 2025). If this same phenomenon can be extended to ultralong GRBs, it could potentially explain the longer duration of the prompt emission. Previously existing selection biases, based on the lack of widefield soft-X-ray telescopes, may have played a role in limiting the discovery of soft precursor emission. It is possible that the initial soft-X-ray emission detected by the EP (H. Q. Cheng et al. 2025b; D. Y. Li et al. 2025) is due to the formation of a cocoon (as in, e.g., J. K. Leung et al. 2025), as the jet (or multiple shells launched by the central engine) attempts to break out of the extended stellar radius of a blue supergiant. As subsequent shells launched within the jet do not have as great a difficulty burrowing out of the stellar material, we have a clearer picture of their prompt gamma rays (likely produced through internal shocks). However, the requirements for the duration of the central engine are still extreme even in such a scenario and lead us to conclude that a collapsar (even from a blue supergiant) is an unlikely progenitor for GRB 250702B.

Based on all of the considerations presented in this manuscript, we find that while GRB 250702B displays similar properties to both classical and ultralong GRBs (e.g., Figure 10), with the main exception being the early pre-trigger X-ray emission (D. Y. Li et al. 2025), it may be explained by a "hybrid" progenitor system, involving a stellar-mass BH but with a TDE-like central engine. This is also favored by the consistency of the surrounding environment with the profile of a stellar wind. The main possibilities for this hybrid system are the merger of a helium star with a stellar-mass BH (C. L. Fryer & S. E. Woosley 1998; S. E. Woosley & A. Heger 2012; E. Neights et al. 2025a) or a micro-TDE with a stellar-mass BH (H. B. Perets et al. 2016; P. Beniamini et al. 2025). These scenarios have been shown to be compatible with day-long central engine activity, as required by this event, and may more naturally explain the early X-ray emission, 1 s minimum variability timescale of the prompt emission, long-lived central engine ($\gtrsim$3 days), and short-timescale X-ray flaring produced by an accretion-driven relativistic outflow. These progenitor scenarios can also potentially explain the current sample of ultralong GRBs. A complete discussion of the micro-TDE scenario is provided by P. Beniamini et al. (2025) and of the helium merger scenario by E. Neights et al. (2025a).

6. Conclusions

We present a comprehensive X-ray analysis of the ultralong transient GRB 250702B using Swift, NuSTAR, and Chandra. These observations trace the X-ray counterpart between 0.5 to 65 days from discovery and reveal a rapidly fading source at 0.3–79 keV. By modeling the near-infrared-to-X-ray SED, we uncover a potential spectral break that is likely due to the synchrotron cooling frequency. The multiwavelength light-curve is found to be well described by the standard fireball model (FS and RS emission) in a wind-like environment. Superposed on this external shock continuum, Swift and NuSTAR detect short-timescale X-ray flares with $\Delta T/T < 0.03$, implying engine-dominated X-ray emission persisting to at least $\sim$2 days that is most naturally attributable to accretion-powered variability.

We demonstrate that the overall characteristics of GRB 250702B do not cleanly match either known relativistic TDEs or ultralong GRBs. With the exception of the initial soft-X-ray detection a full day before the initial gamma-ray triggers, the properties have a closer match to those seen by ultralong GRBs but require an even-longer-lived central engine ($\gtrsim$3 days). In particular, the early soft-X-ray detections (H. Q. Cheng et al. 2025b; D. Y. Li et al. 2025) are not easily explained in the standard collapsar model (S. E. Woosley 1993). As such, we favor a hybrid stellar-mass BH progenitor, such as a micro-TDE (P. Beniamini et al. 2025)—although see also E. Neights et al. (2025a) and J. Granot et al. 2025, in preparation) for alternative explanations. Additional observations of similar transients, hopefully discoverable via the EP (W. Yuan et al. 2025), will aid in uncovering the true nature of GRB 250702B.

Acknowledgments

The authors thank the anonymous referee for the helpful comments that improved the clarity of the manuscript. The authors acknowledge Karl Forster and the NuSTAR SOC for their rapid scheduling of our observations, as well as Pat Slane and the CXO staff for approval and scheduling of our Chandra DDT request. B.O. acknowledges Brian Grefenstette, Oli Roberts, Eliza Neights, and Eric Burns for useful discussions. B.O. thanks Ben Gompertz, Andrew Levan, and Antonio Martin-Carrillo for sharing the redshift derived by JWST.

B.O. is supported by the McWilliams Postdoctoral Fellowship in the McWilliams Center for Cosmology and Astrophysics at Carnegie Mellon University. J.D. acknowledges support from NASA under award numbers NAS5-0136, 80NSSC25K7567, and 80NSSC25K7788. D.R.P. acknowledges support from NASA in the form of a NuSTAR guest observer program. E.R.C. acknowledges support from NASA through the Astrophysics Theory Program, grant 80NSSC24K0897. A.B. acknowledges support from NASA through the FINESST program, grant 80NSSC24K1548. M.M. is supported by an appointment to the NASA Postdoctoral Program at the NASA Goddard Space Flight Center, administered by Oak Ridge Associated Universities under contract with NASA. J.H. acknowledges support from NASA under award number 80GSFC21M0002. The work of P.B. was funded by a grant (no. 2020747) from the United States–Israel Binational Science Foundation (BSF), Jerusalem, Israel and by a grant (no. 1649/23) from the Israel Science Foundation. M. B. is supported by a Student Grant from the Wübben Stiftung Wissenschaft. Funded in part by the Deutsche Forschungsgemeinschaft (DFG, German Research Foundation) under Germany's Excellence Strategy—EXC-2094-390783311.

This work used resources on the Vera Cluster at the Pittsburgh Supercomputing Center (PSC). Vera is a dedicated cluster for the McWilliams Center for Cosmology and Astrophysics at Carnegie Mellon University. We thank the PSC staff for their support of the Vera Cluster.

This work has made use of data from the NuSTAR mission—a project led by the California Institute of Technology, managed by the Jet Propulsion Laboratory, and funded by the National Aeronautics and Space Administration. This research has made use of the NuSTAR Data Analysis Software (`NuSTARDAS`) jointly developed by the ASI Space Science Data Center (SSDC, Italy) and the California Institute of Technology (Caltech, USA). The scientific results reported in this article are based on observations made by the Chandra X-ray Observatory. This research has made use of software provided by the Chandra X-ray Center (CXC) in the application package CIAO. This work has made use of data supplied by the UK Swift Science Data Centre at the University of Leicester. This research has made use of the XRT Data Analysis Software (XRTDAS) developed under the responsibility of the ASI Science Data Center (ASDC), Italy. This research has made use of data and/or software provided by the High Energy Astrophysics Science Archive Research Center (HEASARC), which is a service of the Astrophysics Science Division at NASA/GSFC.

Facilities: Swift, NuSTAR, CXO.

Software: `Astropy` (Astropy Collaboration et al. 2018, 2022), `SciPy` (P. Virtanen et al. 2020), `emcee` (D. Foreman-Mackey et al. 2013), `corner` (D. Foreman-Mackey 2016), `stingray` (D. Huppenkothen et al. 2019), `XSPEC` (K. A. Arnaud 1996), `GUANO` (A. Tohuvavohu et al. 2020), `NITRATES` (J. DeLaunay & A. Tohuvavohu 2022), `BatAnalysis` (T. Parsotan et al. 2023), `CIAO` (A. Fruscione et al. 2006), `HEASoft` (Nasa High Energy Astrophysics Science Archive Research Center (Heasarc) 2014).

Appendix A
Log of Observations

We present the log of X-ray observations of EP250702a analyzed in this work in Table 1. The flux values derived from the Swift/BAT Survey mode data are presented in Table 2. In Table 3, we present the prompt detections of GRB 250702D, GRB 250702D, and GRB 250702E (Table 4) by Swift/BAT using the `GUANO` software (Section 2.1.1).

Table 1

Log of X-Ray Observations of EP250702a Obtained with NuSTAR (PI: Pasham) and Chandra (PI: O'Connor, ObsID: 31011; and PI: Eyles-Ferris, ObsID: 31468)

Start Time (UT)	δT (days)	Telescope	Instrument	Exposure (ks)	ObsID	Flux (erg cm^{-2} s^{-1})
			NuSTAR			
2025-07-03 20:46:11	1.32	NuSTAR	FPMA/B	21.7	81102349002	$(2.42 \pm 0.07) \times 10^{-11}$
2025-07-07 22:56:12	5.41	NuSTAR	FPMA/B	24.2	81102349004	$(1.33 \pm 0.31) \times 10^{-12}$
2025-07-12 01:41:05	9.52	NuSTAR	FPMA/B	38.8	91101324002	$(3.7 \pm 1.9) \times 10^{-13}$
			Chandra			
2025-08-09 05:49:28	37.69	Chandra	ACIS-S	27.7	31011	$(3.3^{+0.7}_{-0.6}) \times 10^{-14}$
2025-09-05 23:26:41	65.52	Chandra	ACIS-S	39.6	31468	$(1.15^{+0.40}_{-0.30}) \times 10^{-14}$

Note. The fluxes are reported in 3–79 keV for NuSTAR and 0.3–10 keV for Chandra. The days from discovery, using the trigger time of GRB 250702D, are provided in the δT column.

Table 2
Log of Swift/BAT Observations of GRB 250702B between $\delta T \pm 4$ days from GRB 250702D

MJD	δT (days)	Exposure (s)	Flux (erg cm^{-2} s^{-1})
60855.1187	−3.43	489	$<2.02 \times 10^{-8}$
60856.1582	−2.39	494	$<3.92 \times 10^{-8}$
60856.2917	−2.26	778	$<2.11 \times 10^{-8}$
60856.4177	−2.13	996	$<2.19 \times 10^{-8}$
60856.3377	−2.21	764	$<6.27 \times 10^{-9}$
60856.4813	−2.07	116	$<1.84 \times 10^{-8}$
60857.0053	−1.54	981	$<6.78 \times 10^{-9}$
60857.1878	−1.36	334	$<1.27 \times 10^{-8}$
60857.2032	−1.34	508	$<8.85 \times 10^{-9}$
60857.2654	−1.28	891	$<6.97 \times 10^{-9}$
60857.3869	−1.16	1618	$<5.43 \times 10^{-9}$
60857.5171	−1.03	1585	$<5.42 \times 10^{-9}$
60857.5854	−0.96	126	$<5.77 \times 10^{-8}$
60857.5886	−0.96	450	$<9.48 \times 10^{-9}$
60857.6599	−0.89	468	$<1.32 \times 10^{-8}$
60857.7022	−0.85	350	$<1.28 \times 10^{-8}$
60857.7198	−0.83	694	$<7.61 \times 10^{-9}$
60857.7710	−0.78	891	$<5.43 \times 10^{-9}$
60857.7821	−0.77	531	$<1.03 \times 10^{-8}$
60857.9162	−0.63	883	$<1.06 \times 10^{-8}$
60858.2306	−0.32	361	$<4.22 \times 10^{-8}$
60858.3658	−0.18	202	$<4.59 \times 10^{-8}$
60858.3689	−0.18	409	$<7.39 \times 10^{-9}$
60858.6245	0.08	1065	$<1.65 \times 10^{-8}$
60858.6816	0.13	856	$(4.95 \pm 1.14) \times 10^{-9}$
60858.7446	0.20	877	$<3.50 \times 10^{-9}$
60858.7557	0.21	411	$<1.20 \times 10^{-8}$
60858.8170	0.27	1058	$(1.08 \pm 0.39) \times 10^{-8}$
60859.0137	0.47	681	$<1.01 \times 10^{-8}$
60859.0851	0.54	702	$<4.15 \times 10^{-9}$
60859.1309	0.58	375	$<5.30 \times 10^{-9}$
60859.2121	0.66	519	$<7.48 \times 10^{-9}$
60859.2761	0.73	1001	$<3.54 \times 10^{-9}$
60859.3432	0.80	239	$<6.99 \times 10^{-9}$
60859.3471	0.80	325	$<6.04 \times 10^{-9}$
60859.7278	1.18	660	$<9.66 \times 10^{-9}$
60859.8519	1.30	442	$<4.61 \times 10^{-9}$
60859.8610	1.31	256	$<1.00 \times 10^{-8}$
60859.9193	1.37	1496	$<2.99 \times 10^{-9}$
60859.9862	1.44	769	$<4.05 \times 10^{-9}$
60860.1206	1.57	443	$<2.70 \times 10^{-8}$
60860.3682	1.82	1725	$<4.35 \times 10^{-9}$
60860.4331	1.89	266	$<1.02 \times 10^{-8}$
60860.6995	2.15	827	$<6.01 \times 10^{-9}$
60860.7724	2.22	558	$<4.39 \times 10^{-9}$
60860.8303	2.28	1278	$<3.12 \times 10^{-9}$
60860.8910	2.34	1088	$<3.42 \times 10^{-9}$
60860.9052	2.36	872	$<1.86 \times 10^{-8}$
60861.0810	2.53	297	$<7.83 \times 10^{-7}$
60861.0875	2.54	364	$<7.71 \times 10^{-9}$
60861.2151	2.67	900	$<1.48 \times 10^{-8}$
60861.4190	2.87	1200	$<4.57 \times 10^{-9}$
60861.4730	2.93	256	$<9.71 \times 10^{-9}$
60861.7992	3.25	976	$<5.52 \times 10^{-9}$
60861.8680	3.32	368	$<7.61 \times 10^{-9}$
60862.0650	3.52	571	$<4.46 \times 10^{-9}$
60862.1294	3.58	641	$<6.58 \times 10^{-9}$
60862.2567	3.71	863	$<6.07 \times 10^{-9}$
60862.3354	3.79	525	$<6.14 \times 10^{-9}$
60862.3954	3.85	900	$<5.14 \times 10^{-9}$
60862.4452	3.90	358	$<8.32 \times 10^{-9}$
60862.5095	3.96	1169	$<4.90 \times 10^{-9}$
60862.5240	3.98	300	$<6.38 \times 10^{-9}$
60862.5746	4.03	812	$<5.78 \times 10^{-9}$

Note. The reported MJD is the midtime of the exposure. The fluxes are reported in 14–195 keV and correspond to upper limits at the 5σ level. We identify two detections at MJD 60858.6816 and 60858.8170.

Table 3
Peak Flux of Bursts Detected in Swift/BAT `GUANO` Data

Trigger Name	MJD	Flux ($\mathrm{erg\ cm^{-2}\ s^{-1}}$)
GRB 250702D	60858.54789	$(5.08 \pm 0.62) \times 10^{-8}$
GRB 250702C	60858.61768	$(3.43 \pm 1.30) \times 10^{-8}$
GRB 250702E	60858.68161	$(6.53 \pm 1.17) \times 10^{-8}$

Note. The fluxes are reported in 14–195 keV. The peak fluxes are for the peak 16.384 s intervals (largest intervals tested by `NITRATES`) within the available `GUANO` data.

Table 4
A Compilation of the High-energy Trigger Times for This Event, Which We Refer to as GRB 250702B

Telescope	Trigger Name	Time (UT)	MJD	References
EP	EP250702a[a]	2025-07-01 01:40:26	60857.0697	D. Y. Li et al. (2025)
Fermi	GRB 250702D[b]	2025-07-02 13:09:02	60858.5479	E. Neights et al. (2025b)
Fermi	GRB 250702B[c]	2025-07-02 13:56:05	60858.5806	E. Neights et al. (2025b)
Fermi	GRB 250702C[d]	2025-07-02 14:49:31	60858.6177	This work; E. Neights et al. (2025a)
Fermi	GRB 250702E	2025-07-02 16:21:33	60858.6816	E. Neights et al. (2025b)

Notes. We list only the initial telescope to report the detection but note that other high-energy monitors detected each of the associated GRB triggers. For further discussion, see E. Neights et al. (2025a).

[a] This is the start of the initial detection window for the 2025 July 1 detection by EP (D. Y. Li et al. 2025).

[b] This burst was initially classified as "below horizon" but was later determined to be a real GRB, based on a ground analysis (Fermi GBM Team 2025). This led to a deviation in the naming scheme, with "D" occurring before "B."

[c] This is the first reported trigger of the event and therefore taken as the name in this work (E. Neights et al. 2025b).

[d] While the association was retracted by Fermi, the transient has notable emission detected by Swift/BAT at this time (Section 2.1.1) that is robustly associated with this transient. A further discussion of its association is reported by E. Neights et al. (2025a).

Appendix B
Log of Trigger Times

Here, we provide a compilation of the high-energy trigger times of GRB 250702B in Table 4.

Appendix C
Temporal Fit Results

In Figure 14, we display the corner plot (D. Foreman-Mackey 2016) showing the results of our power-law fit $F = A\,t^{-\alpha}$ to the X-ray lightcurve. The normalization A is given in units of $10^{-11}\,\mathrm{erg\,cm^{-2}\,s^{-1}}$, corresponding to the X-ray flux at 1 day from the given T_0. The left panel shows the results when T_0 is left free, and the right panel shows the fit when T_0 is set to the trigger time of GRB 250702D. We performed an additional fit with a broken power law with free T_0. We required T_0 to be between MJD 60857 (2025 July 1) and MJD 60859. The results are shown in Figure 15. The best fit does not provide an improved reduced chi-squared ($\chi^2/\mathrm{dof} = 2.35$) compared to the single-power-law fits. If we allow T_0 to push further backward, i.e., before 2025 July 1, the results are similar, but the initial slope α_1 becomes significantly steeper (t^{-5}), and the second slope α_2 pushes closer to t^{-2}.

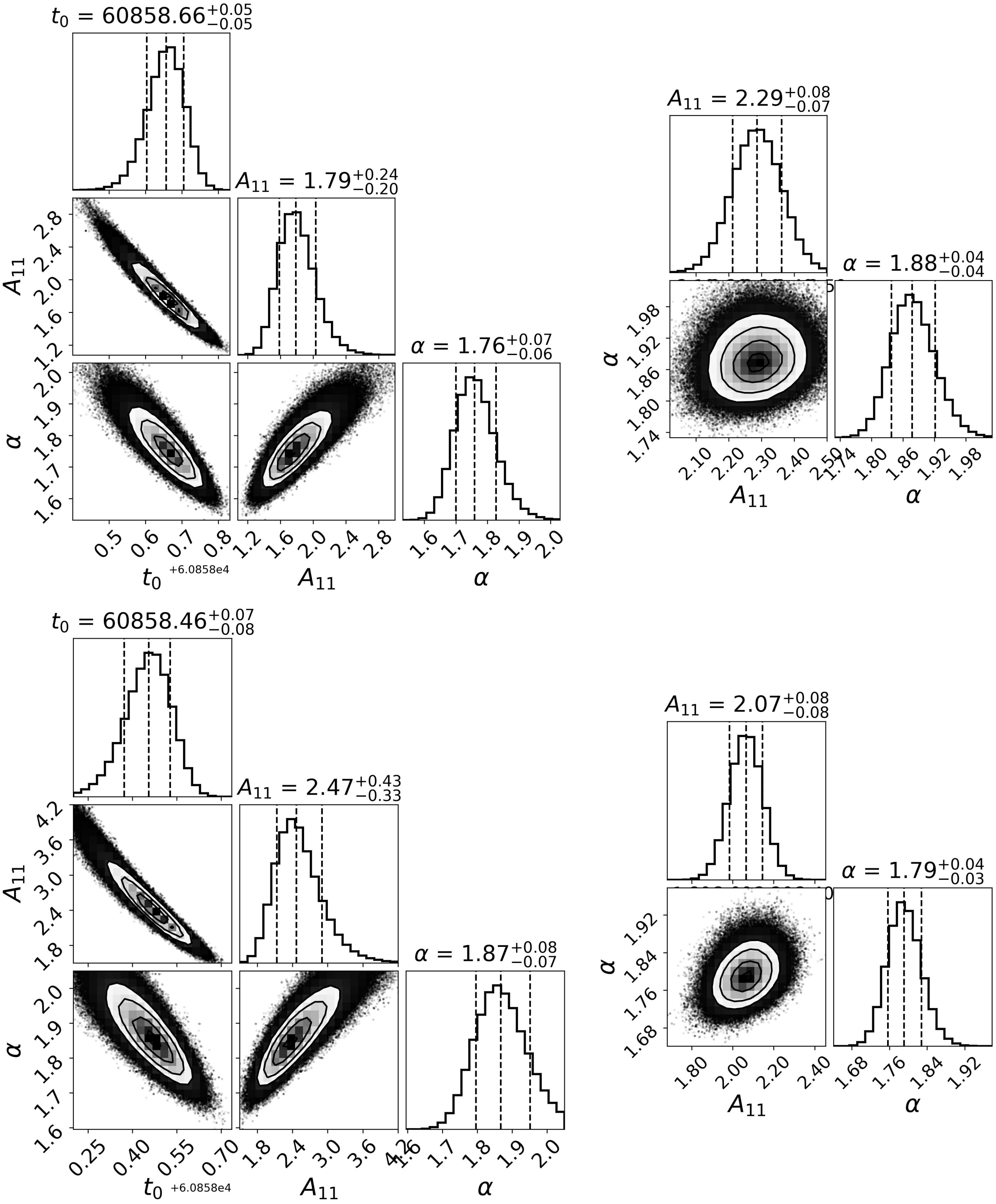

Figure 14. Top left: results of our temporal fit with the afterglow start time free. The fit includes all XRT and Chandra data. Top right: results of our temporal fit with the start time T_0 fixed to GRB 250702D’s trigger time. Bottom left: the same as the top left but only including XRT data after 0.55 days. Bottom right: the same as the bottom right but only including XRT data after 0.55 days. The posterior distributions on T_0 are also shown in Figure 1.

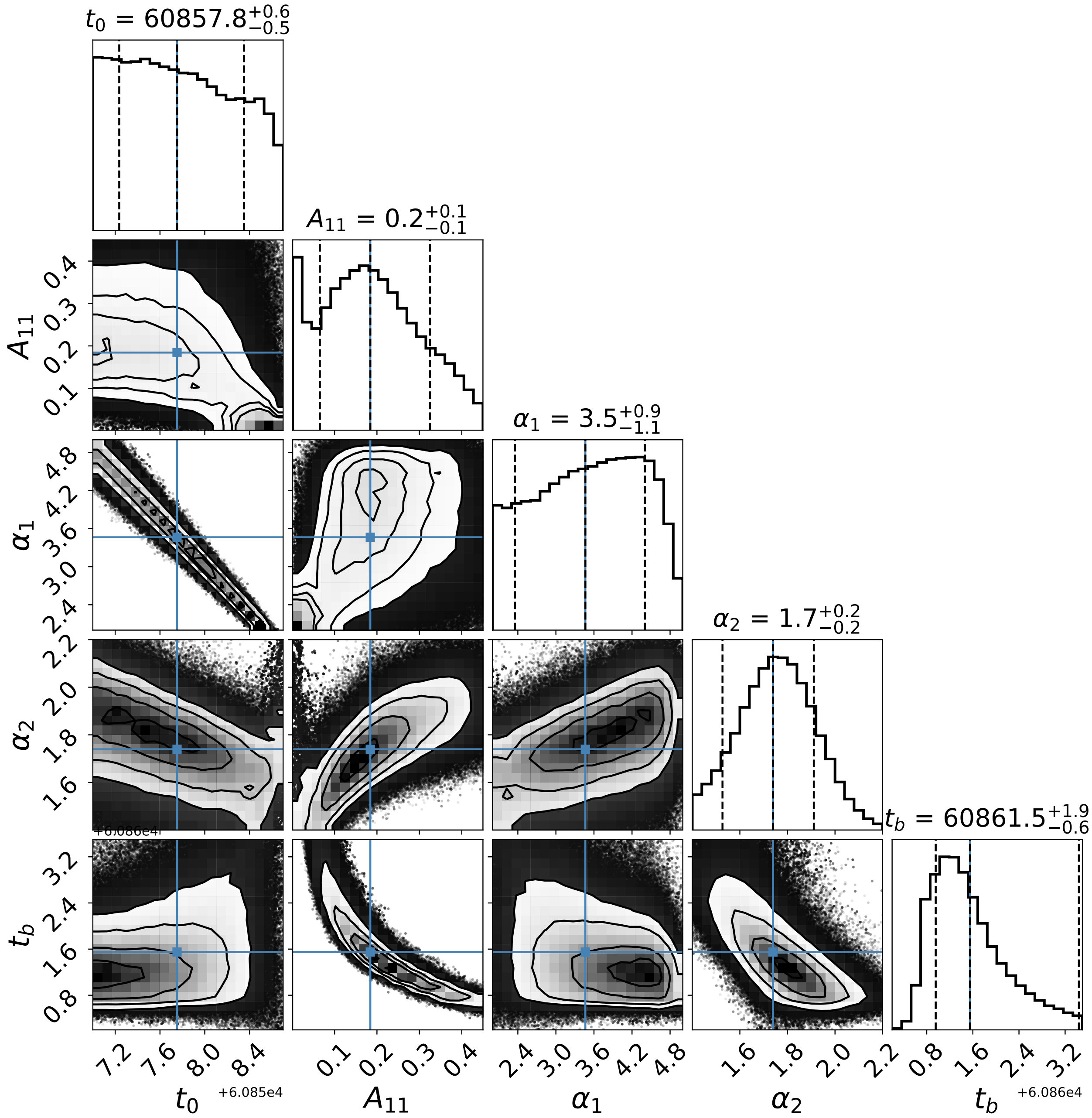

Figure 15. Results of our temporal fit with a broken power law with the onset time T_0 as a free parameter.

Appendix D Comparison to Variability in Other GRB Afterglows with NuSTAR

Since its launch in 2012, NuSTAR has observed a handful of GRB afterglows, including GRBs 130427A, 130925A, 150201A, 170817A, 180720B, 190114C, 190829A, and 221009A. We analyzed NuSTAR observations of these other GRBs to search for source variability (3–79 keV) in the afterglow phase for comparison to GRB 250702B (Figure 3 and Figure 16). We analyzed GRB 130427A (ObsIDs: 80002095002 and 80002095004), GRB 130925A (ObsIDs: 80002096002 and 80002096004), GRB 180720B (ObsID: 80401424002), GRB 190114C (ObsID: 90501602002), and GRB 221009A (ObsIDs: 90802329002, 90802329004, and 90802329006). We find that other NuSTAR observations of GRBs have lower count rates or resulted in nondetections (e.g., GRB 170817A). The data were reduced using the same procedures outlined in Section 2.2, with strict cuts on the particle background. In some cases (e.g., GRB 130925A), the source is observed at a lower count rate, where the limits on source variability are less meaningful (e.g., GRB 180720B in Figure 17). In Figure 17, we present a few representative lightcurves for comparison. To assess the variability, we computed the reduced chi-squared with regard to the weighted mean count rate per FPM. We find that these GRBs do not show evidence for variability in the 3–79 keV energy range. For example, GRB 221009A shows much less variability at a similar count rate (e.g., ObsIDs 90802329004 and 90802329006, occurring at 6 and 11 days, respectively; T. Laskar et al. 2023; B. O'Connor et al. 2023).

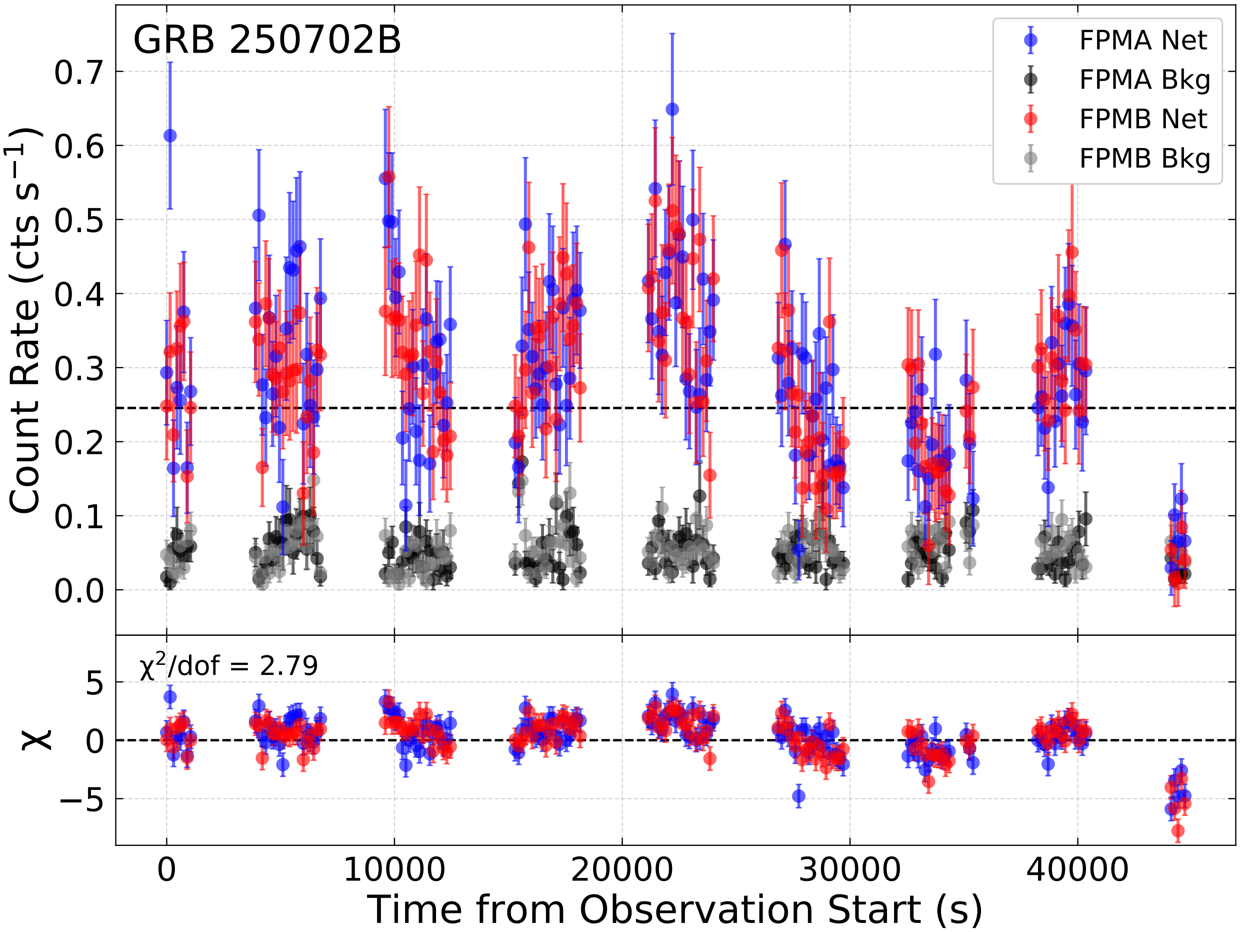

Figure 16. The background-subtracted 3–79 keV NuSTAR lightcurves for both FPMA and FPMB individually in 150 s bins. The background lightcurves for both FPMA and FPMB are also shown for comparison. The dashed black line shows the mean (background-subtracted) count rate in the observation (∼0.25 cts s^{-1}). The bottom panel shows the residuals (for both FPMA and FPMB) with respect to the mean count rate, to underscore the source's short-timescale variability.

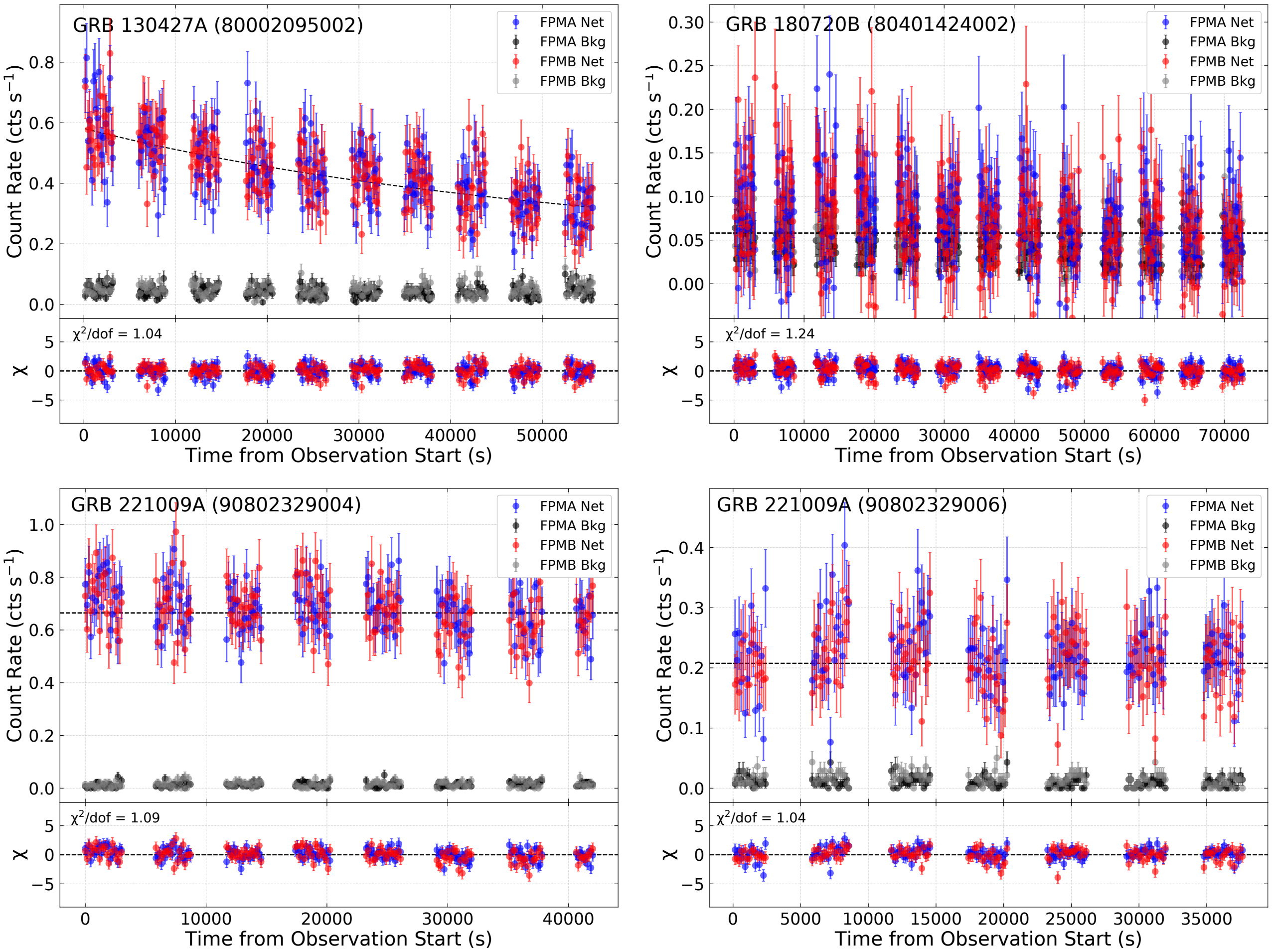

Figure 17. The same as Figure 16 but for multiple NuSTAR observations of GRB afterglows (see Appendix D for details).

Appendix E
HR Evolution Analysis

In Figure 18, we show that the HR, defined as the ratio of the counts in the hard band to the soft band, is constant over the course of our first NuSTAR observation. This is likely due to the low count rate in our observation, as a spectral evolution would be expected, given the source's lightcurve variability. We computed the HRs between 10–20 and 3–6 keV in 500 s bins for both FPMA and FPMB. We also investigated the HR of the Swift/XRT observations in the 0.3–2 and 2–10 keV energy bands. This is shown in Figure 19, though see also Figure 4. The HR does not show any significant long-term deviations, though short-term deviations were identified, especially in the first orbit of data shown in Figure 4.

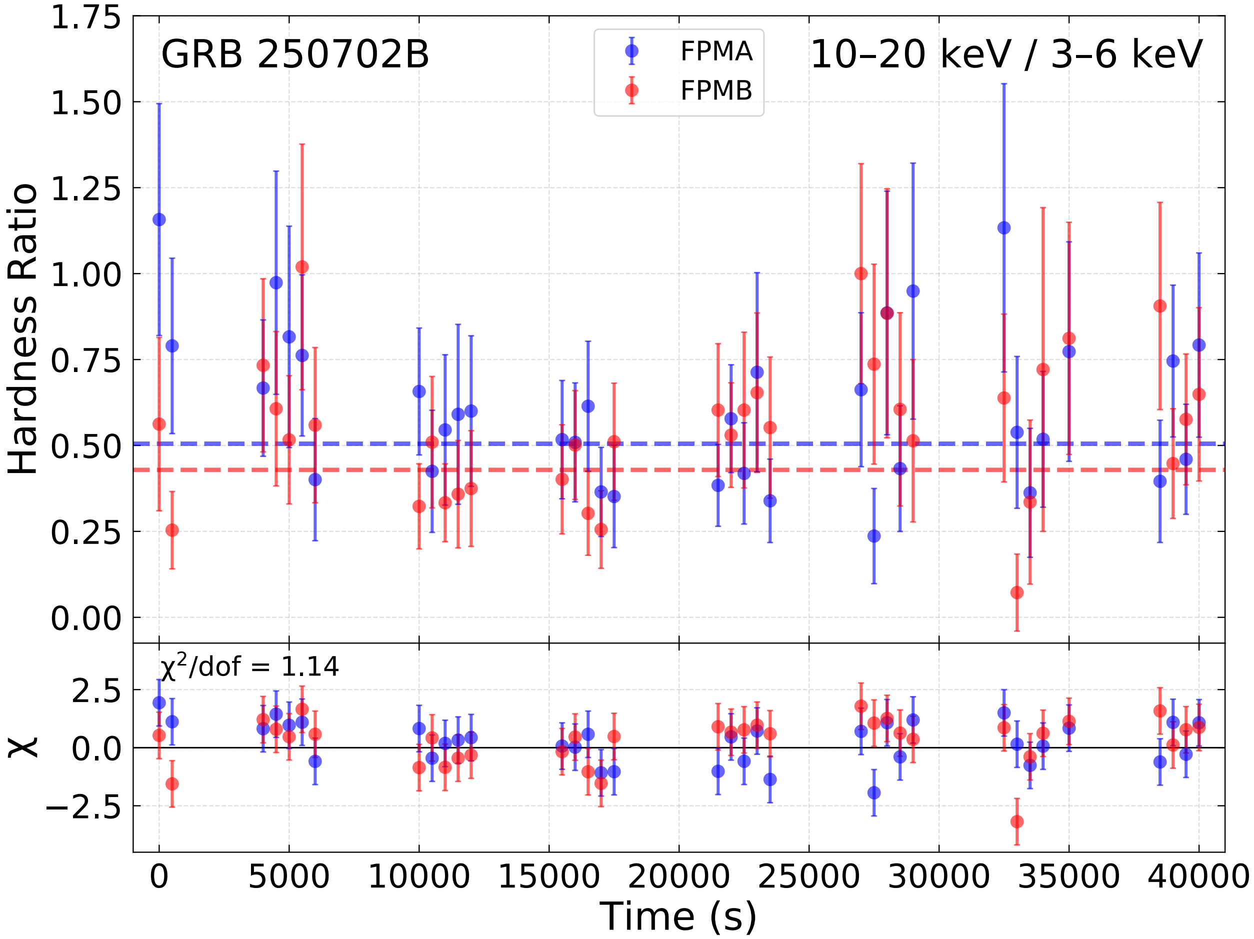

Figure 18. HRs (background-subtracted) computed between 10–20 and 3–6 keV in 500 s bins for both FPMA and FPMB. The weighted mean HRs for both FPMs are shown as horizontal lines. The bottom panel shows the residuals from the weighted mean HR.

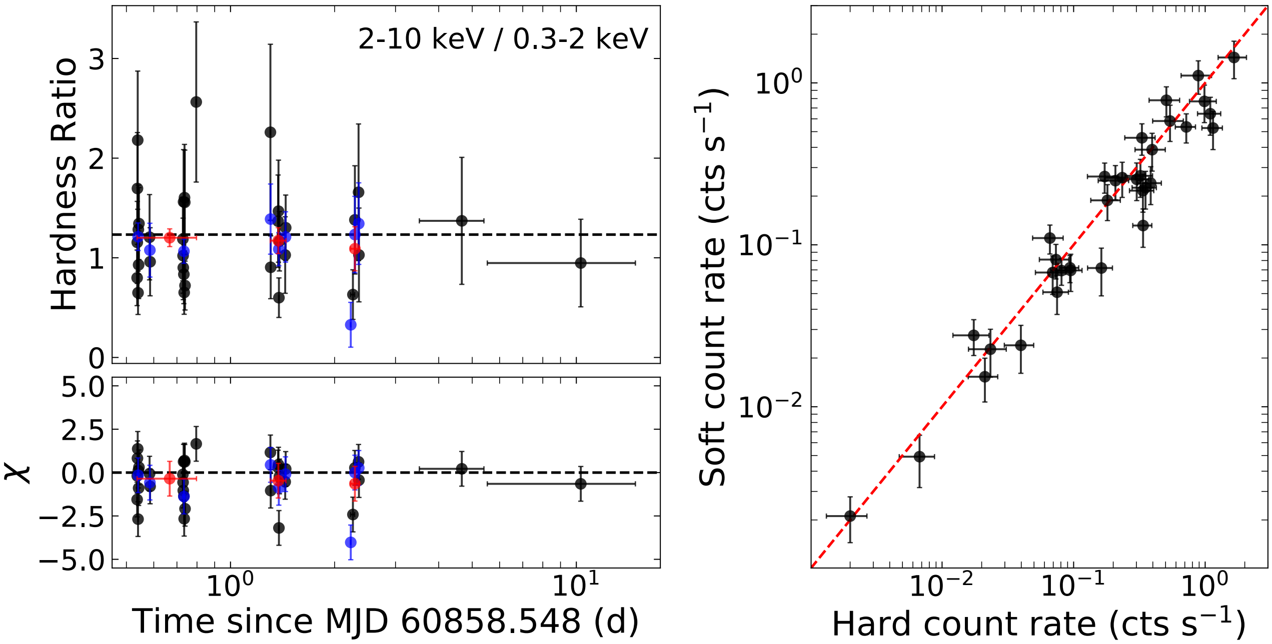

Figure 19. Left: Swift/XRT HR computed between 2–10 and 0.3–2 keV. The mean HR is shown as a horizontal line. The bottom panel shows the residuals from the mean HR. We also show the HR on a per-observation (red) and a per-snapshot (blue) basis for the first few days before multiple observations must be combined to achieve a detection. Right: hard (2–10 keV) versus soft (0.3–2 keV) count rates for the Swift/XRT lightcurve. The dashed line shows the expectation for a one-to-one HR. In both panels, the data are binned to a minimum of 20 counts per bin.

Appendix F
Afterglow Modeling Results

In Figure 20, we display the corner plot showing the posterior probability distributions for each model parameter, based on our broadband afterglow modeling in Section 3.3, which uses the "E" burst as T_0. Additional fits using the "D" burst as T_0 are presented in Figures 21 and 22.

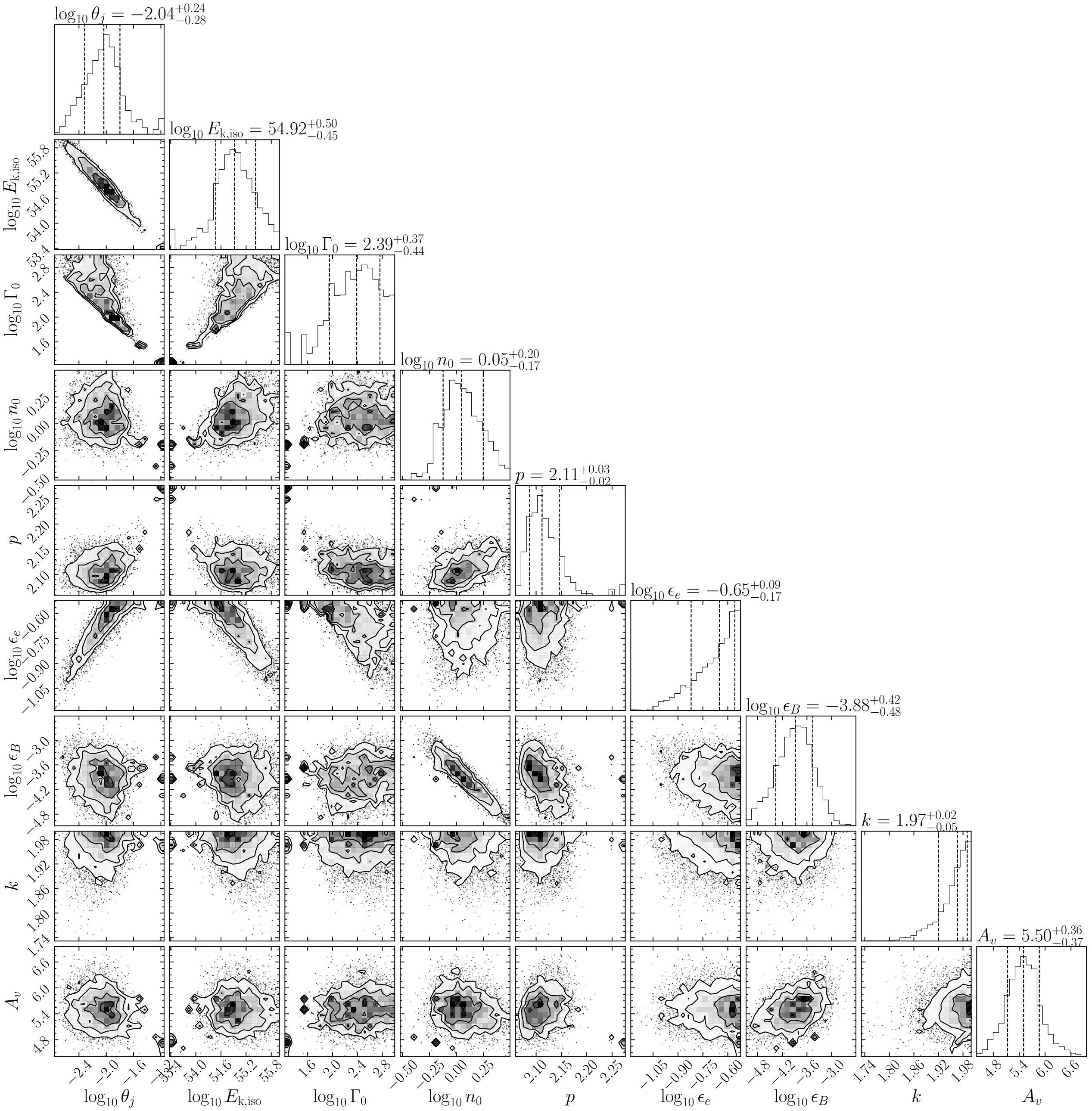

Figure 20. Corner plot showing the posterior parameter distributions of our FS afterglow modeling, as detailed in Section 3.3. We have used the GBM "E" burst as T_0. The condition $\Gamma_0\theta_j \geqslant 1$ is enforced, to prevent the jet from spreading laterally in the coasting phase.

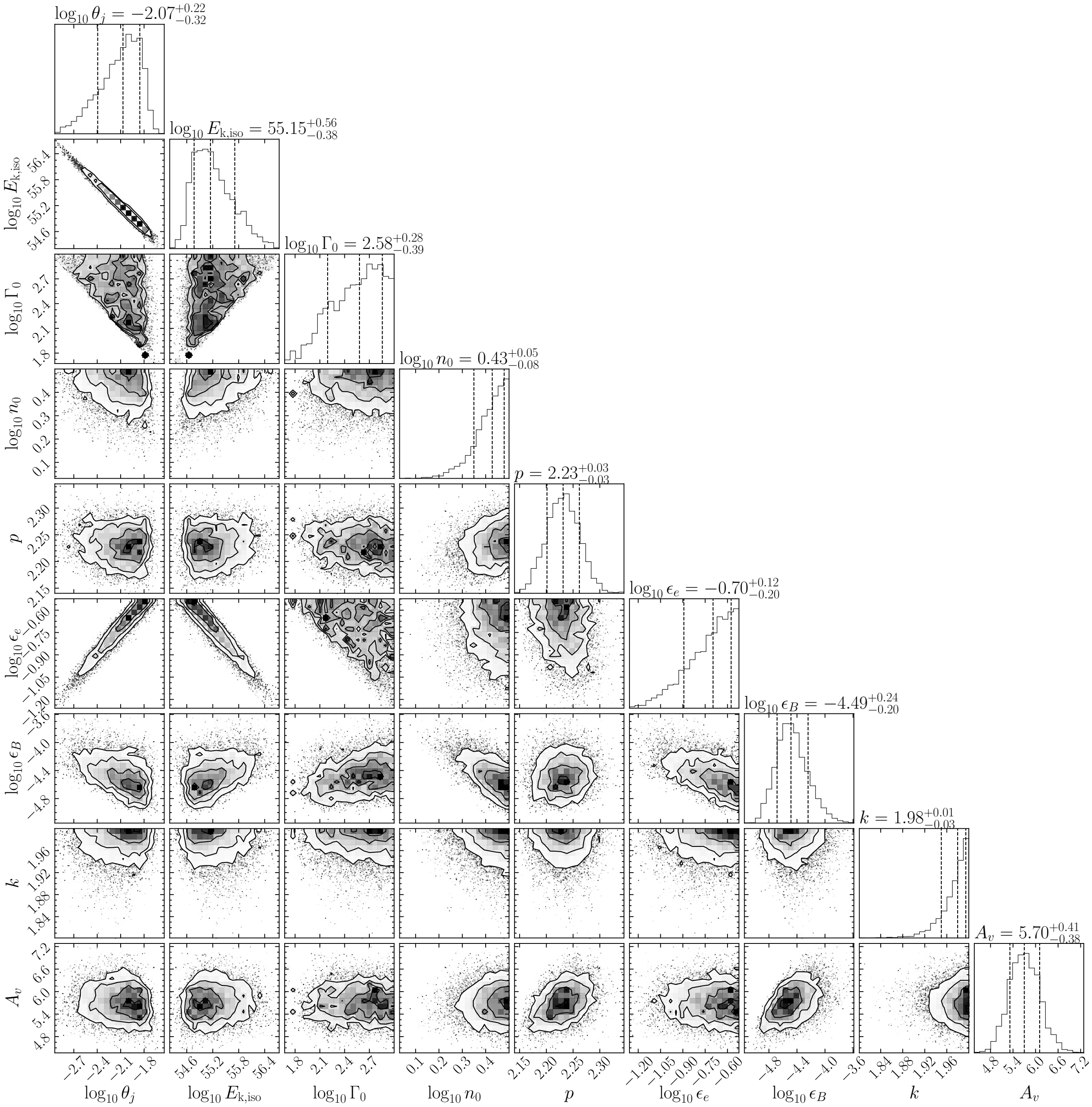

Figure 21. The same as Figure 20 but now using the GBM "D" burst as T_0.

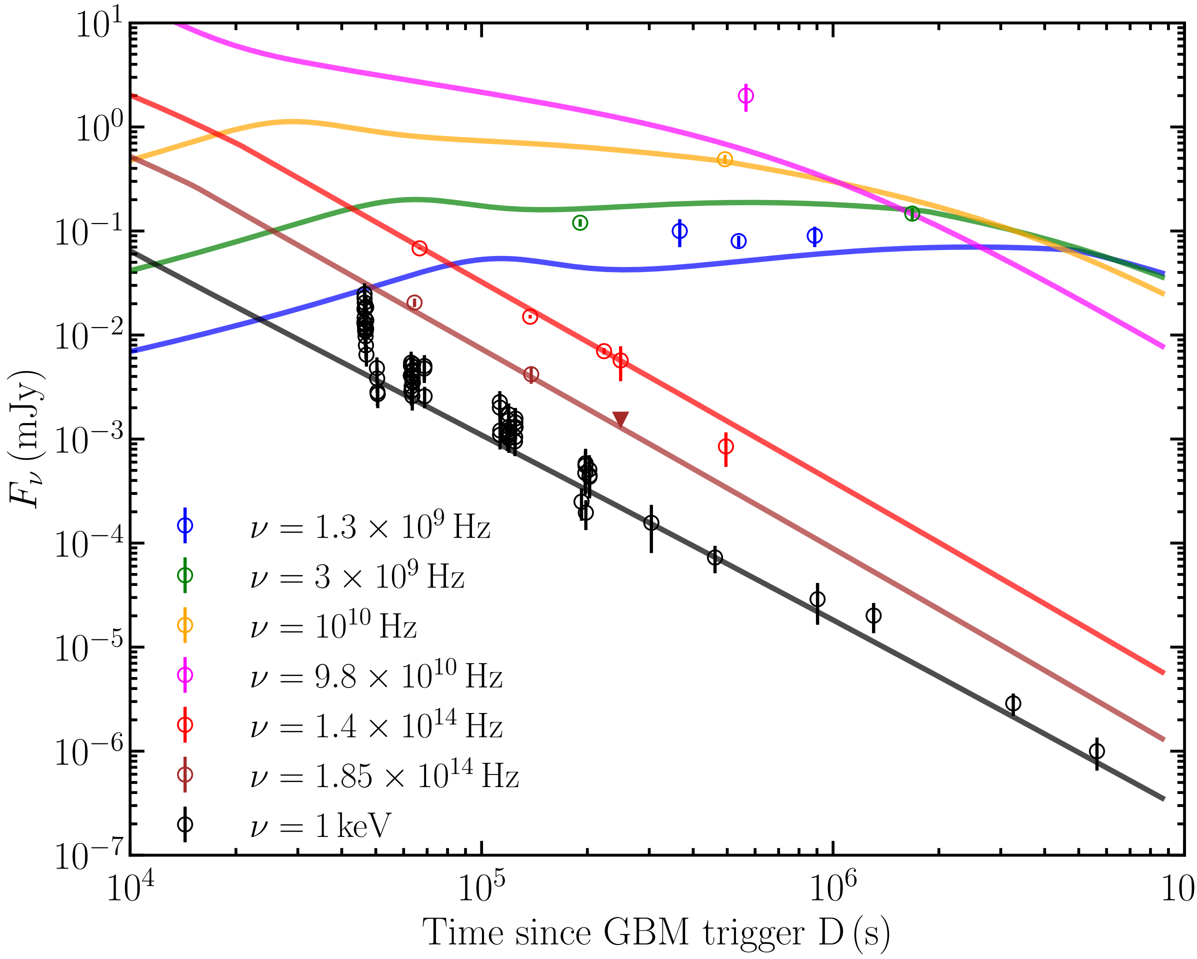

Figure 22. The same as Figure 9 but now using GRB 250702D as the start time T_0. The FS afterglow fit posterior distributions are shown in Figure 21, and the RS emission is now obtained with a different value of $\varepsilon_{B,\mathrm{RS}} = 2 \times 10^{-4}$. The description of the data is broadly consistent with the fit in Figure 9. The lightcurves are obtained for the following model parameters that keep the X-ray afterglow emission below the flaring X-ray emission at early times: $\theta_j = 4 \times 10^{-3}$ rad, $E_{\mathrm{k,iso}} = 4 \times 10^{55}$ erg, $\Gamma_0 = 282$, $n_0 = 1.9$ at $R_0 = 10^{18}$ cm, $p = 2.24$, $\epsilon_e = 0.13$, and $\epsilon_B = 10^{-4}$, $k = 2$.

ORCID iDs

Brendan O'Connor https://orcid.org/0000-0002-9700-0036
Ramandeep Gill https://orcid.org/0000-0003-0516-2968
James DeLaunay https://orcid.org/0000-0001-5229-1995
Jeremy Hare https://orcid.org/0000-0002-8548-482X
Dheeraj Pasham https://orcid.org/0000-0003-1386-7861
Eric R. Coughlin https://orcid.org/0000-0003-3765-6401
Ananya Bandopadhyay https://orcid.org/0000-0002-5116-844X
Akash Anumarlapudi https://orcid.org/0000-0002-8935-9882
Paz Beniamini https://orcid.org/0000-0001-7833-1043
Jonathan Granot https://orcid.org/0000-0001-8530-8941
Igor Andreoni https://orcid.org/0000-0002-8977-1498
Jonathan Carney https://orcid.org/0000-0001-8544-584X
Michael J. Moss https://orcid.org/0000-0002-1103-7082
Ersin Göğüş https://orcid.org/0000-0002-5274-6790
Jamie A. Kennea https://orcid.org/0000-0002-6745-4790
Malte Busmann https://orcid.org/0009-0001-0574-2332
Simone Dichiara https://orcid.org/0000-0001-6849-1270
James Freeburn https://orcid.org/0009-0006-7990-0547
Daniel Gruen https://orcid.org/0000-0003-3270-7644
Xander J. Hall https://orcid.org/0000-0002-9364-5419
Antonella Palmese https://orcid.org/0000-0002-6011-0530
Tyler Parsotan https://orcid.org/0000-0002-4299-2517
Samuele Ronchini https://orcid.org/0000-0003-0020-687X
Aaron Tohuvavohu https://orcid.org/0000-0002-2810-8764
Maia A. Williams https://orcid.org/0000-0002-0025-3601

References

Alexander, K. D., Miller-Jones, J., Goodwin, A., et al. 2025, GCN, 41059, 1
Andreoni, I., Coughlin, M. W., Perley, D. A., et al. 2022, Natur, 612, 430
Aptekar, R. L., Frederiks, D. D., Golenetskii, S. V., et al. 1995, SSRv, 71, 265
Arnaud, K. A. 1996, in ASP Conf. Ser. 101, Astronomical Data Analysis Software and Systems V, ed. G. H. Jacoby & J. Barnes (San Francisco, CA: ASP), 17
Astropy Collaboration, Price-Whelan, A. M., Lim, P. L., et al. 2022, ApJ, 935, 167
Astropy Collaboration, Price-Whelan, A. M., Sipőcz, B. M., et al. 2018, AJ, 156, 123
Atri, P., Rhodes, L., Fender, R., et al. 2025, GCN, 41054, 1
Balasubramanian, A., Resmi, L., Eappachen, D., et al. 2025, GCN, 41145, 1
Bandopadhyay, A., Fancher, J., Athian, A., et al. 2024, ApJL, 961, L2
Barthelmy, S. D., Barbier, L. M., Cummings, J. R., et al. 2005, SSRv, 120, 143
Beniamini, P., Nava, L., Duran, R. B., & Piran, T. 2015, MNRAS, 454, 1073
Beniamini, P., Nava, L., & Piran, T. 2016, MNRAS, 461, 51
Beniamini, P., Perets, H. B., & Granot, J. 2025, arXiv:2509.22779
Beniamini, P., Piran, T., & Matsumoto, T. 2023, MNRAS, 524, 1386
Berger, E. 2014, ARA&A, 52, 43
Bernardini, M. G., Margutti, R., Chincarini, G., Guidorzi, C., & Mao, J. 2011, A&A, 526, A27
Bloom, J. S., Giannios, D., Metzger, B. D., et al. 2011, Sci, 333, 203
Bouchet, P., Lequeux, J., Maurice, E., Prevot, L., & Prevot-Burnichon, M. L. 1985, A&A, 149, 330

Bromberg, O., Nakar, E., Piran, T., & Sari, R. 2012, ApJ, 749, 110
Bromberg, O., Nakar, E., Piran, T., & Sari, R. 2013, ApJ, 764, 179
Brown, G. C., Levan, A. J., Stanway, E. R., et al. 2015, MNRAS, 452, 4297
Burns, E., Svinkin, D., Fenimore, E., et al. 2023, ApJL, 946, L31
Burrows, D. N., Hill, J. E., Nousek, J. A., et al. 2005, SSRv, 120, 165
Burrows, D. N., Kennea, J. A., Ghisellini, G., et al. 2011, Natur, 476, 421
Cannizzo, J. K., Lee, H. M., & Goodman, J. 1990, ApJ, 351, 38
Carney, J., Andreoni, I., O'Connor, B., et al. 2025, arXiv:2509.22784
Cash, W. 1979, ApJ, 228, 939
Castro-Tirado, A. J., Bremer, M., McBreen, S., et al. 2007, A&A, 475, 101
Castro-Tirado, A. J., Gupta, R., Pandey, S. B., et al. 2024, A&A, 683, A55
Cenko, S. B., Frail, D. A., Harrison, F. A., et al. 2010, ApJ, 711, 641
Cenko, S. B., Krimm, H. A., Horesh, A., et al. 2012, ApJ, 753, 77
Cheng, H. Q., Zhang, Y. J., Zhao, G. Y., et al. 2025a, GCN, 40917, 1
Cheng, H. Q., Zhao, G. Y., Zhou, C., et al. 2025b, GCN, 40906, 1
Chevalier, R. A., & Li, Z.-Y. 2000, ApJ, 536, 195
Coughlin, E. R., & Nixon, C. J. 2022, MNRAS, 517, L26
Cufari, M., Coughlin, E. R., & Nixon, C. J. 2022, ApJ, 924, 34
Cummings, J. R., Barthelmy, S. D., Beardmore, A. P., et al. 2011, GCN, 11823, 1
Curran, P. A., Starling, R. L. C., O'Brien, P. T., et al. 2008, A&A, 487, 533
DeLaunay, J., Ronchini, S., Tohuvavohu, A., et al. 2025, GCN, 40903, 1
DeLaunay, J., & Tohuvavohu, A. 2022, ApJ, 941, 169
Eftekhari, T., Tchekhovskoy, A., Alexander, K. D., et al. 2024, ApJ, 974, 149
Evans, P. A., Osborne, J. P., Beardmore, A. P., et al. 2014b, ApJS, 210, 8
Evans, P. A., Page, K. L., Bearmore, A. P., et al. 2023, MNRAS, 518, 174
Evans, P. A., Willingale, R., Osborne, J. P., et al. 2014a, MNRAS, 444, 250
Eyles-Ferris, R. A., King, A., Starling, R. L., et al. 2025, arXiv:2509.22843
Eyles-Ferris, R. A. J., Levan, A. J., Martin-Carrillo, A., et al. 2025, GCN, 41767, 1
Fancher, J., Bandopadhyay, A., Coughlin, E. R., & Nixon, C. J. 2025, ApJ, 990, 104
Fermi GBM Team 2025, GCN, 40886, 1
Filgas, R., Greiner, J., Schady, P., et al. 2011, A&A, 535, A57
Foreman-Mackey, D. 2016, JOSS, 1, 24
Foreman-Mackey, D., Hogg, D. W., Lang, D., & Goodman, J. 2013, PASP, 125, 306
Frail, D. A., Kulkarni, S. R., Sari, R., et al. 2001, ApJL, 562, L55
Frederiks, D., Lysenko, A., Ridnaia, A., et al. 2025, GCN, 40914, 1
Fruscione, A., McDowell, J. C., Allen, G. E., et al. 2006, Proc. SPIE, 6270, 62701V
Fryer, C. L., & Woosley, S. E. 1998, ApJL, 502, L9
Garain, D., & Sarkar, T. 2024, ApJ, 967, 167
Gehrels, N., Chincarini, G., Giommi, P., et al. 2004, ApJ, 611, 1005
Gendre, B., Stratta, G., Atteia, J. L., et al. 2013, ApJ, 766, 30
Ghirlanda, G., Nappo, F., Ghisellini, G., et al. 2018, A&A, 609, A112
Giannios, D. 2013, MNRAS, 431, 355
Giannios, D., Uzdensky, D. A., & Begelman, M. C. 2009, MNRAS, 395, L29
Gill, R., & Granot, J. 2018, MNRAS, 478, 4128
Gill, R., & Granot, J. 2023, MNRAS, 524, L78
Golkhou, V. Z., & Butler, N. R. 2014, ApJ, 787, 90
Gompertz, B. P., Levan, A. J., Laskar, T., et al. 2025, arXiv:2509.22778
Gordon, K. D., Fitzpatrick, E. L., Massa, D., et al. 2024, ApJ, 970, 51
Granot, J. 2007, arXiv:astro-ph/0610379
Granot, J., & Sari, R. 2002, ApJ, 568, 820
Greiner, J., Krühler, T., Klose, S., et al. 2011, A&A, 526, A30
Greiner, J., Mazzali, P. A., Kann, D. A., et al. 2015, Natur, 523, 189
Greiner, J., Yu, H. F., Krühler, T., et al. 2014, A&A, 568, A75
Grollimund, N., Corbel, S., Coleiro, A., Cangemi, F., & Rodriguez, J. 2025, GCN, 41147, 1
Güver, T., & Özel, F. 2009, MNRAS, 400, 2050
Harrison, F. A., Craig, W. W., Christensen, F. E., et al. 2013, ApJ, 770, 103
Hills, J. G. 1988, Natur, 331, 687
Huppenkothen, D., Bachetti, M., Stevens, A. L., et al. 2019, ApJ, 881, 39
Ioka, K., Hotokezaka, K., & Piran, T. 2016, ApJ, 833, 110
Jin, C. C., Li, D. Y., Jiang, N., et al. 2025, arXiv:2501.09580
Kawakubo, Y., Serino, M., Negoro, H., et al. 2025, GCN, 40910, 1
Kennea, J. A., Siegel, M. H., Evans, P. A., et al. 2025, GCN, 40919, 1
Kouveliotou, C., Meegan, C. A., Fishman, G. J., et al. 1993, ApJL, 413, L101
Krühler, T., Greiner, J., Schady, P., et al. 2011a, A&A, 534, A108
Krühler, T., Schady, P., Greiner, J., et al. 2011b, A&A, 526, A153
Kumar, P., & Panaitescu, A. 2000, ApJL, 541, L51
Lacy, J. H., Townes, C. H., & Hollenbach, D. J. 1982, ApJ, 262, 120
Laskar, T., Alexander, K. D., Margutti, R., et al. 2023, ApJL, 946, L23
Leahy, D. A., Darbro, W., Elsner, R. F., et al. 1983, ApJ, 266, 160
Lesage, S., Veres, P., Briggs, M. S., et al. 2023, ApJL, 952, L42
Leung, J. K., Sharan Salafia, O., Spingola, C., et al. 2025, arXiv:2502.13435
Levan, A. J., Jonker, P. G., Saccardi, A., et al. 2025a, NatAs, 9, 1375
Levan, A. J., Martin-Carrillo, A., Laskar, T., et al. 2025b, ApJL, 990, L28
Levan, A. J., Tanvir, N. R., Brown, G. C., et al. 2016, ApJ, 819, 51
Levan, A. J., Tanvir, N. R., Cenko, S. B., et al. 2011, Sci, 333, 199
Levan, A. J., Tanvir, N. R., Starling, R. L. C., et al. 2014, ApJ, 781, 13
Li, D. Y., Yang, J., Zhang, W. D. & The Einstein Probe Collaborations 2025, arXiv:2509.25877
Liu, Y., Sun, H., Xu, D., et al. 2025, NatAs, 9, 564
Lodato, G., King, A. R., & Pringle, J. E. 2009, MNRAS, 392, 332
Lodato, G., & Rossi, E. M. 2011, MNRAS, 410, 359
Lomb, N. R. 1976, Ap&SS, 39, 447
Madsen, K. K., Grefenstette, B. W., Pike, S., et al. 2020, arXiv:2005.00569
Mangano, V., Burrows, D. N., Sbarufatti, B., & Cannizzo, J. K. 2016, ApJ, 817, 103
Margutti, R., Bernardini, G., Barniol Duran, R., et al. 2011, MNRAS, 410, 1064
Matsuoka, M., Kawasaki, K., Ueno, S., et al. 2009, PASJ, 61, 999
Meegan, C., Lichti, G., Bhat, P. N., et al. 2009, ApJ, 702, 791
Mészáros, P., & Rees, M. J. 1997, ApJ, 476, 232
Mészáros, P., & Rees, M. J. 2001, ApJL, 556, L37
Mockler, B., Guillochon, J., & Ramirez-Ruiz, E. 2019, ApJ, 872, 151
Molinari, E., Vergani, S. D., Malesani, D., et al. 2007, A&A, 469, L13
Nakar, E. 2007, PhR, 442, 166
Nakauchi, D., Kashiyama, K., Suwa, Y., & Nakamura, T. 2013, ApJ, 778, 67
Nasa High Energy Astrophysics Science Archive Research Center (Heasarc), 2014 HEAsoft: Unified Release of FTOOLS and XANADU, Astrophysics Source Code Library, ascl:1408.004
Nauenberg, M. 1972, ApJ, 175, 417
Nava, L., Vianello, G., Omodei, N., et al. 2014, MNRAS, 443, 3578
Neights, E., Burns, E., Fryer, C. L., et al. 2025a, arXiv:2509.22792
Neights, E., Roberts, O. J., Burns, E., Veres, P. & Fermi-GBM TeamFermi-GBM Team 2025b, GCN, 40891, 1
Nicholl, M., Lanning, D., Ramsden, P., et al. 2022, MNRAS, 515, 5604
Nysewander, M., Fruchter, A. S., & Pe'er, A. 2009, ApJ, 701, 824
O'Connor, B., Beniamini, P., & Kouveliotou, C. 2020, MNRAS, 495, 4782
O'Connor, B., Pasham, D., Andreoni, I., & Hare, J. 2025a, GCN, 41014, 1
O'Connor, B., Pasham, D., Andreoni, I., et al. 2025b, ApJL, 979, L30
O'Connor, B., Pasham, D., Andreoni, I., et al. 2025c, GCN, 41309, 1
O'Connor, B., Troja, E., Ryan, G., et al. 2023, SciA, 9, eadi1405
Oganesyan, G., Kammoun, E., Ierardi, A., et al. 2025, arXiv:2507.18694
Parsotan, T., Laha, S., Palmer, D. M., et al. 2023, ApJ, 953, 155
Parsotan, T., & Lazzati, D. 2024, ApJ, 974, 158
Pasham, D. R., Cenko, S. B., Levan, A. J., et al. 2015, ApJ, 805, 68
Pasham, D. R., Lucchini, M., Laskar, T., et al. 2023, NatAs, 7, 88
Pasham, D. R., Remillard, R. A., Fragile, P. C., et al. 2019, Sci, 363, 531
Pei, Y. C. 1992, ApJ, 395, 130
Perets, H. B., Li, Z., Lombardi, J. C., Jr., & Milcarek, S. R., Jr. 2016, ApJ, 823, 113
Perley, D. A., Cenko, S. B., Bloom, J. S., et al. 2009, AJ, 138, 1690
Perley, D. A., Morgan, A. N., Updike, A., et al. 2011, AJ, 141, 36
Planck Collaboration, Aghanim, N., Akrami, Y., et al. 2020, A&A, 641, A6
Predehl, P., & Schmitt, J. H. M. M. 1995, A&A, 293, 889
Price, D. J., Wurster, J., Tricco, T. S., et al. 2018, PASA, 35, e031
Rees, M. J. 1988, Natur, 333, 523
Reis, R. C., Miller, J. M., Reynolds, M. T., et al. 2012, Sci, 337, 949
Rhoads, J. E. 1997, ApJL, 487, L1
Rhoads, J. E. 1999, ApJ, 525, 737
Sakamoto, T., Barthelmy, S. D., Baumgartner, W. H., et al. 2011, GCN, 11842, 1
Sari, R., & Mészáros, P. 2000, ApJL, 535, L33
Sari, R., & Piran, T. 1995, ApJL, 455, L143
Sari, R., & Piran, T. 1999, ApJ, 520, 641
Sari, R., Piran, T., & Halpern, J. P. 1999, ApJL, 519, L17
Sari, R., Piran, T., & Narayan, R. 1998, ApJL, 497, L17
Saxton, C. J., Soria, R., Wu, K., & Kuin, N. P. M. 2012, MNRAS, 422, 1625
Scargle, J. D. 1982, ApJ, 263, 835
Scargle, J. D. 1998, ApJ, 504, 405
Scargle, J. D., Norris, J. P., Jackson, B., & Chiang, J. 2013, ApJ, 764, 167
Schady, P., Page, M. J., Oates, S. R., et al. 2010, MNRAS, 401, 2773
Schlafly, E. F., & Finkbeiner, D. P. 2011, ApJ, 737, 103
Sfaradi, A. I., Yao, Y., Sears, H., et al. 2025, GCN, 41053, 1
Shukla, A., & Mannheim, K. 2020, NatCo, 11, 4176
Stone, N., Sari, R., & Loeb, A. 2013, MNRAS, 435, 1809
Stratta, G., Gendre, B., Atteia, J. L., et al. 2013, ApJ, 779, 66
Svom/Grm Team, Wang, C.-W., Zheng, S.-J., et al. 2025, GCN, 40923, 1

Swenson, C. A., & Roming, P. W. A. 2014, ApJ, 788, 30
Tetarenko, A. J., Bright, J., Bower, G., & Graves, S. 2025, GCN, 41061, 1
Tikhomirova, Y. Y., & Stern, B. E. 2005, AstL, 31, 291
Tohuvavohu, A., Kennea, J. A., DeLaunay, J., et al. 2020, ApJ, 900, 35
Troja, E., Sakamoto, T., Guidorzi, C., et al. 2012, ApJ, 761, 50
van der Horst, A. J., Kouveliotou, C., Gehrels, N., et al. 2009, ApJ, 699, 1087
van Velzen, S., Stone, N. C., Metzger, B. D., et al. 2019, ApJ, 878, 82
Verner, D. A., Ferland, G. J., Korista, K. T., & Yakovlev, D. G. 1996, ApJ, 465, 487
Virtanen, P., Gommers, R., Oliphant, T. E., et al. 2020, NatMe, 17, 261
Wang, X.-G., Zhang, B., Liang, E.-W., et al. 2018, ApJ, 859, 160
Wei, J., Cordier, B., Antier, S., et al. 2016, arXiv:1610.06892
Wijers, R. A. M. J., & Galama, T. J. 1999, ApJ, 523, 177
Willingale, R., Starling, R. L. C., Beardmore, A. P., Tanvir, N. R., & O'Brien, P. T. 2013, MNRAS, 431, 394
Wilms, J., Allen, A., & McCray, R. 2000, ApJ, 542, 914
Woosley, S. E. 1993, ApJ, 405, 273
Woosley, S. E., & Heger, A. 2012, ApJ, 752, 32
Yao, Y., Chornock, R., Ward, C., et al. 2025, ApJL, 985, L48
Yao, Y., Lu, W., Harrison, F., et al. 2024, ApJ, 965, 39
Yin, Y.-H. I., Fang, Y., Zhang, B.-B., et al. 2025, ApJL, 989, L39
Yin, Y.-H. I., Zhang, B.-B., Yang, J., et al. 2024, ApJL, 975, L27
Yuan, W., Dai, L., Feng, H., et al. 2025, SCPMA, 68, 239501
Zafar, T., Watson, D., Fynbo, J. P. U., et al. 2011, A&A, 532, A143
Zauderer, B. A., Berger, E., Margutti, R., et al. 2013, ApJ, 767, 152
Zauderer, B. A., Berger, E., Soderberg, A. M., et al. 2011, Natur, 476, 425
Zhang, W., Yuan, W., Ling, Z., et al. 2025, SCPMA, 68, 219511